Fermiology, 3D to 2D dimensionality crossover and electron-phonon coupling in the electronic structure of transition metal dichalcogenides

Zakariae El Youbi

CY CERGY-PARIS UNIVERSITY

DOCTORAL THESIS

Fermiology, 3D to 2D dimensionality crossover and electron-phonon coupling in the electronic structure of transition metal dichalcogenides

Author:
Zakariae EL YOUBI

Referee: Dr. Pavel Dudin
Referee: Prof. Dr. Neil Wilson

Examiner: Dr. Christine Boeglin
Examiner: Dr. Véronique Brouet

Supervisor: Prof. Dr. Karol Hricovini
Supervisor: Prof. Dr. Christine Richter
Supervisor: Dr. Cephise Cacho
Co-Supervisor: Dr. Matthew D. Watson

A thesis submitted in fulfillment of the requirements
for the degree of Doctor of Philosophy

May 6, 2021

"Felix, qui potuit rerum cognoscere causas."

"Fortunate, who was able to know the causes of things."

"Heureux, qui a pu pénétrer la raison des choses."

Vergil Georgics

Abstract

This PhD consists in the investigation of the electronic structure of transition metal dichalcogenides (TMDs), namely 1T-$HfTe_2$, 2H-NbS_2 and 3R-NbS_2 using angle-resolved photoemission spectroscopy (ARPES). While the first part is dedicated to a methodical study of the electronic band structure of 1T-$HfTe_2$ and its evolution with potassium dosing, the second part presents a comparative study of the two phases of NbS_2 and the experimental evidence of the strong electron-phonon coupling in the 2H phase.

The dosing of layered materials with alkali metals has become a commonly used strategy in ARPES experiments. However, precisely what occurs under such conditions, both structurally and electronically, has remained a matter of debate.

In this thesis, we performe a systematic study of 1T-$HfTe_2$, a prototypical semimetal of the TMDs family. By utilizing photon energy-dependent ARPES, we have investigated the electronic structure of this material as a function of Potassium (K) deposition. From the k_z maps, we observe the appearance of 2D dispersive bands after electron dosing, with an increasing sharpness of the bands, consistent with the wavefunction confinement at the topmost layer.

In our highest-dosing cases, a monolayer-like electronic structure emerges, presumably as a result of intercalation of the alkali metal. Here, by bringing the topmost valence band below E_F, we could directly measure a band overlap of ~ 0.2 eV. However, 3D bulk-like states still contribute to the spectra even after considerable dosing. Our work on $HfTe_2$ provides a reference point for the increasingly popular studies of the alkali metal dosing of semimetals using ARPES.

In our second work, we investigated the electronic band structure of the two polytypes of NbS_2, namely 2H-NbS_2 and 3R-$Nb_{1+x}S_2$ combining ARPES and density functional theory (DFT) calculations. The measured Fermi surfaces show a remarkable difference in size, reflecting a significantly increased band filling in 3R-$Nb_{1+x}S_2$ due to the presence of additional Nb interstitials. Thus we found that the stoichiometry, rather than the stacking arrangement, is the most important factor in the difference in electronic and physical properties of the two phases.

Our high resolution data on the 2H phase shows strong kinks in the spectral function that are fingerprints of the electron-phonon coupling. However, the strength of the coupling is found to be much larger for the the sections of bands with Nb $4d_{x^2-y^2,xy}$ character than for the Nb $4d_{3z^2-r^2}$. Our results provide an experimental framework for interpreting the two-gap superconductivity and latent CDW in 2H-NbS_2.

Resumé

Cette thèse consiste à l'investigation de la structure électronique des métaux de transition dichalcogénides (TMDs), notamment 1T-$HfTe_2$, 2H-NbS_2 et 3R-NbS_2 en utilisant la spectroscopie de photoémission résolue en angle ARPES. La première partie est dédiée à une étude méthodique de la structure de bande de $HfTe_2$ et son évolution en fonction de dosage, alors que la deuxième présente une étude comparative des deux polytypes de NbS_2 et l'évidence expérimentale de fort couplage électron-phonon dans la phase 2H.

Le dosage des matériaux en couches avec les métaux alcalins est devenu une stratégie commune dans ARPES, mais ce qui se passe mais ce qui passe au niveau structurel et électronique a toujours été sujet de débat. Dans cette thèse, on réalise une étude de 1T-$HfTe_2$, un semimetal prototypique de la famille des TMDs. En utilisant ARPES en dépendance de l'énergie de photons, nous avons examiné la structure électronique de ce matériau en fonction du dosage avec le potassium K. D'après nos spectres de k_z, on a observé l'apparence de 2D états électroniques après le dosage, avec une amélioration remarquable de la qualité des données mesurées, en accord avec le confinement de la fonction d'onde à la plus haute monocouche.

A notre niveau de dosage le plus élevé, la structure électronique mesurée est similaire à celle d'une monocouche, attestant l'intercalation des atomes alcalines dans le gap de van der Waals. En ramenant le top de la bande de valence en dessous du niveau de Fermi, nous avons directement mesuré le gap négatif d'une valeur de 0.2 eV. Toutefois, des états électroniques de volumes contribuent toujours au spectre même après une quantité considérable de dosage. Enfin, la bande de valence de $HfTe_2$ contient un point de Dirac et un gap inversé, en analogie avec tous les TMDs du même groupe de symétrie. Notre étude de $HfTe_2$ présente une référence pour la croissante popularité de dosage de semimétaux dans l'ARPES.

Dans notre deuxième projet, nous avons étudié les deux polytypes de NbS_2, notamment 2H-NbS_2 et 3R-$Nb_{(1+x)}S_2$ en utilisant ARPES et les calculs DFT (density functional theory). Les deux surfaces de Fermi mesurées montrent une grande différence en taille, indiquant un remplissage de bande plus important dans le 3R phase en raison d'atomes interstitielles de Nb. Cela montre que la stoichiométrie est le facteur le plus important dans la différence des propriétés électronique et physiques des deux phases, et pas l'empilement de couche.

Nos données avec la meilleure résolution de 2H-NbS_2 montrent de forts 'kinks' dans la fonction spectrale, témoignant l'électron-phonon couplage dans ce système. Nous avons trouvé que ce couplage est plus fort dans les sections de bandes dérivées de Nb $4d_{x^2-y^2,xy}$ orbitales que dans celles de Nb $4d_{3z^2-r^2}$ orbitales. Nos résultats présentent un cadre expérimental pour l'interprétation des deux gaps supraconducteurs et l'absence de l'onde de densité de charge dans 2H-NbS_2.

Acknowledgements

At the beginning, I would like to thank my supervisors, Dr. Cephise Cacho, Prof. Christine Richter and Prof. Karol Hricovini for giving me the opportunity to do this PhD, and all the people from the LPMS and I05-ARPES beamline for their help and support.

This thesis wouldn't have been accomplished the way it did without the presence of Dr. Matthew D. Watson, who has provided me with unconditional support and valuable guidance. I will not forget the many hours we spent working on and discussing fascinating research topics. It has been a great joy learning from you and I am extremely grateful for your commitment to both my academic and personal development.

I am gratefully thankful to Dr. Sungwon Jung for introducing me to the I05 beamline and providing me with precious assistance during the beamtimes. I was very fortunate to work with you and benefit from your delightful insights and constructive comments.

A thesis cannot come to an end without phases of stress and anxiety, but I have been very lucky to have great people standing by me, Oussama Hanguir, Othmane Sayem, Xavier Romon and Jean-Christophe Lambret who, through their wisdom, sagacity and shrew have kept me grounded and focused on my ultimate goal. I owe you enormous gratitude and recognition, your backing has gone beyond this PhD and affected numerous aspects of my life journey.

I would like to thank my friends for the amazing moments we've spent together. My friends from Naples Jerry De Crescenzo, Fabio Marzocchi and Danilo Argentino for their warm welcome and shared passion. Tom Charleston, Eileen Naughton, Sonka Reimers and all the members of Didcot runners running club for the joyful running sessions and races across Oxfordshire. Coach Dominique Trélat for his amazing character and all the members of the trail club in Cergy for the wonderful memories in *l'ile de loisirs* and Beaujolais mountains. My thanks go as well to Oussama Madih, Thomas Djezzane, Reda Idil, Régis Lambret, Chaima El Khattabi, Nizar Benyahia, Younes El Chaheb, Emily Kloos, Salh Akssas, Youssef El Bikri and Jean Piard.

Last, but not least. I express my immense gratitude to my mother, my sisters and Becky for their unconditional love, constant cheer and encouragement, and for reminding me that life is not all about physics.

Publications

1. **Fermiology and electron-phonon coupling in the 2H and 3R polytypes of NbS_2**
Zakariae El Youbi, Sung Won Jung, Christine Richter, Karol Hricovini, Cephise Cacho, Matthew D. Watson. (Submitted to Phys. Rev. Letters, DOI: https://arxiv.org/abs/2012.12595).

2. **Bulk and surface electronic states in the dosed semimetallic $HfTe_2$**
Zakariae El Youbi, Sung Won Jung, Saumya Mukherjee, Mauro Fanciulli, Jakub Schusser, Olivier Heckmann, Christine Richter, Ján Minár, Karol Hricovini, Matthew D. Watson, and Cephise Cacho. (Phy. Rev. B 101, 235431 (2020), DOI: 10.1103/PhysRevB.101.235431).

3. **Spin, time, and angle resolved photoemission spectroscopy on WTe_2**
Mauro Fanciulli, Jakub Schusser, Min-I Lee, Zakariae El Youbi, Olivier Heckmann, Maria Christine Richter, Cephise Cacho, Carlo Spezzani, David Bresteau, Jean-François Hergott, Pascal D'Oliveira, Olivier Tcherbakoff, Thierry Ruchon, Jan Minár, and Karol Hricovini. (Phys. Rev. Research 2, 013261 (2020), DOI: 10.1103/PhysRevResearch.2.013261).

4. **Angle-resolved photoemission calculations of WTe_2 compared to experiment**
Jakub Schusser, Laurent Nicolaï, Mauro Fanciulli, Min-i Lee, Zakariae El Youbi, O. Heckmann, M. C. Richter, J. Minar, K. Hricovini. (AIP Conference Proceedings 2131, 020041 (2019), DOI: https://doi.org/10.1063/1.5119494).

5. **Origin of the spin-polarized photocurrent in a system with time-reversal and spatial inversion symmetries**
Jakub Schusser, Mauro Fanciulli, Zakariae El Youbi, O. Heckmann, M. C. Richter, C. Cacho, J. Minar, K. Hricovini. (in preparation).

Contents

List of Figures

To my beloved father

Introduction and Layout

Since the successful exfoliation of graphene, two-dimensional (2D) materials have attracted extensive interest due to their excellent electrical, thermal, mechanical, and optical properties. Although it has been the most explored in the 2D family, the zero band gap in graphene has been a major limitation to revolutionise its applications in electronic device [1]. Transition metal dichalcogenides (TMDs), another 2D family which has attracted intensive research and development in recent years due to their rich and fertile physical, chemical and electronic properties (Fig. 1). The possesion of a non-zero band gap and the possibility of its tuning as a function of the material thickness, as well as the opportunity to form heterojunctions with other materials make this family a very suitable candidate for solar energy harvesting, conversion and storage via photovoltaics and photocatalytic hydrogen evolution (PHE) reaction [2, 3, 4, 5]. Furthermore, the possibility to lift the spin-degeneracy without magnetism through inversion symmetry breaking in combination with spin-orbit coupling was a magnificent achievement, alongside the possession of topological features such as Dirac and Weyl points, nodal lines, Fermi arcs an other topological features have offered new routes to use information carriers other than charge, such as spin [6] and valley-pseudospin. These effects are now experiencing a resurgence in condensed matter in pure academic research and technological applications such as spintronics and valleytronics.

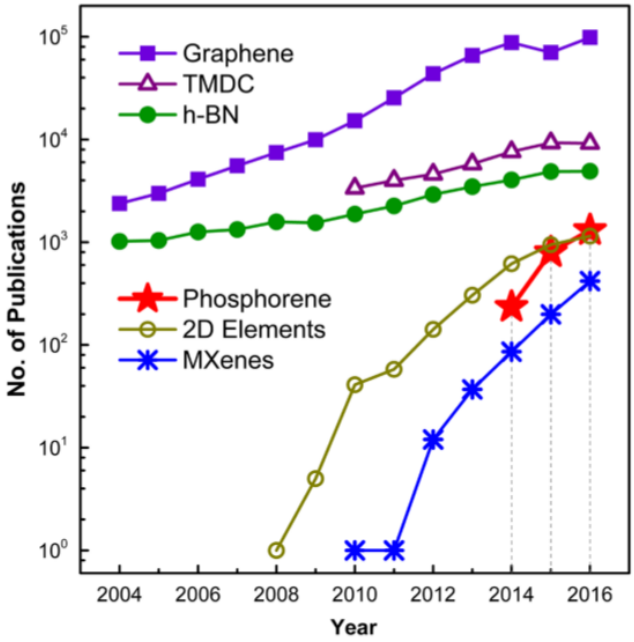

FIGURE 1: **2D materials**. Number of published articles during a decade [7].

In addition to the non-zero gap, their high electron mobility has offered them as

a potential solution for switching device applications such as field effect transistor (FET), for which the current design has come to a limit, notably physically, since the increasing transistor density due to further miniaturisation (i. e. modern transistors approach the quantum limit) has lead to crucial heat dissipation problems [8] and tunneling effects, causing them to fail.

One approach to bypass these thermal losses is to implement materials with much better electronic conductivity, shedding automatically light on superconductors, a family of a large number of metallic elements and compounds, characterized by zero resistivity below a transition temperature, making them excellent candidates. Since their discovery in 1911 by Kamerlingh Onnes [9] and the Nobel prize awarded in 1957 to Bardeen, Cooper and Schreiffer (BCS), who provided a theoretical description of the phenomenon, consisting of the pairing of electrons induced by a weakly attractive interaction mediated by phonons, a great number of superconducting materials was found and characterized, however, the lack of a superconductor with a transition temperature close to room temperature yield to their unlikely consideration, so far, as a solution to prevent the stagnation of device development (e. g. high-temperature copper-oxide superconductors hold a record of a transition temperature of 113K at atmospheric pressure [10]).

In the following part a breakdown of how this thesis will unfold:

Chapter 1 starts with some of the important and relevant (for this thesis) concepts in condensed matter physics, notably the behaviour of electrons in solids and the theory of bulk and surface electronic structures, being the foundation for the experimental results in this work. Relativistic effects such as spin-orbit coupling and Rashba effect are also emphasized, alongside the global lattice symmetries and their importance in shaping the electronic band structure of a material. The Dirac cones are introduced from a simplified tight-binding model of graphene, followed by the perturbations arising from spin-orbit coupling and inversion symmetry breaking, resulting in a finite band gap in the TMDs. A full description of the crystalline and electronic structure of TMDs is given, highlighting most of the recent achievement relevant for this thesis including the spin-texture, the topological features arising from within a single manifold and the origin of the novel electronic states in this family.

Chapter 2 is dedicated to angle-resolved photoemission spectroscopy (ARPES), being the main experimental technique used during this thesis, giving insights on the underpinning theoretical framework of the photoemission process as well as some important practical considerations.

Chapter 3 begins with an overview of the crystalline structure of $HfTe_2$ and underlying symmetries, followed by a literature review of the most relevant findings to this work, with a focus on the transport properties, being a part of the motivation to study this system. Insights on the used density functional theory (DFT) calculations approach and its merits will be explained, followed by the obtained results from the experimental investigations on the electronic band structure of pristine $HfTe_2$. The possible scenarios of dosing a layered material with alkali metals are given in details, and the factors favouring each of them are thoroughly explained, followed by the results obtained from our potassium K dosing sequences on the $HfTe_2$ surface, resulting in the emergence of a monolayer-like electronic structure, evidencing the

intercalation of the K atoms within the van der Waals gaps and then isolating the topmost layer. This chapter finishes by highlighting the topological features in the valence band of $HfTe_2$, analogous to other materials in the same space group.

Chapter 4 starts by recalling the peculiarity of 2H-Nb_2 as an exception in the metallic family of TMDs, since it is the only material which hosts a superconducting phase without a charge density wave (CDW). Electron-phonon and electron-electron interaction as the origin of the novel electronic states in TMDs will be introduced, showing their effect on the spectral function. Previous works performed on the superconducting nature as well as the surprising absence of a CDW phase in 2H-NbS_2 are reported. Our obtained results on the electronic band structures of both the 2H and 3R phases of NbS_2 will be shown, which, although have different crystalline structures, they are expected to have lots of similarities in the electronic structure as the DFT calculations would suggest. Our measured data, however, reveal striking differences between the two phases which we attribute to additional Nb interstitials in 3R-NbS_2, explaining the remarkable difference in the electronic structure of this phase and putting it away from any instabilities. Furthermore, we revisit the origin of the band splitting present in each phase, backed with our high resolution data. The chapter finishes by the experimental evidence of the momentum-dependent strong electron-phonon coupling and its direct link to the superconducting gaps distribution in 2H-NbS_2.

The last part provides a summary of the performed work, drawing the most important conclusions and giving perspectives to the findings in this work, opening routes for the possible further investigations to gain more insights on some of the interesting phenomena which could not have been accomplished within the framework of this thesis.

Chapter 1

Scientific Background and Materials of Interest

This chapter begins with a brief discussion of the theory of electronic band structure, which will serve as the foundation for experimental results discussed in this thesis, as well as an overview of the bulk and surface electronic structures of a solid. Relativistic effects such as spin-orbit coupling and Rashba effect will be introduced, alongside with the importance of global lattice symmetries.

Subsequently, a short introduction about the huge interest into 2D materials in the last few years, following the successful exfoliation of graphene will be given. The crystal and electronic structure of graphene will be shown, with the Hamiltonian describing the near Fermi-level band dispersion around K point, resulting in a linear band dispersion which gives rise to Dirac cones at the Brillouin zone corners. Furthermore, additional terms in the Hamiltonian near the K point, which refer to the inversion symmetry breaking in monolayer 1H-TMDs and spin-orbit coupling are introduced, opening thus the gap and resulting in the spin-valley locking in these materials. Also, the physics underpinning the diversity accross the TMDs family are highlighted, including the structural phase of the system and the schematic overview of its electronic band structure.

Other polytypes of the TMDs are described, notably the 1T and 3R counterparts, discussing some of their attractive electronic properties such as the topologically non-trivial states and the valley dependent spin-polarized states, respectively. This chapter completes with an introduction to the variety of instabilities in the TMDs, including Mott-insulating phase, charge density wave an superconductivity, emphasizing the many-body interactions as the origin of these novel electronic states.

1.1 Scientific background

1.1.1 Electronic structure

The electronic structure is the anchor to understand the behaviour of electrons in solids through a network of bands, the *electronic band structure*. The shape of the electronic band structure reflects many of the physical properties of the system, from superconductivity, charge density wave (CDW) to novel forms of topology, since it covers information about charge, spin and quasiparticle correlations. Therefore, the discovery and development of new materials with exotic properties requires a disentangled understanding of their electronic structure.

Electronic phenomena and band structure are one of the most important branches in condensed matter physics. A keystone to get access to such information is the many-particle Schrödinger equation:

$$H|\Psi\rangle = E|\Psi\rangle \tag{1.1}$$

where Ψ is the wavefunction of the electrons in the solid with E their energy, while H represents the Hamiltonian of the system, which describes the kinetic energy and Coulomb interactions between the electrons and the lattice ions. However, to get a good approximation of the electronic structure, it is not always necessary to consider all interactions within the lattice. Some assumptions are thus often made to simplify the solution.

The first assumption consists to combine the interaction of each electron with the lattice into a single potential, $V(\mathbf{r})$, since the electron dynamics are much faster than lattice dynamics (the electrons are independent; the adiabatic approximation) [11, 12]. The second assumption is the so called "one electron approximation", which dictates that all the electrons experience the same potential $V(\mathbf{r})$ [11, 12].

The Hamiltonian becomes thus the time-independent Schrödinger equation and can be written as:

$$\hat{H}(\mathbf{r}) = -\frac{\hbar^2}{2m}\boldsymbol{\nabla}^2 + V(\mathbf{r}) \tag{1.2}$$

with

$$V(\mathbf{r}) = V(\mathbf{r} + \mathbf{R}) \tag{1.3}$$

where m is the electron mass, $\mathbf{r}$ is the position vector of the electron, $\hbar$ is the reduced Planck constant and $\mathbf{R}$ is the lattice vector.

The periodicity of the potential $V(\mathbf{r})$ enforces that the solutions for the problem must also satisfy the periodicity condition. The wavefunctions $\Psi(\mathbf{r})$ can then be described by Bloch functions (modified plane waves) and can be written as follow:

$$\Psi(\mathbf{r} + \mathbf{R}) = \exp(i\mathbf{k}\mathbf{R})\Psi(\mathbf{r}) \tag{1.4}$$

To find the corresponding eigenstates for Eq. 1.1, which will provide the electronic band structure, two of the main used approaches are the nearly-free electron model and the tight binding model (TBM). In the nearly-free electron model the crystal potential $V(\mathbf{r})$ is considered as a weak perturbation, while it is treated as a strong perturbation in the TBM, where electronic states are assumed to be mostly localised to individual atoms (i.e. electrons are *tightly bound* to the lattice).

The tightly bound core electrons are strongly localised to the constituent atoms and thus have negligible dispersion. On one hand, the loosely bound valence electrons lie in large orbitals which have a great overlap (hopping strength) with neighbouring atoms within the unit cell. These orbital overlaps contribute directly to the bands dispersion in a solid and hence to its electronic properties. For instance, solids are formed by the bonding of these electrons across atomic sites, either covalently or ionically, where electron pairs are shared or fully transferred between atomic sites,

respectively. Consequently, the shape of the electronic structure is fundamentally governed by the crystal structure, since it reflects its periodicity and the orbitals distribution and their relative overlaps within the unit cell.

As shown in Fig. 1.1, obtained from a simplistic tight-binding model of graphene, the bandwidth of the p_z-derived bands depends purely on the hopping strength of the p_z orbitals "t_{p_z}"; or in other words, the degree of overlap between neighbouring p_z orbitals. Analogously, in a three-dimensional material where the band structure depends on both the in-plane $k_{x,y}$ and out-of-plane k_z momentum, the band dispersion along each direction is defined by the hopping strength of the corresponding orbitals. The manipulation of such hopping and its control with neighbouring unit cells in layered materials leads to a rich display of coexisting topological states and phases [13] as it will be explained in details later.

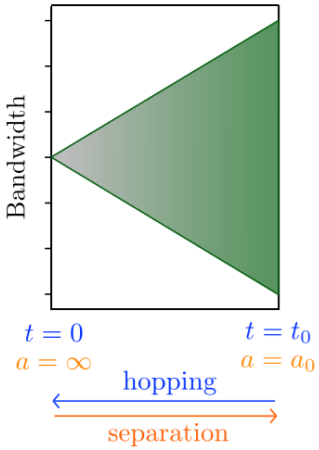

FIGURE 1.1: Bandwidth of the p_z derived bands in graphene as a function of hopping strength, where $t = 0$ corresponds to infinitely separated atoms ($a = \infty$) [14].

Density functional theory (DFT), the exclusive theoretical approach used in this thesis, establishes the ground state electron density, $\rho(\mathbf{r})$, of a many electron system as the relevant physical quantity, from which all information about the system can be obtained [15]. This is founded on the principle that the ground state electron density uniquely identifies the potential experienced by the electrons, determining thus the ground state wavefunction (first Hohenberg-Kohn theorem) [15]. This consequently gives some evidence that by minimising the total energy of the system, the ground state wavefunction can be acquired.

The second Hohenberg-Kohn theorem states that the total energy is a function of the electron density, which itself is a function of $\mathbf{r}$ only [15]. This thereby significantly simplifies the computational cost of DFT and offers the ability to handle large solids, molecules and atoms.

DFT solutions are expressed as linear combinations of a complete set of basis functions. In principle the set of basis functions is infinite, making the exact solution analytically impossible, but an approximation can be made using a limited number of wavefunctions corresponding to a subset of the atomic orbitals.

Although predominantly used in ARPES community as it successfully reproduces the electronic band structure of a system, standard DFT unrealistically understimates the band gaps and bandwiths [16]. This is improved using functionals such as the modified Becke-Johnson (mBJ), Heyd–Scuseria–Ernzerhof (HSE) exchange-correlation functional and GW approximation [17, 18, 19]. The mBJ functional was used in this work, and the details about its merit will be given in Chapter. 3.

Several commercial packages have been developed using DFT. Here, the WIEN2k package [20] was used by Dr. Matthew D. Watson to reproduce the measured electronic band structures for 1T-$HfTe_2$, 2H-NbS_2 and 3R-$Nb_{1+x}S_2$.

1.1.2 Surface states

The above subsection gives a simple description of the bulk electronic structure of a solid. However, since the investigated crystals have a surface, it is essential to study the electronic states confined to these surfaces, because surface states SS can have fundamentally different properties to their bulk counterparts.

As demonstrated above, the k-dependence of a given electronic band is defined by the periodicity of the potential, V($\boldsymbol{r}$). However, this periodicity is lost at the surface, and the potential inside the solid $V(\boldsymbol{r})_{z<0}$ must match somehow the constant vaccum potential $V(\boldsymbol{r})_{z>0} = V_{vac}$. Therefore, the Bloch plane wave solutions to the Schrödinger equation in the bulk ($z < 0$) are not valid at the surface ($z = 0$) due to the broken translational symmetry along the z direction.

For instance, since the Bloch plane wave solutions within the solid cannot exist outside, the resulting behaviour is an exponential decay upon reaching the potential barrier into the vaccum at the surface (Fig. 1.2(a)). Nevertheless, bulk solutions must obey the boundary conditions matching the wavefunctions inside the solid (plane wave, $z < 0$) to the wavefunctions outside (exponential decay; $z > 0$) by assuming the plane wave to be a superposition of the incident and reflected Bloch function [21, 22]. The wavefunctions inside and outside the solid will have, respectively, the following form:

$$\psi_{solid} \sim A\exp(ik_z z) + B\exp(-ik_z z)(z < 0) \tag{1.5}$$

and

$$\psi_{vaccum} \sim C\exp(-z)(z > 0) \tag{1.6}$$

where A, B, and C are constants. The continuity conditions are satisfied as follow:

$$\psi_{solid}(z = 0) = \psi_{vaccum}(z = 0) \tag{1.7}$$

and

$$\frac{d\psi_{solid}}{dz}(z = 0) = \frac{d\psi_{vaccum}}{dz}(z = 0) \tag{1.8}$$

Empirically, a plane wave with a complex wavevector could satisfy these continuity conditions, such that the wavefunction inside the solid $\propto \exp(ik_z z)$ is also real. This imaginary wavevector then produces an exponential decay into the bulk as well

as into the vacuum, implying that the amplitude of the wavefunction goes to zero away from the surface both into the solid and the vacuum. Solutions of this form are *surface states* (Fig. 1.2(c)).

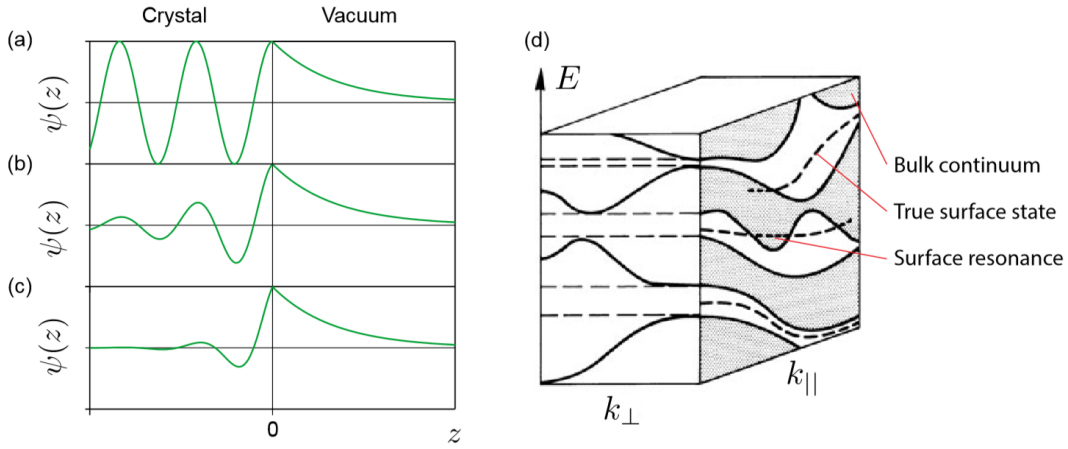

FIGURE 1.2: Electronic wavefunction at the sample surface for a bulk band (a), a surface resonance (b) and a surface state (c). $z < 0$ corresponds to the solid and $z > 0$ is the vaccum [14]. (d) Schematics of bulk-surface wavefunction overlap in a three dimensional band structure [21]. Solid lines correspond to bulk bands, shaded regions represent the projected bulk continuum states while white areas are band gaps. Surface solutions which exist within the band gaps and do not degenerate with the bulk continuum are true surface states, otherwise they are described as surface resonances.

Given the bulk solutions have strictly real k-vectors, the complex wave vector of the surface states does not allow their degeneracies with those of the bulk, and then surface states can only exist within bulk band gaps. In other words, if surface states existed at the same energies as bulk states (which have solutions with real momenta only), these SS could not have imaginary momenta and would not yield an exponential decay into bulk. Therefore, imaginary momemtum solutions can only exist where there is not already a real momentum solution, hence surface states must live in bulk band gaps.

Surface states do not disperse in k_z and can only have in-plane momentum $\boldsymbol{k}_{||}$ due to their localisation to the 2D surface plane. However, since surface states are imposed to be in bulk band gaps, they can exist exactly with bulk bands at some k_z and thus degenerate with the projected bulk continuum states (Fig. 1.2(b),(d)). The result is a *surface resonance* (Fig. 1.2(b),(d)) which extend deeper into the bulk (i.e. more spatially delocalised) than a 'true' surface state [21]. The experimental creation of surface states in a 3D electronic band structure will be shown in details in Chap. 3, where the intercalation of alkali metal atoms into the van der Waals gaps results in a quasi-free standing monolayer, with the wavefunction confinement to the topmost layer.

1.1.3 Spin-orbit coupling

Spin-orbit coupling has become a key element in condensed matter physics. It enters as a relativistic correction to the Schrödinger equation and can be considered as an "*internal Zeeman effect*". For instance, depending on the electron spin, the energetic splitting of an electron system in a magnetic field can be $\pm\boldsymbol{\mu}.\mathbf{B}$, where $\boldsymbol{\mu}$ is the magnetic moment and $\mathbf{B}$ is the magnetic field.

Analogically, when considering the oversimplified picture of an electron with velocity $\boldsymbol{v} = \boldsymbol{p}/m$ orbiting a nucleus, the electron experiences an electric field , $\boldsymbol{E}(\boldsymbol{r})$, from the positive Coulomb potential of the nucleus. The Lorentz transformation of $\boldsymbol{E}(\boldsymbol{r})$ is the effective field experienced by the orbiting electron in the rest frame and therefore, the electron experiences a magnetic field which can be expressed as $\boldsymbol{B} = -\boldsymbol{v} \times \frac{\boldsymbol{E}(\boldsymbol{r})}{c^2}$. The resulting energy shift is:

$$-\boldsymbol{\mu}.\mathbf{B} = -\frac{\hbar e}{(mc)^2}\boldsymbol{\sigma}.(\mathbf{E} \times \mathbf{p}) \tag{1.9}$$

with $\boldsymbol{\sigma}$ the Pauli matrices, m the electron mass and $\boldsymbol{E}$ the size of the electric field within the solid. From Eq. 1.9, it is evident that spin-orbit coupling consequently gives rise to a momentum-dependent spin mixed term when operating on a two component plane wave wavefunction.

Nevertheless, for a complete picture of quantum mechanics, capturing spin-orbit coupling and other relativistic effects, the Dirac Hamiltonian should be considered, which can be written as follow:

$$\hat{H}_D = c\boldsymbol{\alpha}.\mathbf{p} + \beta mc^2 + V(\mathbf{r}) \tag{1.10}$$

where $i \in \{x, y, z\}$ and

$$\alpha_i = \begin{pmatrix} 0 & \sigma_i \\ \sigma_i & 0 \end{pmatrix} \qquad \beta = \begin{pmatrix} I_2 & 0 \\ 0 & -I_2 \end{pmatrix} \tag{1.11}$$

Following the Foldy-Wouthuysen transformation [23], and taking into account the complete relativistic corrections, for a hydrogen-like atom with a spherical central potential, the resulting Dirac Hamiltonian can be written [24]:

$$\hat{H}_D = \underbrace{\frac{\boldsymbol{p}^2}{2m} + V(\boldsymbol{r})}_{\textit{non rel.}} \underbrace{- \frac{\boldsymbol{p}^4}{8m^3c^2}}_{\textit{mass corr.}} \underbrace{- \frac{\hbar^2}{4m^2c^2}\frac{dV}{\partial r}\frac{\partial}{dr}}_{\textit{Darwin term}} + \underbrace{\frac{1}{2m^2c^2}\frac{1}{r}\frac{dV}{dr}\boldsymbol{L}.\boldsymbol{S}}_{\textit{spin-orbit coupling}} \tag{1.12}$$

where the first and second terms are the non relativistic part, representing the kinetic energy and potential term of the Schrödinger equation, respectively. The third term accounts for a variable mass, while the fourth term is the Darwin correction, which corresponds to changes in electron-nucleus interactions resulting from the quantum oscillations of the electrons (i.e. the non-local influences of the Coulomb interactions). The last term is the spin-orbit coupling, which can be written as:

$$\hat{H}_{SOC} = \frac{\mu_B}{\hbar mec^2}\frac{1}{\mathbf{r}}\frac{\partial V}{\partial r}\boldsymbol{L}.\boldsymbol{S} \tag{1.13}$$

with $\mu_B = \frac{\hbar e}{2m}$ being the Bohr magneton, $\boldsymbol{S} = \frac{1}{2}\hbar\boldsymbol{\sigma}$ and:

$$\boldsymbol{L.S} = \frac{\hbar^2}{2}(j(j+1) - l(l+1) - s(s+1)) \tag{1.14}$$

This equation empirically shows the coupling of spin and orbital angular momentum quantum numbers. For instance, spin-orbit coupling mixes the orbital character, and any additional intrinsic or extrinsic electric fields to the atomic spin-orbit coupling will yield further spin-orbit corrections, such as the Rashba-type spin-splitting [25], which results from the inversion symmetry breaking along the z-axis at the surfaces and interfaces, or the Dresselhaus-type spin-splitting [26], which arises in bulk systems lacking an inversion centre.

The strength of the spin-orbit coupling is highly dependent on the chemical element's atomic number ($SOC \propto Z^4$ [27]), meaning that spin-orbit corrections are larger for the valence electrons of heavier atoms. Furthermore, d-orbitals derived electronic bands can experience larger spin-orbit corrections than p-orbitals derived bands, as the spin-orbit coupling is larger for larger l. However, to lift the spin degeneracy (electrons with $m_s = \pm\frac{1}{2}$), a breaking of either *inversion symmetry* (IS) or *time-reversal symmetry* (TRS) is required.

1.1.4 Time reversal and inversion symmetry

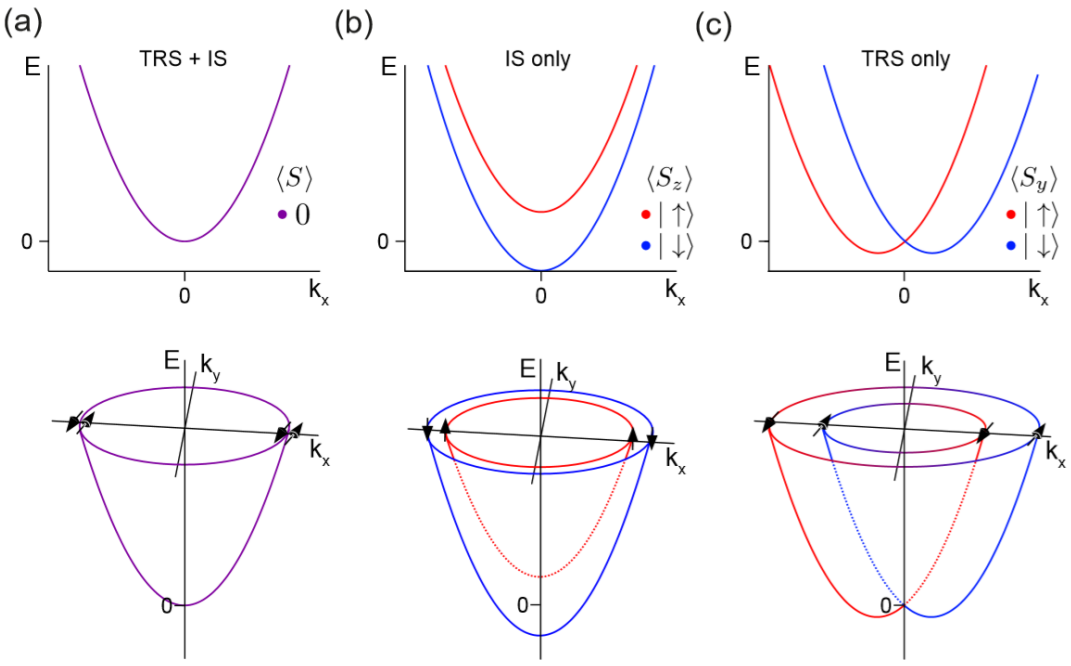

FIGURE 1.3: Effect of TRS and IS breaking on the band structure of a free-electron gas. (a) A typical 2DEG dispersion following $E \propto \mathbf{k}^2$, preserving both TRS and IS. Spin-degeneracy is lifted by the violation of TRS (b) or IS (c), resulting in a Rashba-type splitting in the latter case [14].

The presence of both time reversal and inversion symmetry dictates the energy degeneracy (i.e. Kramer's degeneracy) of electronic states with the same orbital wavefunction but opposite spins.

Time-reversal symmetry (TRS) holds for non-magnetic materials and forces spin-degeneracy at the so called time-reversal invariant momentum (TRIM) of the Brillouin zone. For instance, Kramer's theorem states that for every energy eigenstate of a time-reversal symmetric system with half-integer total spin such as an electron, there is at least one more eigenstate with the same energy. In other words, every energy level is at least doubly degenerate if it has a half-integer spin.

$$E(\boldsymbol{k},\uparrow) = E(-\boldsymbol{k},\downarrow) \tag{1.15}$$

Another fundamental symmetry is that of inversion symmetry (IS). IS means the existence of a center of inversion about which the unit cell of a system is invariant under the transformation $\boldsymbol{r} \rightarrow -\boldsymbol{r}$, such as the body-centred cubic structure of sodium or the hexagonal structure of transition metal dichalcogenides (TMDs), where $\boldsymbol{r}$ is a real space position in the crystal. In analogy to the $\boldsymbol{r} \rightarrow -\boldsymbol{r}$ transformation in real space, the $\boldsymbol{k} \rightarrow -\boldsymbol{k}$ transformation in reciprocal space occurs and hence for every state in the Brillouin zone the inversion symmetry dictates:

$$E(\boldsymbol{k},\uparrow) = E(-\boldsymbol{k},\uparrow) \tag{1.16}$$

It is apparent that the presence of both TRS and IS (i.e, the combination of equations 1.15 and 1.16, $E(\boldsymbol{k},\uparrow) = E(-\boldsymbol{k},\uparrow) = E(\boldsymbol{k},\downarrow) = E(-\boldsymbol{k},\downarrow)$) enforces the spin-degeneracy of all the states in the Brillouin zone. Therefore, spin-orbit coupling cannot give rise to a spin splitting within systems that are simultaneously time-reversal and inversion symmetric.

As has been demonstrated, the chemical composition and crystal structure represent the key foundation to the electronic structure of materials. For instance, in a non-magnetic system (i.e. TRS is upheld) where the lattice is constructed of light atoms (i.e. negligible SOC) with cubic symmetry, the three p-orbital derived bands are degenerate at the Brillouin zone center Γ, each of which is doubly spin-degenerate. However, if the system is composed of heavy atoms such as those of the transition metals, SOC is significant and results in a splitting of $p_{1/2}$ and $p_{3/2}$ orbital derived bands, with spin-degeneracy is still present for each band. Finally, if the crystal lattice is changed in a way that the inversion symmetry is broken, the spin-degeneracy will be lifted and thus each electronic band is spin-polarised, except at time-reversal invariant momentums (TRIM points) such as Γ, where TRS enforces $E(\boldsymbol{k},\uparrow) = E(-\boldsymbol{k},\downarrow)$. The existence of TRS also dictates the total spin-polarisation of the system to be zero, with no preferred direction as for every spin-up electronic state, there is a spin-down state at opposite $\boldsymbol{k}$ in the Brillouin zone.

In the case of magnetic materials (Fe, Cr...), an asymmetry in the population of electronic spins (i.e. a shift in energy of the density of states of spin-up vs spin-down) known as an exchange splitting develops (i.e. more up-spins than down-spins). This spin-population imbalance breaks time-reversal symmetry and therefore, for a state with spin-majority at $\boldsymbol{k}$, there is no corresponding state with spin-minority at -$\boldsymbol{k}$ (Fig. 1.3(b)). Nevertheless, this thesis will focus entirely on non-magnetic materials (time-reversal symmetric), hence only inversion symmetry breaking is responsible of any spin-splitting shown here.

1.1.5 Rashba Effect

The principle of *Rashba-type* spin-splitting [25] can be described by considering a two-dimensional electron gas (2DEG) at a material surface or interface; free electrons propagating in the x-y plane but confined in z, formed from a gradient in the potential at the surface in the z direction. This effective electrostatic potential normal to the surface naturally provides the loss of inversion symmetry required by *Rashba-type* spin-splitting (Fig. 1.3(c)), even when the underlying crystal structure is inversion symmetric.

More precisely, the strong variation of the electrostatic potential near the surface results in the so called "near-surface band bending effects", a familiar scenario when dosing semiconductors with alkali metals [28, 29, 30, 31]. This band bending caused by the charge accumulation in the near-surface region yields the effective spatial confinement and emergence of quantum-well-like states. The band structures of these confined sub-bands therefore mimic the bulk, but without the constraints imposed by inversion symmetry. One of the most famous experimental realisations of *Rashba-type* spin-split quantum-well-states derives from the near-surface layers of Bi_2Se_3 [28, 29, 32], but sub-band states exist also in systems with residual surface charge or at the interface between two materials. More recently, the quantum confinement has been shown to exist in the semimetallic TMDC $PtSe_2$ as well, although the existence of both holelike and electronlike free carriers makes the underlying mechanism complex to predict [33].

Similarly, *Rashba-type* spin-splitting also exists in the surface electronic structure of any compound which hosts surface-localised states, since the inversion symmetry is naturally broken at the surface of a material. *Rashba-type* spin-splitting of the surface states was demonstrated by angle-resolved photoemission spectroscpy (ARPES) for Au(111), an inversion symmetric material and other noble metals such as Cu(111) and Ag(111) [34, 35, 36, 37, 38, 39].

Nevertheless, and directly related to the work presented here, *Rashba-type* spin-splitting can also exist in bulk systems lacking inversion symmetry, such as monolayer 1H-TMDs (1H-NbS_2, 1H-$NbSe_2$, 1H-WSe_2 and 1H-MoS_2) which exhibits an out-of-plane spin splitting around the K valleys resulting from the in-plane dipole within each single layer of their layered crystal structure [40, 41, 42, 43, 44, 45]. The inversion symmetry breaking ISB in 1H-TMDs, however, is local since the unit cell, formed by two monolayers rotated by 180° between each other (2H-TMDs) is inversion symmetric, as it will be explicitly described later, rather than the global ISB shown in the giant Rashba system BiTeI [46, 29, 47, 48].

1.2 Introduction to 2D materials

1.3 Graphene

The discovery of graphene has triggered an extensive rise in the study of two-dimensional materials [49]. As shown in its crystal structure (Fig. 1.4), graphene is composed by

a single sheet of carbon atoms on a two-site triangular lattice, resulting in a honeycomb structure. Both inversion symmetry and time-reversal symmetry are preserved in graphene, as a consequence of its crystalline structure and non-magnetism, respectively.

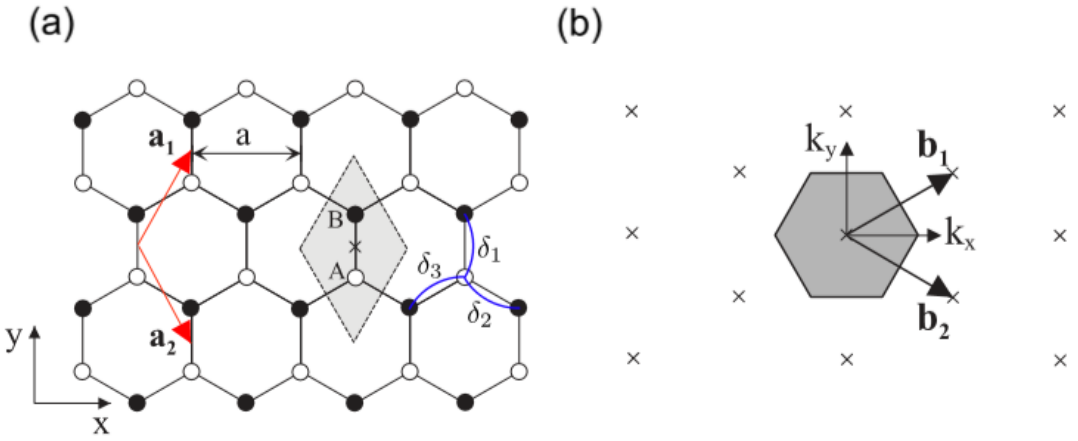

FIGURE 1.4: Real space and reciprocal space lattice of graphene [50]

with:

$$\mathbf{a}_1 = (\frac{a}{2}, \frac{\sqrt{3}a}{2}), \mathbf{a}_2 = (\frac{a}{2}, -\frac{\sqrt{3}a}{2}) \tag{1.17}$$

and:

$$\mathbf{b}_1 = (\frac{2\pi}{a}, \frac{2\pi}{\sqrt{3}a}), \mathbf{b}_2 = (\frac{2\pi}{a}, -\frac{2\pi}{\sqrt{3}a}) \tag{1.18}$$

The in-plane $2p_{x,y}$ orbitals form the σ-type bonding in graphene, while the low-energy band structure is π-type bonds, deriving from the out-of-plane orbitals $2p_z$. Therefore, it is sufficient to consider only the p_z orbitals in the Hamiltonian. There is then a p_z orbital from the A and the B sublattice (Fig. 1.4) forming a 2 x 2 Hamiltonian describing the bonding (π) and antibonding (π*) states. The diagonal terms describe the on-site energies, while off-diagonal terms describe hopping between orbitals.

$$H = \begin{pmatrix} \epsilon_A & -tf(\boldsymbol{k}) \\ -tf^*(\boldsymbol{k}) & \epsilon_B \end{pmatrix} \tag{1.19}$$

Where $\epsilon_{A,B}$ is the on-site energy for the A or B site, t is the hopping parameter, and $f(\boldsymbol{k})$ is the momentum dependence of the hopping.

The Hamiltonian can be diagonalised and solved as follows:

$$E_\pm = \frac{\epsilon_A + \epsilon_B}{2} \pm \frac{\sqrt{(\epsilon_A - \epsilon_B)^2 + 4t^2|f(\boldsymbol{k})|^2}}{2} \tag{1.20}$$

where E_- and E_+ are the bonding π and anti-bonding π* bands, respectively.

Since both A and B sites contain a carbon atom, and the honeycomb lattice of graphene possesses inversion symmetry, the on-site energies are equivalent to the on-site energy of the carbon $2p_z$ orbital where $\epsilon_A = \epsilon_B = \epsilon_{p_z}$. Thus, the eigenvalues are:

$$E_{\pm} = \epsilon_{p_z} \pm t|f(\boldsymbol{k})| \tag{1.21}$$

giving the dispersion of the π bands as illustrated in Fig. 1.5, where the degeneracy is enforced at the points where $f(\boldsymbol{k}) = 0$ ($E_{\pm} = \epsilon_{p_z}$).

The notoriety of the band structure of graphene is embodied in the Dirac cones at the corners of the Brillouin zone [51, 52, 53, 54]. As shown in Fig. 1.5, Dirac fermions are formed by the crossing of linearly dispersing bands at the K points, allowing graphene to host unique properties, such as a very high mobility on the order of $10^5\ cm^2V^{-1}s^{-1}$ [55], which corresponds to a low resistivity of $\sim 10^{-6}\ \Omega cm$. Another consequence of these Dirac cones in graphene is its possession of an unconventional integer quantum Hall effect [51, 56]. Adding to that a strikingly high thermal conductivity [57] makes graphene a material which may potentially revolutionize the next-generation electronic devices.

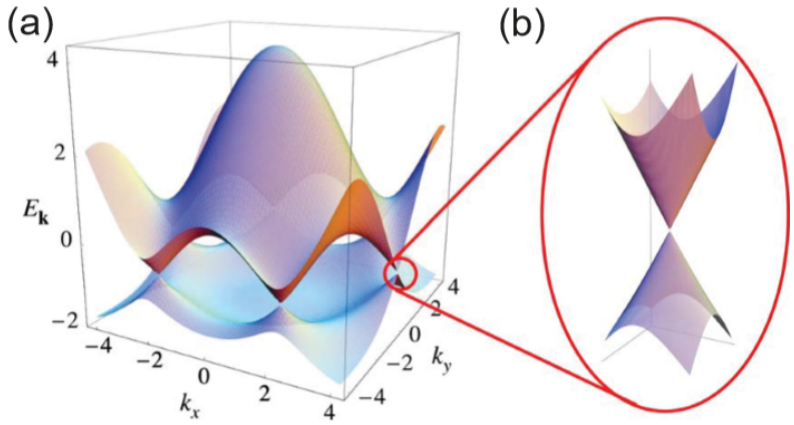

FIGURE 1.5: a). Electronic structure of the π-bands of graphene. b). Low-energy band dispersion around the K point showing the linear dispersion of the Dirac cone states [54].

The momentum dependence of the hopping is given by:

$$f(\boldsymbol{k}) = \sum_i e^{i(\boldsymbol{k}.\boldsymbol{\delta}_i)} = e^{ik_y a/\sqrt{3}} + 2e^{-ik_y a/2\sqrt{3}} cos(k_x a/2) \tag{1.22}$$

where the three hopping vectors from an A site to the nearest B site or vice versa are:

$$\boldsymbol{\delta_1} = (0, \frac{a}{\sqrt{3}}), \boldsymbol{\delta_2} = (\frac{a}{2}, -\frac{a}{2\sqrt{3}}), \boldsymbol{\delta_3} = (-\frac{a}{2}, -\frac{a}{2\sqrt{3}}) \tag{1.23}$$

As seen in Fig. 1.5, the degeneracy of the π bands occurs at the Brillouin zone corners (K points), this point can be obtained as follows:

$$(\mathbf{b}_1 + \mathbf{b}_2)/3 = \xi(\frac{4\pi}{3a}, 0) \tag{1.24}$$

where the valley index $\xi = \pm 1$. In momentum space, this distinguishes between K and K'(-K) Brillouin zone corners. Away from K_ξ, the momentum is $\mathbf{p} = \hbar\boldsymbol{k}$ - $\hbar K_\xi$,

which gives the hopping function:

$$f(\boldsymbol{k}) = e^{ip_y a/\sqrt{3}\hbar} + 2e^{-ip_y a/2\sqrt{3}\hbar} cos(\frac{2\pi\xi}{3} + \frac{p_x a}{2\hbar}) \tag{1.25}$$

by expanding and neglecting the higher orders in momentum, we get:

$$\approx -\frac{\sqrt{3}a}{2\hbar}(\xi p_x - ip_y) \tag{1.26}$$

The low-energy effective Hamiltonian for the states close to K_ξ is thus:

$$H_{K_\xi} = v \begin{pmatrix} 0 & \xi p_x - ip_y \\ \xi p_x + ip_y & 0 \end{pmatrix} \tag{1.27}$$

where $v = \sqrt{3}at/2\hbar$ is the particle velocity.

The effective Hamiltonian can be diagonalised to give two eigenvalues and eigenstates:

$$E_\pm = \pm vp, \psi_\pm = \frac{1}{\sqrt{2}} \begin{pmatrix} 1 \\ \pm\xi e^{i\xi\phi} \end{pmatrix} e^{ip.r/\hbar} \tag{1.28}$$

where ϕ is the in-plane velocity angle and $\boldsymbol{p}$ = (p_x, p_y) = p ($cos\phi$, $sin\phi$).

Then, a linear dispersion relation is obtained close to the K point, with the electronic states described as Dirac fermions with a velocity v.

The fact that there is a pseudospin which relates to the electron or hole density being localized to either the A or B sublattices, the effective Hamiltonian can be written as:

$$H = v(\xi\sigma_x p_x + \sigma_y p_y) \tag{1.29}$$

where σ_i refers to a Pauli matrix for the i^{th} component of the pseudospin.

The observation of Dirac cones in graphene has triggered a surge of interest in Dirac semimetals and topological insulators, since they are considered as the realisation of massless Dirac fermions in condensed matter physics. However, despite the wide range of novel physics in graphene [58, 59, 60], the gapless band structure limits its suitability for transistor-based devices, or any other applications which require semiconducting materials. Furthermore, the fact that both inversion and time-reversal symmetries are preserved in graphene makes this system less attractive for spintronic applications, due to the complexity to control the charge carriers.

This was the original reason behind the avalanche of studies on a related class of materials: Transition metal dichalcogenides TMDs. Unlike graphene, TMDs can possess both a lack of inversion symmetry (i. e. 1H phase) and a strong SOC, due to the large atomic size of the constituting elements. These, as explained earlier, consequently lead to a lifting of the spin-degeneracy of the states and a finite gap in the band structure, respectively. Since the research conducted within this thesis consists entirely of materials which belong to the TMD family, an extensive discussion is dedicated in the following section.

1.4 Transition metal dichalcogenides

Transition metal dichalcogenides (TMDs) are a class of layered materials that has been a cornerstone of condensed-matter physics research since the last century. Structures and properties have been reviewed by Wilson [61] as early as 1969, and electronic properties were reviewed by Yoffe [62]. Lieth, Balchin and Levy [63, 64] have summarized the preparation and crystal growth procedures, while Hulliger [65] has compiled extensive structural information. Phase transitions and charge-density waves were considered by Gamble and Geballe [66], whereas Whittingham [67] has reviewed the chemistry of intercalation [68].

TMDs form in the MX_2 stochiometry, where M represents almost any transition metal from group IV through X, and X stands for chalcogen elements from group XVI of the Periodic Table $\{S, Se, Te\}$ (Fig. 1.6).

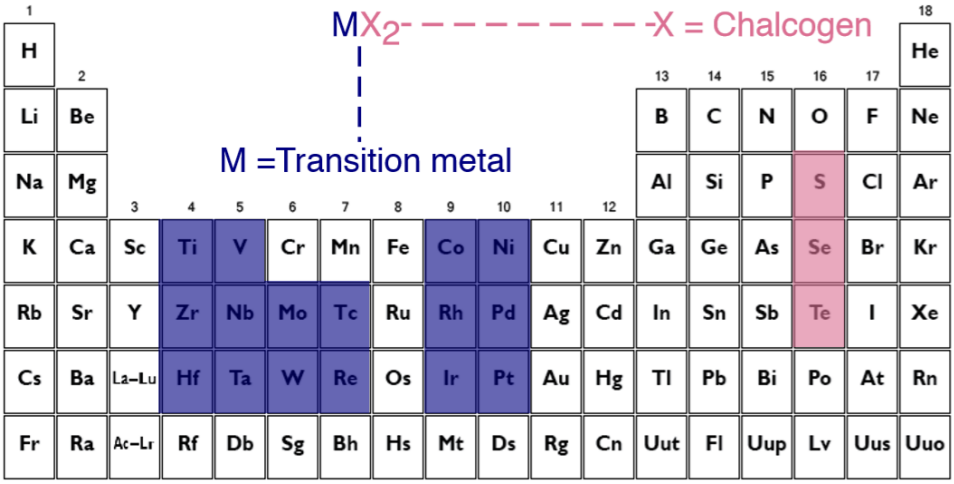

FIGURE 1.6: Periodic table of elements presenting some possible combinations of elements forming layered TMDs MX_2. Purple color indicates the transition metals (M), while chalcogens (X) are indicated by the pink color [69].

1.4.1 Atomic structure

A monolayer TMD is composed of a hexagonal layer of the transition metal atoms and two hexagonal layers of dichalcogenide atoms positioned above and below the the transition metal plane, resulting in the order X-M-X. Depending on their crystalline structure, TMDs can form either in the 2H, 1T, the 'distorted' 1T' and 3R phase, where the number denotes the number of layers within a unit cell, and T, H and R indicate the trigonal, hexagonal and rhombohedral structures respectively (Fig. 1.7).

Bulk TMDs consist of either covalently or ionically (i. e. depending on the transition metal configuration, which will be explained later) bonded quasi-two dimensional layers stacked along the c-axis in one of the orders described above, separated by the van der Waals gaps. The layered crystal structure adopted by these materials makes them exhibiting a highly anisotropic thermal, chemical and electronic properties [70,

71].

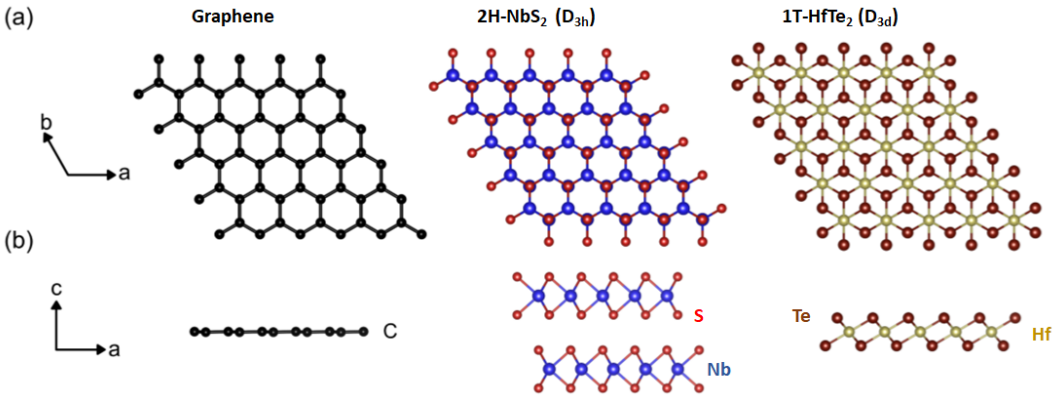

FIGURE 1.7: **Comparison of the crystal structure of graphene with that of the TMD family.** (a) top-view (c-axis projection) structures of graphene, 2H-NbS_2 and 1T-$HfTe_2$ from left to right. (b) side-view (b-axis projection) of the same three compounds. The number of layers shown indicates one full repeating unit along the c-axis.

1.4.2 Diversity across TMDs

The extensive avalanche in studying bulk TMDs in the last decade is a natural consequence of their rich and large electronic properties, range from insulating (HfS_2 [72, 73]), semiconducting (MoS_2 and WSe_2 [43, 42, 45]), semimetallic ($HfTe_2$, WTe_2, $PtSe_2$ and $PdTe_2$ [74, 61, 75]) to metallic ($NbSe_2$, NbS_2 and $TaSe_2$ [76, 77, 78, 79, 80]). These metals are well-known for hosting a variety of instabilities such as a charge density wave and superconductivity, arising from the interplay between electron-phonon and electron-electron coupling, making them a fertile playground of novel electronic states.

As summarized in Fig. 1.8, this diversity is predominantly owed to both the band filling of the transition metal and the point group symmetry, which dictates the thermodynamically favoured structural phase of the material [83, 70, 71]. In general, the electronic structure of TMDs consists of a valence band formed by the bonding σ and anti-bonding σ^* chalogen p-orbital manifolds, and a conduction band formed by the transition metal d-orbital manifold. Depending on the adopted structure phase by the system, the effect of the crystal field on the d-orbital manifold can be different.

For TMDs with the 2H (3R) crystal structure (primarly group-V and group-VI), which puts the transition metal ion in a trigonal prismatic coordination (D_{3h} point group symmetry), the d-orbital manifold is split into $[\{d_{z^2}\}, \{d_{x^2-y^2,xy}\}$ and $\{d_{xz,yz}\}]$ sub-manifolds. Group-VI TMDs, which have the transition metal in the (d^2) configuration, fully filling the lowest d_{z^2} band are thus semiconducting, such as MoS_2 and WSe_2. Whereas, group-V TMDs have the metal in the (d^1) configuration, leaving the d_{z^2} band half-filled, making them metallic, such as $NbSe_2$ and $TaSe_2$ [76, 84, 80].

For 1T-TMDs, where the transition metal ion undergoes an octahedral coordination (D_{3d} point group symmetry), preferred by group-IV, group-IX and group-X, d-orbital

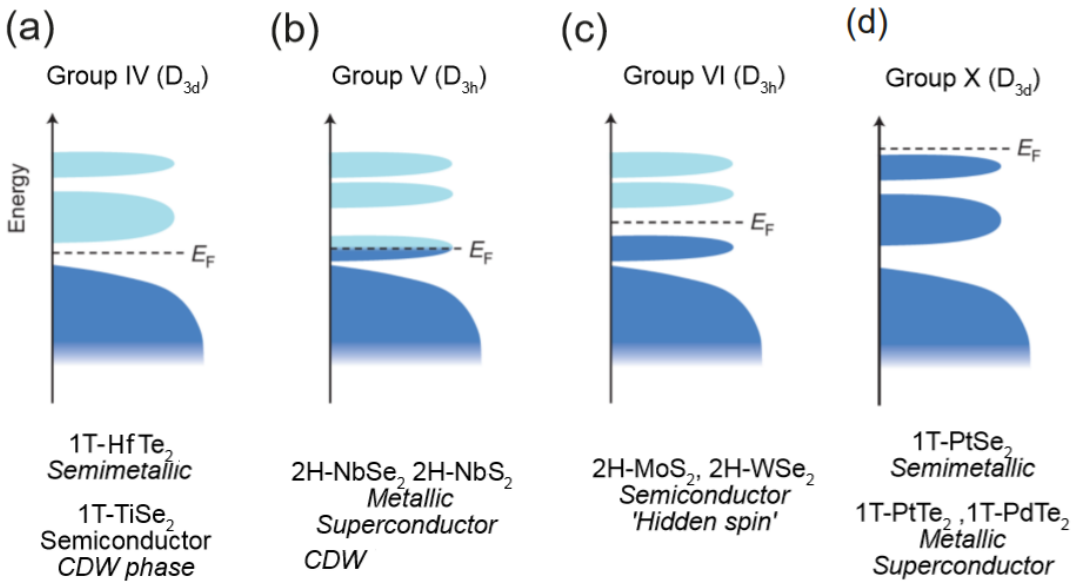

FIGURE 1.8: **Simplified electronic structures of transition-metal dichalcogenides.** Density of states diagrams with the relevant transition metal group and coordination indicated above. The filled bands are highlighted in dark blue while the unoccupied are in light blue. Adapted from [81, 69, 82, 14].

manifold is split into $[t_{2g} = \{d_{yz,xz,xy}\}$ and $e_g = \{d_{z^2}, d_{x^2-y^2}\}]$ sub-manifolds. Following the ionic distribution for TMDs where the transition metal belongs to group-IV of the periodic table (d^0 configuration), the oxidation states of the transition metal atom and the chalcogen atom are $+4$ and -2, respectively. In this case, the valence electrons (e.g. $2p^6$ for Se) fill the two bonding and antibonding chalcogen p-orbitals, resulting in a semiconducting electronic band structure such as $TiSe_2$ and $HfSe_2$ [85, 86]. This ionic picture, however, starts to break down as the d orbital filling progressively increases, leading to significant differences in the electronic band structure of these materials.

While the diagram in Fig. 1.8 presents a good way to understand the trends in the electronic structure within the TMDs class of materials, it is a simple interpretation which does not take into account other details that make the outlook more complicated, such as the orbitals hybridization, the band splitting and orbital mixing from the significant spin-orbit coupling in these materials. Such overlap between the transition metal d-orbitals and the chalcogen p-orbital can lead, in the case of $HfTe_2$ for example, to a semimetallic ground state with an band overlap (inverted band gap) of $\sim$ 0.2 to 0.3 eV, compared with the isostructural and isoelectronic HfS_2 which is an insulator.

1.4.3 Spin-texture in TMDs

Inversion symmetry breaking and spin-valley locking in 1H-TMDs

In graphene, the inversion symmetry is preserved, resulting in a spin-degenerate band structure (i. e. Kramer's degeneracy). In 1H-TMDs, however, the inversion symmetry is broken as can be seen in Fig. 1.9. This gives rise to finite band gaps

in the states analoguous to the Dirac points of graphene (K and K' valleys), and the effective Hamiltonian near the K points can be written as [87]:

$$H = at(\xi\sigma_x p_x + \sigma_y p_y) + \frac{\Delta}{2}\sigma_z \tag{1.30}$$

where a and t are the lattice and the hopping parameters, respectively, and $\mathbf{\Delta}$ is the energy gap opened from the sublattice symmetry breaking (the difference in on-site energies for the A and B sub-lattices).

This is, however, only a simplistic analogy drawn between graphene and TMDs to give straightforward insights, since this is now a multiorbital system with a completely different lattice and electron count.

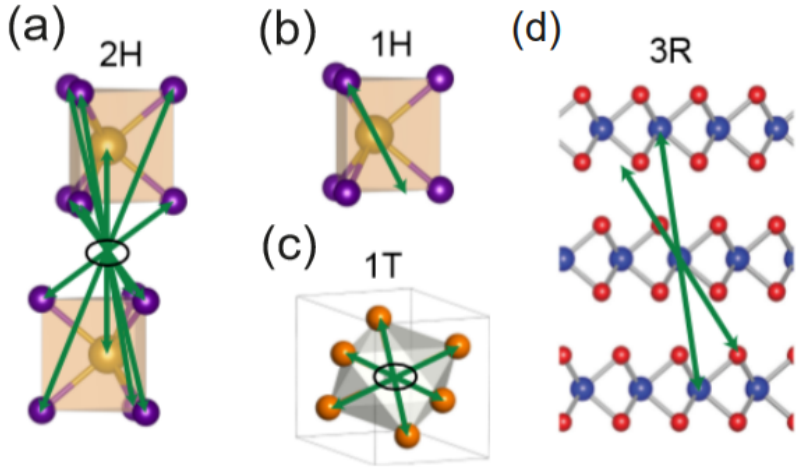

FIGURE 1.9: The stacking along the c-axis is shown for the a) 2H, b) 1H, c) 1T and d) 3R polymorphs. Green arrows represent the application of the inversion operator [82].

Furthermore, the d orbitals originating from heavy transition metals experience a much higher spin-orbit coupling than the electrons deriving from carbon $2p$ orbitals. This can further split the bands when lifting the spin degeneracy of the valence band maximum (VBM) at K and K' valleys, as permitted by the inversion asymmetric nature of the 1H-structure, and enhance the size of the band gaps. The effective Hamiltonian close to the K points, including spin-orbit coupling for a monolayer TMD, is therefore [87]:

$$H = at(\xi\sigma_x p_x + \sigma_y p_y) + \frac{\Delta}{2}\sigma_z - \lambda\xi\frac{\sigma_z - 1}{2}s_z \tag{1.31}$$

where the last term couples to the s_z component of the electron's spin, with a spin-orbit strength λ.

As indicated by the out-of-plane spin operator, the spin polarisation of the valence bands in monolayer $1H$-TMDs is entirely out-of-plane (s_z), due to the effective in-plane electrical dipole inherent to each X-M-X layer [40, 41]. It can be seen also from eq. 1.31 that the sign of the energy is governed by the valley index ξ. This gives rise to the so called "spin-valley locking", which exists only in monolayer TMDs where inversion symmetry is broken ($1H$ and $1R$ crystalline structures). Time-reversal symmetry relates the valence bands at the $K(\xi = 1)$ and $K'(\xi = -1)$ points, enforcing

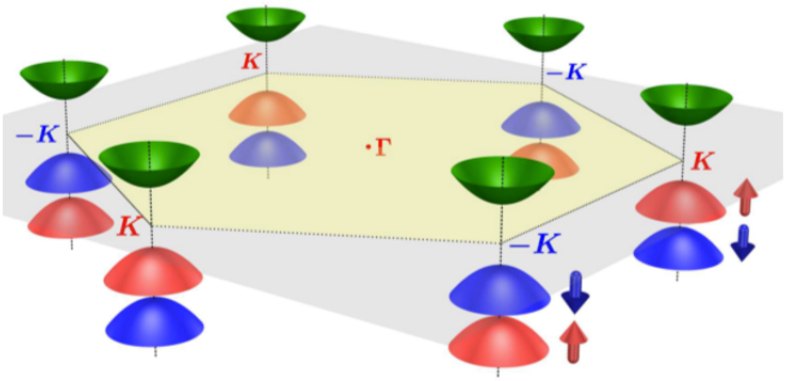

FIGURE 1.10: **Spin-valley locking in TMDs.** Low-energy electronic structure of a monolayer 1H-TMD near the zone corners [87].

that the spin-splitting has opposite ordering within each valley [87]. For example, as depicted in Fig. 1.10, the upper valence band at the K point (ξ=1) possesses a spin-up s_z while at the K' point (ξ=-1), the upper valence band possesses a spin-down s_z.

The surge of interest into monolayer transition metal dichalcogenides, especially 1H semiconducting variants, focused mainly on exploiting this spin-valley locking for manipulation of valley carriers and the study of the interplay between the pseudospin and spin degrees of freedom [88].

The use of circularly polarised optical fields has been a successful tool to selectively probe only electrons of a single spin type (either up or down). For an optical transition via the absorption of circularly polarised right (+) or left (-) light, the matrix elements can be approximated as: $|P_{\pm}|^2 \approx A(1 \pm \xi)^2$, where A is a constant [87]. In this regard, several optical and photoluminescence experiments have been carried out consisting of exciting excitonic transitions in these materials between the filled valence bands and unfilled conduction bands, using circularly polarised light [89, 87, 90, 91, 92, 40].

As illustrated in Fig. 1.11(b), for circularly polarised photons with an appropriate energy to the band gap between the upper valence band and the conduction band (ω_2), a choice of right σ^+ or left σ^- handed circular polarisation populates either the conduction band at K with spin down electrons, or the conduction band at K' with spin up electrons, due to the valley selection rules. The opposite is true for a photon energy corresponding to the energy separation between the lower valence band and the conduction band (ω_1).

The embodiment of this spin-valley locking plays a vital role in reducing the backscattering in these materials. In other words, the relaxation of an electron is most likely to occur through the same channel as it was excited, since intervalley scattering (from K to K' valley) requires a spin flip and (potentially) a large in-plane momentum, which are energetically less favourable, or even an unrealistically significant change in energy associated with the splitting of the upper and lower valence band, leading to robust valley coherence [93, 88]. Fig. 1.11(c) highlights the allowed and forbidden intervalley scatterings.

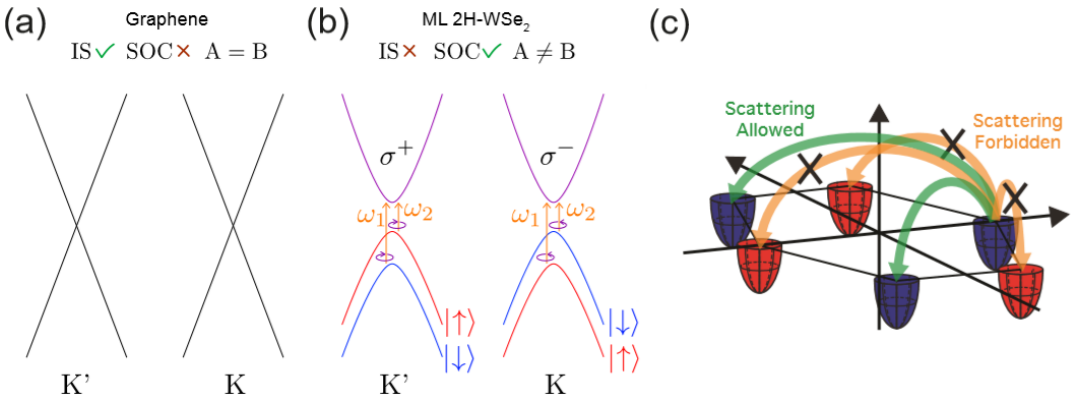

FIGURE 1.11: (a) Simplified band structure of graphene, where the band structure spin-degeneracy is preserved by the combination of time-reversal and inversion symmetry (IS). Sub-lattice symmetry and small spin-orbit coupling results in ungapped crossings at its K points. (b) Simplified band structure for monolayer WSe_2. A finite band gap with a spin-split VBM arise du to the inversion and sub-lattice symmetries breaking. The possible transitions at the K and K′ points are indicated. For example, exciting the sample with fixed energy $h\mu = \omega_1$ circularly-right polarised light (σ^+) will populate the conduction bands at K′ with spin-down electrons, with no excitations at K. For σ^- with $h\mu = \omega_1$ photons, the conduction bands at K with spin-up electrons will be populated, with no excitations at K′. The spin-picture is reversed for $h\mu = \omega_2$. (c) Spin-valley coupling reduces the propbability of backscattering events which require spin-flips [93].

Hidden spin-texture in 2H-TMDs

Bulk TMDs, however, exhibit important changes in their electronic structure. The VBM is shifted from the Brillouin zone corner at $K(K')$ to the zone center at Γ, while the CBM shifts from $K(K')$ point to Σ valley, a position partway between Γ and K. This results in a direct to indirect band gap transition when moving from monolayer to bulk TMDs [94, 95, 89, 96, 97, 98, 99, 100, 101, 102].

Due to the strong hopping along the c-axis of the orbitals from which the top and the shallow regions of the valence band at the Γ point are derived in the bulk electronic band structure, d_{z^2} in WSe_2 for example, the k_z dispersion of these bands is significant in the Brillouin zone center (along ΓA direction), as a consequence of the dimensionality increase in real space [70, 71, 42, 13].

Furthermore, in bulk $2H$-TMDs, the global inversion symmetry is restored. As shown in Fig. 1.9(b), the unit cell is formed by two monolayers which are rotated by 180° with respect to each other, establishing thus an inversion center between the two layers. As a result of both inversion symmetry and time-reversal symmetry, a total spin-degeneracy of the electronic states is expected.

Surprisingly, the spin-valley locking of the asymetric 1H monolayers still exists in their centrosymmetric $2H$ bulk counterparts [42, 44, 45]. This is a consequence of two major reasons. At the K points, the electronic wavefunctions have a strong 2D nature, due to the in-plane orbital character from which the bands are derived [103, 44], $d_{xy}, d_{x^2-y^2}$ in WSe_2, resulting in a great suppression of the interlayer hopping

(negligible k_z dispersion of these states). Due to the extreme surface sensitivity of an experimental method such as spin-ARPES, the measured spin-polarisation is predominantly localised to a single monolayer (the top layer) of the bulk 2*H*-TMDs (Fig. 1.12). In other words, only the local inversion asymmetry of a single *X*-*M*-*X* unit along the c-axis is probed [41]. However, in the regions where the bands are derived from orbitals with a strong interlayer hopping (p_z, d_{z^2}), the 3D extended nature of the electronic wavefunction experiences the global inversion symmetry being upheld, which, in addition to the time-reversal symmetry provides a lack of spin-polarisation of these electronic states (the Brillouin zone center).

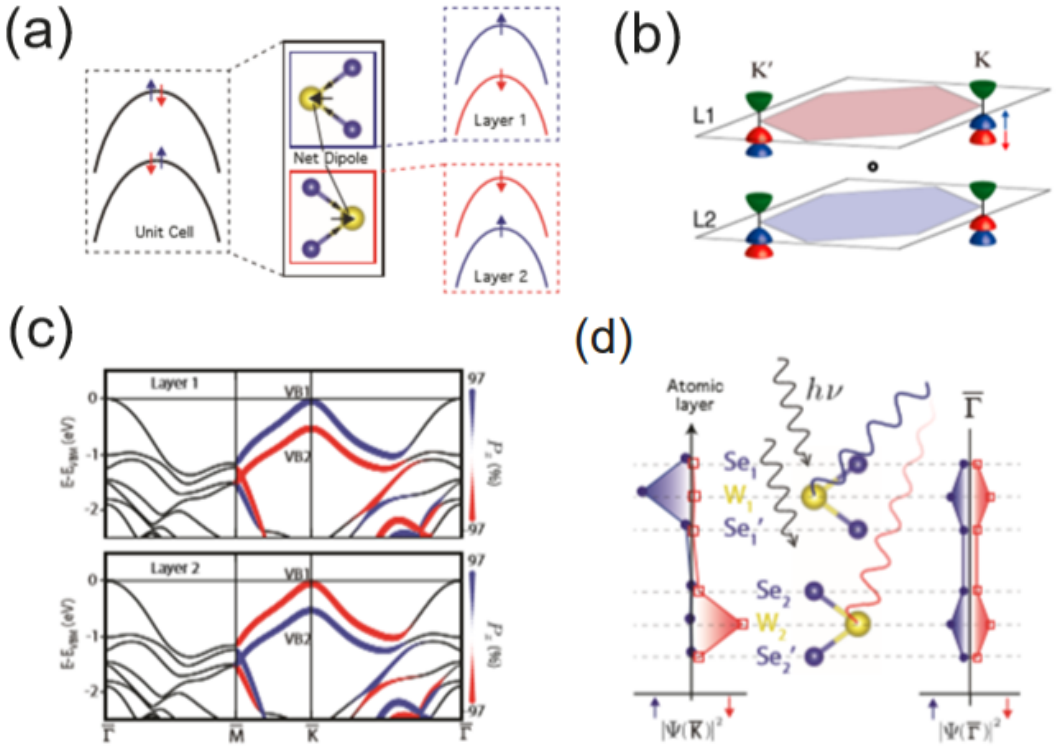

FIGURE 1.12: **Spin-valley-layer locking in inversion-symmetric TMDs.** (a). The sum over the unit cell dictates that all states are spin-degenerate, but due to a local breaking of inversion symmetry by the individual layers, out-of-plane spin-polarisations exists in each layer. The 180° rotation between each monolayer reverses the direction of the in-plane dipole and therefore the out-of-plane spin-polarisation. The red and blue arrows indicate out-of-plane spin polarizations. (b). Schematics for a low-energy pair of VB (red and blue) and CB (green) around two different valleys (K and K') and in two different layers (L1 and L2). The open circle denotes the inversion center of bilayer 2H-TMDs. (c) Projection of bulk band structure onto individual layers of the unit cell reveals a strong out-of-plane spin-polarisation of electronic states near Brillouin zone corners, which reverses between layers. (d) Electronic wavefunctions at the zone corners are localised to individual layers for a given spin, while an even distribution exists at the zone centre. (a), (b) and (d) [42], and (b) [31].

In addition to the spin-valley locking in TMDs, the probe of a spin-polarisation predominantly localised to the uppermost layer in bulk materials is a signature of a spin-layer locking in these systems [42, 44, 104, 45]. As depicted in details in Fig.

1.12, the fact that the two layers being rotated by 180° in the 2*H* structure which restores the inversion symmetry, results in an opposite net dipole and thus opposite spin texture of the two individual monolayers. Riley *et al.* [42] showed that by tuning the photon energy, the measured spin polarisation in WSe_2 can be reduced to almost zero, resulting from photoelectron interlayer interference effects, where the probe becoming sensitive to a coherent superposition of the top two monolayers equally, thus assigning the out-of-plane spin-polarisation as a direct result of the locking of electronic spin to the layer-pseudospin. Also, selecting this hidden spin-polarised electronic states in these centrosymmetric 2H-TMDs using circulary polarised light has shown exciting results [104, 45], supporting the spin-valley and layer-pseudospins locking allowed by the local inversion symmetry breaking in these systems.

Valley-dependent spin polarization in the non-centrosymmetric 3R-TMDs

As illustrated in Fig. 1.13(a), each layer is translated by (0, 0, a/3) with respect to the layer below in the 3R phase, resulting in a conventional unit cell which contains three formula units. The primitive unit cell, however, contains only one formula unit, as indicated by the dashed lines. In this stacking structure, the inversion symmetry is broken (space group R3m), and the slanting of the primitive unit cell away from the *z* axis in this phase results in a more complex Brillouin zone (Fig. 1.13(b)), rather than the conventional hexagonal one for the 2H and 1T phases.

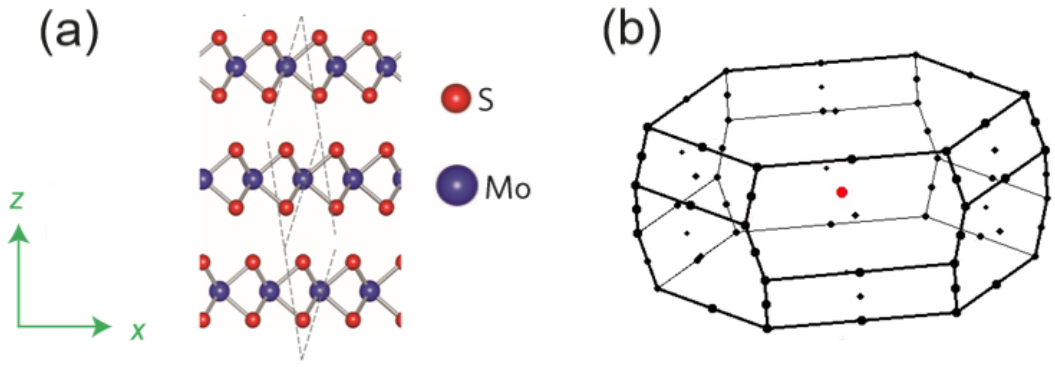

FIGURE 1.13: Crystal structure of 3R-MoS_2 (a) and corresponding Brillouin zone (b), with blue and red spheres indicate Mo and S atoms, respectively, and dashed lines correspond to the primitive unit cell [105].

The main difference between 2H, 1T and 3R-TMDs polytypes is that the crystalline structure of the latter globally breaks inversion symmetry, unlike the earlier two phase where the inversion symmetry exists within the unit cell. This ISB, in addition to the SOC, results in a robust valley polarization in bulk 3R-TMDs, making them a firm basis for the development of magnetic and electric manipulation of spin/valley degrees of freedom [105].

As expected, the electronic structure of 3R-TMDs reveals spin-splittings around the K valleys of the Brillouin zone, emerging from both the ISB and SOC of the material (Fig. 1.14(a)). In addition, due to the net in-plane dipole, located at the transition metal of the system, shown above in Fig. 1.12(a), the measured spin-polarisation is

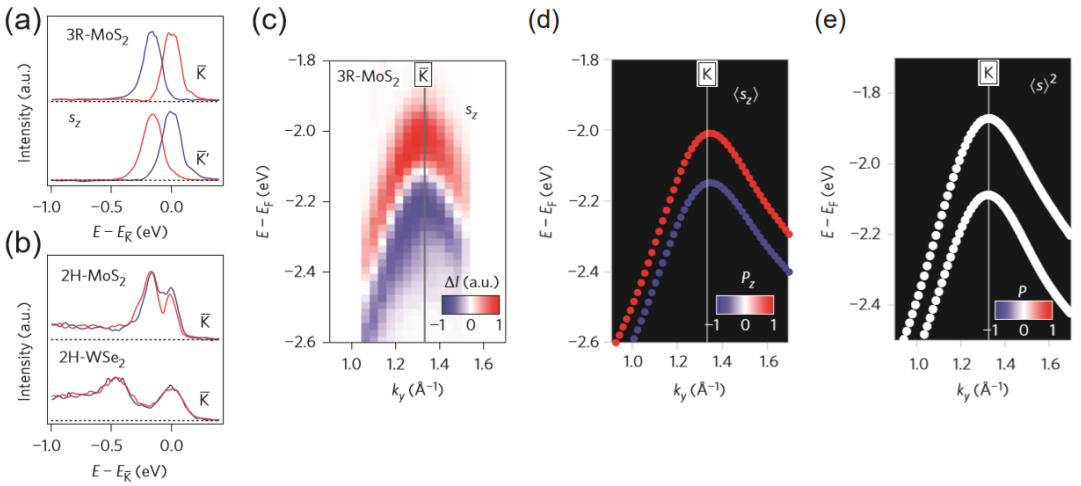

FIGURE 1.14: **Spin-polarised electronic bulk bands at the K valleys**. (a) Constant energy map. Red and blue contours around the K points indicate spin-up and spin-down components, respectively. Spin-resolved energy distribution curves (EDCs) (b) at the K point and the corresponding spin polarization (c). (d) Spin-resolved EDCs for the out-of-plane component of sin S_z at the K and K′ points. (e) Spin-resolved EDCs at the K point from the centrosymmetric materials 2H-MoS_2 and 2H-WSe_2. (f) Spin-ARPES data at the K valley of 3R-MoS_2 along k_y. Calculated total spin polarizations P_z of the valence bands along (0, k_y, 0) for 3R-MoS_2 (g) and the centrosymmetric 2H-MoS_2 [105].

predominantly arising from the out-of-plane S_z component ($P_z \approx \pm 1$), with negligible contribution from the in-plane spin components S_x and S_y ($P_x \approx P_y \approx 0$), as shown in Fig. 1.14(b, c).

In bulk centrosymmetric 2H-TMDs, all the electronic states are spin-degenerate (Fig. 1.14(e)), since the measured spin-polarisation around the K valleys arise from the ISB within the monolayer solely (1H) [42]. In contrast, the lack of inversion symmetry in the 3R stacking yield spin-valley coupled electronic states realized in the bulk material itself (Fig. 1.14(d)). This establishes 3R-TMDs as a very solid playground for spintronics and valleytronics physics, as the spin-polarisation they provide is robust against interference of spin-up and spin-down photoelectrons emitted from different layers of the material, as it is the case for 2H-TMDs, where the relative 180° rotation of the two layers forming the unit cell gives rise to opposite spin polarisations, which can lead to the suppression of the total polarisation at high photon energies, where the photoelectrons would be probed from both layers of the unit cell and not only the topmost one (Fig. 1.12(d)) [42].

Yet the origin of the band splitting is not exactly the same for the two polytypes. While it is emerging from the ISB and SOC only in the 3R phase, interlayer interaction is present in the 2H-TMDs, arising from interactions between the two layers forming the unit cell. This additional interlayer hopping term, in addition to SOC explains the relatively larger band splitting at the top of the valence band at the K point of the Brillouin zone for the 2H compared to the 3R phase. For instance, the valence band splittings at the K (K′) point in 2H-MoS_2 and 3R-MoS_2 are $\sim$ 0.17 eV and $\sim$ 0.14 eV, respectively (Fig. 1.14(g, h)) [105].

1.4.4 Topological features in 1T-TMDs

Unlike 2H-TMDs, where the unit cell contains two monolayers rotated by 180° within each other, which creates an inversion symmetry center, the unit cell of 1T-TMDs consists, as indicated by the number 1, of only one monolayer. This number, as explained above, denotes how many layers are required to form one repeating block along the c-axis, or in other words, the number of layers for atoms to map back onto each other (Fig. 1.9). Thus, as depicted in Fig. 1.15(a), the crystal structure of the 1T transition-metal dichalcogenides consists of the transition metal (D_{3d} coordination) at the centre of a trigonally distorted octahedron of chalcogen atoms, each forming triangular layers above and below the transition-metal plane, rotated by 180° with respect to each other, such that every chalcogen atom from the top sub-layer maps onto another in the bottom sub-layer by the translation $-r \rightarrow r$. Therefore, 1T-TMDs monolayers are centrosymmetric materials with the transition metal being the inversion symmetry center of the unit cell ($r = 0$).

By possessing both global and local inversion symmetry, 1T-TMDs are therefore overlooked for spin-polarisation in non-magnetic materials. The absence of specific atomic asymmetries in 1T-TMDs (D_{3d} point group symmetry) means all bands must be doubly degenerate, and hence a lack of spin polarisation [41]. Therefore, properties such as spin-valley locking are restricted to TMDs with the 2H crystal structure (D_{3h} point group symmetry), since they arise from the local inversion symmetry breaking within each monolayer in 2H-TMDs.

While the overall structure and properties in TMDs are dictated predominantly by the transition metal, the choice of chalcogen leads to a decrease of the band gap when going from S, Se to Te, as a result of the increased degree of overlap of the chalcogen p-orbitals in the larger atoms. However, this is not the only role of the p-orbitals. Bahramy *et al*. [13] have shown a general mechanism for topological phenomena arising solely from a single chalcogen p-orbital manifold, unlike in the "conventional" topological insulator phases such as Bi_2Se_3, where the non-trivial phases arise from inversions between Bi p and Se p orbitals [106].

As described in Fig. 1.15, the unit cell of 1T-TMDs is a two-site chalcogen system (X_1 and X_2), with 3p orbitals for each site. Therefore, a total of 6 orbitals are split into two triply-degenerate $\{p_x,\ p_y,\ p_z\}$ manifolds due to bonding (lower branch) and anti-bonding (upper branch). The trigonal crystal field further splits each of these manifolds into doubly-degenerate in-plane orbitals $\{p_x,\ p_y\}$ and an out-of-plane p_z orbital. The inclusion of spin-orbit coupling lifts the degeneracy of the $\{p_x,\ p_y\}$ orbitals and causes a slight alteration to the energy of the p_z orbital derived state, producing thus the bands $R^{\pm}_{5,6}$, $R^{\pm}_{4'}$ and $R^{\pm}_{4}$, respectively. $\pm$ indicates the parity of each level [13, 107, 108, 109].

The basic details of the dispersion of these bands in the electronic band structure can be understood from the relative hopping strengths in the unit cell, as they are the only responsible of how each band evolves 1.15(a). Intra-layer hopping $t_{1,2}$, which designs the hopping between the chalcogen atoms in the same atomic plane along the a and b axes are stronger for the p_x and p_y orbitals than p_z orbitals, due to the extended in-plane nature of $\{p_x, p_y\}$ orbitals, while inter-layer hopping, both within

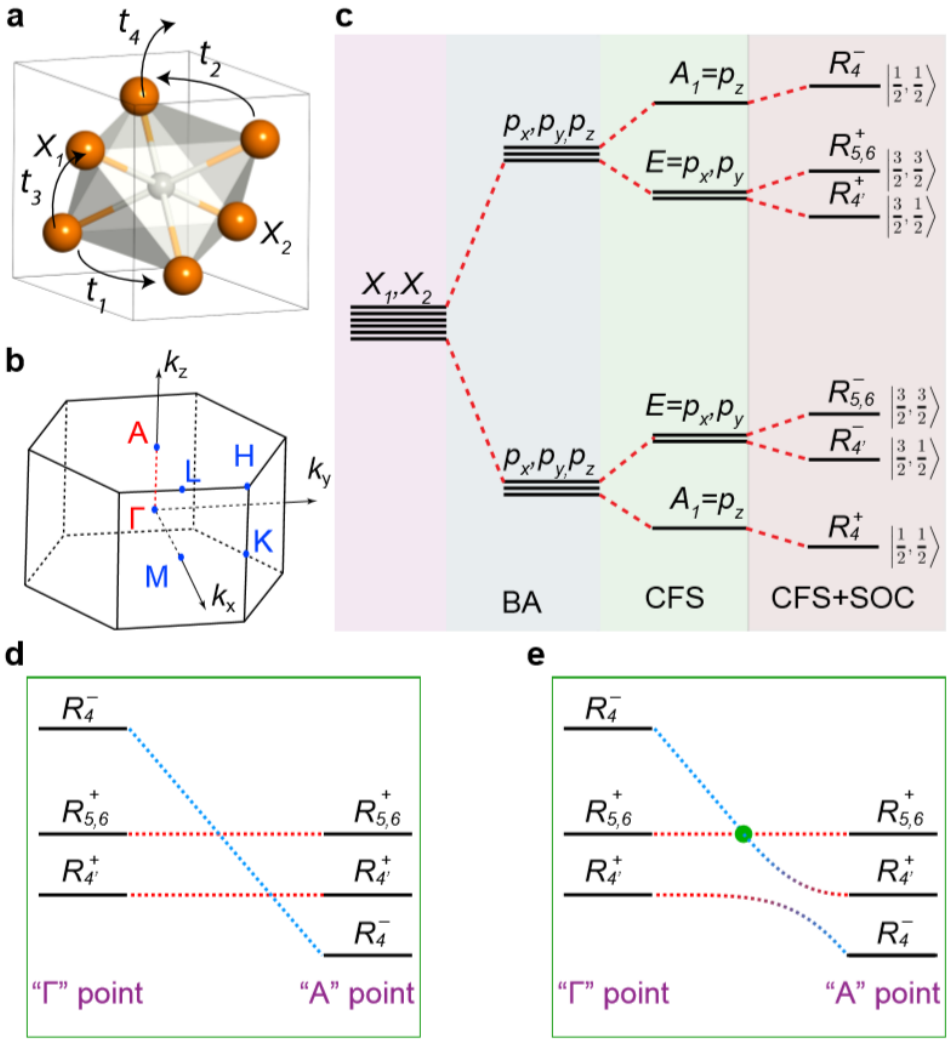

FIGURE 1.15: **Hierarchy of band inversions arising from p orbitals in a trigonal crystal field.** (a). Crystal structure of the 1T transition-metal dichalcogenides, with the transition metal at the centre of a trigonally distorted octahedron of chalcogen atoms (X1 and X2) which each form triangular layers above and below the transition-metal plane. (b). Octahedral unit cell of a 1T-TMD. Hopping paths t_1 to t_4 are indicated. (c). Degeneracy lifting of six-fold degenerate p-orbital levels from two isolated chalcogen atoms (X_1 and X_2). BA: Bringing two chalcogen atoms (X_1 and X_2) together to form the unit cell results in the formation of bonding and anti-bonding manifolds. CFS: Trigonal crystal field, C_{3v} separates $p_{x,y}$ and p_z derived bands. SOC: Spin-orbit coupling lifts the remaining degeneracies (neglecting spin degeneracy). (d,e). Evolution of these crystal-field-derived levels (anti-bonding set) as a function of out-of-plane k_z momentum without (d) and with SOC (e), showing a crossing of the A_1 and E-derived levels that is naturally expected due to their disparate out-of-plane dispersion, forming thus a protected crossing and the opening of an inverted band gap at the crossing of the R_4^- level with the $R_{5,6}^+$ and $R_{4'}^+$ levels, respectively [13].

't_3' and between 't_4' neighbouring unit cells along the c-axis is higher for the p_z

orbitals, due to the extended nature of the p_z orbitals wavefunction along the out-of-plane axis. Consequently, this leads to a significant dispersion of p_z orbitals-derived states and dispersionless $\{p_x, p_y\}$ orbital-derived states along the out of plane momentum k_z. Therefore, a set of k_z-dependent band crossings are naturally expected, arising solely within the p-orbital manifold derived states [13].

Focusing now on the out-of-plane dispersion of the anti-bonding manifold (upper branch) along ΓA direction 1.15(e), the crossing of the p_z orbital derived states R_4^- with the upper band of the $\{p_x, p_y\}$-derived state $R_{5,6}^+$ results in a bulk Dirac point (BDP), due to their belonging to different irreducible representations, protecting thus the crossing. The R_4^- and the lower $R_{4'}^+$ bands share the same symmetry character and angular momentum m_j but have opposite parity $\pm$, their hybridization thus leads to an inverted bandgap which is expected to host topological surface states [13, 107, 108, 109]. An equivalent scenario occurs in the bonding manifold (lower branch), with the crystal-field splitting dictates that the $\{p_x, p_y\}$ and p_z orbitals being reversed. 1T-$PdTe_2$, 1T-$PtSe_2$, 1T-$IrTe_2$ and 1T-$NiTe_2$ have all been demonstrated to host type-I and type-II bulk Dirac fermions as well as ladders of topological surface states and surface resonances [13, 109]. Such topological features are present in 2H-TMDs too, as they belong, similarly with their 1T counterparts, to C_{3v} space group (e.g. 2H-WSe_2, 2H-$NaSe_2$ and 2H-$TaSe_2$) [13].

To fully understand when the crossings are protected and when they are not, a closer look at the hybridisation matrix elements for the crossings of the chalcogen p-derived bands along the k_z direction should be taken. By applying the unitary operator of the C_{3v} rotational symmetry on the wavefunctions describing the bands $R_{5,6}$, $R_{4'}$ and R_4, the following equations can be obtained:

$$C_{3v}|R_{5,6}^{\pm}\rangle = e^{\frac{2\pi i}{3}m_j}|R_{5,6}^{\pm}\rangle = -|R_{5,6}^{\pm}\rangle \tag{1.32}$$

$$C_{3v}|R_{4'}^{\pm}\rangle = e^{\frac{2\pi i}{3}m_j}|R_{4'}^{\pm}\rangle = e^{\frac{\pi i}{3}}|R_{4'}^{\pm}\rangle \tag{1.33}$$

$$C_{3v}|R_{4}^{\pm}\rangle = e^{\frac{2\pi i}{3}m_j}|R_{4}^{\pm}\rangle = e^{\frac{\pi i}{3}}|R_{4}^{\pm}\rangle \tag{1.34}$$

Orthogonal wavefunctions will give different eigenvalues under the application of C_{3v}, and the hybridization matrix elements between them must be therefore zero. This can be summarized as follows:

$<\mid>$	$R_4^{\pm}$	$R_{4'}^{\pm}$	$R_{5,6}^{\pm}$
$R_4^{\pm}$	$\neq 0$	$\neq 0$	$= 0$
$R_{4'}^{\pm}$	$\neq 0$	$\neq 0$	$= 0$
$R_{5,6}^{\pm}$	$= 0$	$= 0$	$\neq 0$

TABLE 1.1

This demonstrates how the crossing is allowed between R_4 and $R_{5,6}$, producing a bulk Dirac point (BDP) protected by C_{3v} symmetry, while it leads to an inverted bandgap between R_4 and $R_{4'}$ due to their opposite parity.

1.4.5 Novel electronic states in TMDs

In addition the spin-polarised electronic states even in the presence of global inversion symmetry (2H phase) and the richness in topological features, strong electron-electron and electron-phonon interactions in TMDs are the origin of a wide variety of instabilities, ranging from spin and charge density wave, superconductivity and Mott-insulating phases, which makes TMDs a fertile playground for exploring the interplay between these novel electronic phases [110, 111].

In general, the reduced electronic dimensionality of TMDs or any other layered materials such as Fe-base superconductors, Cu-based superconductors or heavy Fermions is a key ingredient for these novel states to take place, as this makes them more prone to electronic instabilities [112]. TMDs in particular, where charge density wave (CDW) were observed for the first time [113], they appear even more adopting to electronic instabilities in monolayer [114]. For instance, a very significant enhancement of the CDW transition temperature T_c of $NbSe_2$ from 33 K to 145 K when going from bulk to single layer [115, 116].

On the other hand, one of the most remarkable features for superconducting TMDs is that superconductivity coexists or occurs in proximity of a CDW phase [117, 112]. $NbSe_2$ a prototypical metal, is the most eminent representative of this class of materials, as it hosts a CDW phase (T_c = 33 K) which coexists with superconductivity (T_c = 7,1 K) [118, 119, 120, 121]. However, the isostructural and isovalent compound NbS_2 stands out as a striking exception in this family, which although has a superconductivity below T_c = 6.2 K but does not undergo a CDW phase [122, 123, 124, 110, 125, 126]. This raises questions on whether superconductivity and CDW compete or cooperate in these systems [112, 126].

Many investigations have been devoted to disentangling the driving force of the CDW and its relation to superconductivity. While the traditional understanding consists of a Fermi surface nesting as the origin of these novel electronic states, leading to instabilities in the electronic system and inducing a CDW transition in the Peierls-like picture [127], it has been theoretically and experimentally demonstrated that this scenario is inconsistent with the charge-ordering wave vector, q_{CDW} in TMDs, and thus a simple nesting model cannot account for the CDW in these materials [128, 129]. Instead, the main driving force for both the CDW and superconductivity transitions is attributed to the strong k-dependent electron-phonon coupling (EPC) [128, 129, 115, 130, 110, 131, 126].

Chapter 2

Experimental Techniques

Photoemission spectroscopy is a wide class of experimental techniques which can be described as "photon-in, electron-out" experiments. These experiments consist of the excitation of a sample of interest by a source of photons, and measuring the intensity of the emitted photoelectrons. The measured intensity can be a function of the ejected electron's kinetic energy, its emission angle and spin-polarisation, as well as the photon energy and light polarisation. As developed in the following, such measurements are sensitive to the sample's electronic structure [132, 133, 134, 135, 136, 22].

Depending on which of these parameters are resolved in the measurements, different types of photoemission spectroscopy can be defined. In X-ray photoemission spectroscopy (XPS), for example, the integrated intensity is measured as a function of the emitted photoelectron kinetic energy only. However, angle-resolved photoemission spectroscopy (ARPES) allows the measurements of the intensity as a function of the kinetic energy of the photoelectron and its emission angle, while spin- and angle-resolved photoemission spectroscopy (spin-ARPES) and time and angle-resolved photoemission spectroscopy (TR-ARPES) additionally measures the intensiy as a function of the photoelectron spin polarisation and time delay, respectively [132, 133, 134, 135, 136, 22].

In this chapter, an overview of the experimental techniques used in this work will be provided, with a closer focus on ARPES, the main employed technique throughout this thesis. The key theory behind this technique, allowing the interpretation of photoemission data will be highlighted, and the typical set-ups used for photoemission experiments will be introduced. The theoretical component draws mainly from [136] and [22].

2.1 Angle-resolved photoemission spectroscopy

2.1.1 Principle of ARPES

ARPES is a tool which permits the direct imaging of a solid's electronic band structure. Its origin lies in the photoelectric effect, discovered by Hertz in 1887 [137] and described later by Einstein in 1905 [138], one of the ground-breaking works for which he was awarded the Nobel prize in 1921. This technique can be defined as follow: when a photon is incident on a material, an electron can absorb its energy and, if this energy is large enough to overcome the electron's binding energy E_B and the material's work function ϕ, (on the order of 4.5 eV, presents the minimum energy required for an electron within to overcome the energy barrier at the crystal surface

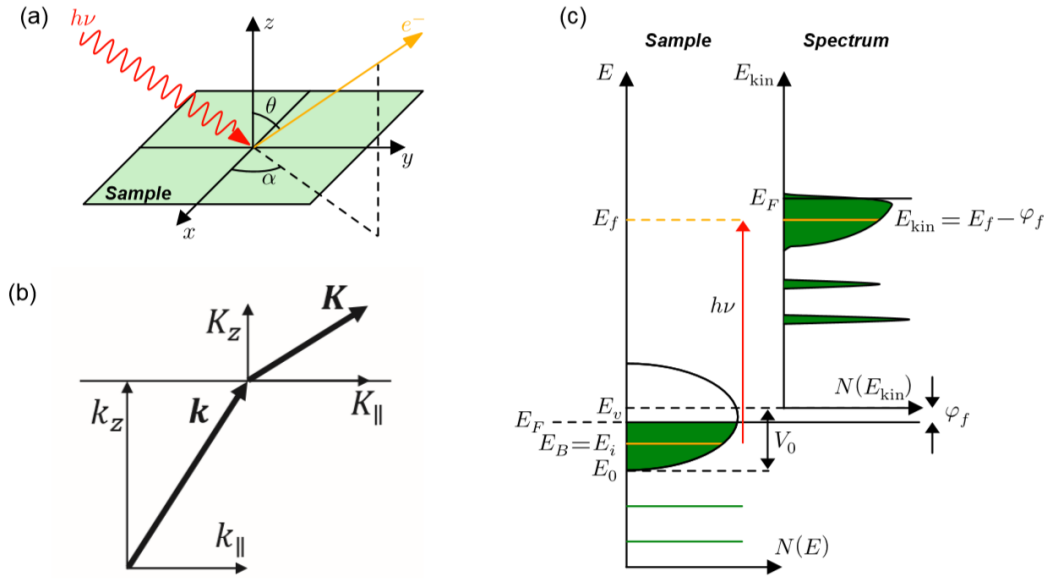

FIGURE 2.1: **Energetics of photoemission**. (a) Schematic geometry of an ARPES experiment, where an incident photon with energy $h\nu$ on a sample surface (x-y) plane causes the emission of a photoelectron at a polar angle θ and an azimuthal angle α, with respect to the z and x direction, respectively. (b) Photoelectron momentum inside $\mathbf{k}$ and outside $\mathbf{K}$ the solid. (c) The density of states in an ARPES spectrum (right) upon the excitation of the initial states within the sample (left) by a photon with sufficienty high energy $h\nu$ [14].

into the vacuum), the electron can escape from the surface of the material into the vacuum and then be detected.

Satisfying both energy and momentum conservation laws between the impinging photon and the N-particle system, the following equations can be obtained:

$$E_f^N - E_i^N = h\nu \tag{2.1}$$

$$\mathbf{k}_f - \mathbf{k}_i = \mathbf{k}_{h\nu} \tag{2.2}$$

where E_i^N and E_f^N are the initial and final state energy of the N-particle system, respectively. $h\nu$ is the photon energy. k_i, k_f and $k_{h\nu}$ are the momentum of the electron in the initial sate, final state within the solid and the absorbed photon, respectively.

However, the momentum of the photon can be neglected at the low photon energies most often used in ARPES experiments ($h\nu < 100$ eV), as it is much smaller than the typical Brillouin-zone dimension $2\pi/a$ of a solid [136]. Therefore, eq. 2.2 can be written as:

$$k_f = k_i + n\mathbf{G} \tag{2.3}$$

with $n\mathbf{G}$ are multiples of the reciprocal lattice vector $\mathbf{G}$, mapping equivalent points in k-space across Brillouin zones [136]. In other words, the required momentum for the electron to reach the excited state is provided by the crystal potential, so that this momentum comes in multiples of the reciprocals vectors $\mathbf{G}$. Therefore, the optical

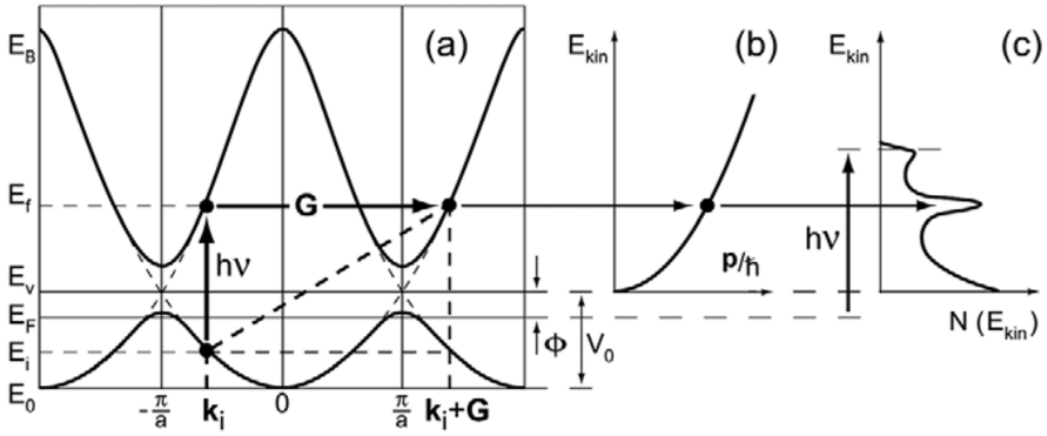

FIGURE 2.2: **Kinematics of photoemission**. (a) Direct optical transition in the solid, with the required momentum provided by the lattice. (b) Free-electron final state in vaccum. (c) Photoelectron spectrum, with the scattered electrons giving rise to a background [136].

transition between the bulk initial and final state can be described by a vertical transition in the *reduced-zone scheme* ($k_f - k_i = 0$) or a transition in the *extended-zone scheme* ($k_f - k_i = \mathbf{G}$), as shown in Fig. 2.2. It is the latter *scheme* which should be considered in the photoemission process, since in ARPES measurements neighbouring Brillouin zones to the first one can be probed by increasing the emission angles.
.

2.1.2 The three-step model

A more accurate framework for describing ARPES is the one-step model, where the photoexcitation and emission of an electron are treated as a single quantum mechanical coherent process, in which the photoelectron is excited directly into a damped inverse LEED (low-energy electron diffraction) state near the surface [139, 140]. This final state is an excited state of the system that matches the boundary condition of becoming a free-particle wavefunction outside the crystal. The one-step model is considered as a cornerstone in cutting edge photoemission calculations. However, a simpler description of ARPES is embodied in the so called "three-step model", which provides reasonable results when invoked in the interpretation of photoemission experiments. Unlike the one-step model, the photoemission process is divided into three independent steps in the three-step model:

1. Optical excitation of an electron from an initial into a final bulk state.

2. Propagation within the bulk to the surface.

3. Transmission through the surface potential barrier and escape into the vacuum.

In the first step of the photoemission process within this model, the transition probability w_{fi} for an optical excitation from an initial state Ψ_i^N into a final state wavefunction Ψ_f^N can be described by Fermi's golden rule [136]:

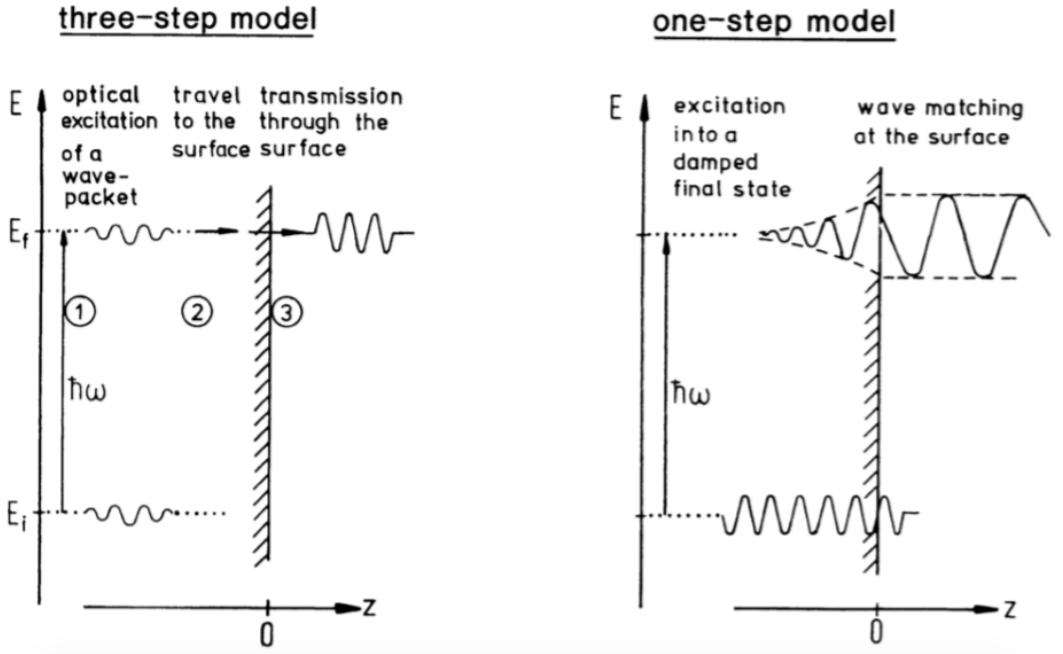

FIGURE 2.3: **Three-step and one-step model**. The three-step model embodies (1) optical excitation, (2) travel to the surface and (3) escape to the vaccum. Wheras the one-step model consists of the direct excitation from an initial state into a damped final state, matching a plane wave in vacuum [22].

$$w_{fi} = \frac{2\pi}{\hbar}|\langle\Psi_f^N|\mathbf{H}_{int}|\Psi_i^N\rangle|^2\delta(E_f^N - E_i^N - h\nu) \tag{2.4}$$

Here, the delta function enforces energy conservation upon excitation with a photon of energy $h\nu$. The N-particle initial state system consists of a N-1-particle system which does not undergo excitation and an electron with binding energy E_B ($E_i^N = E_i^{N-1} - E_B$), which is excited to a final state energy E_f. After overcoming the workfunction Φ, this photoelectron is emitted into the vaccum with a kinetic energy E_{kin}, with a $N-1$ electron system left behind with energy E_f^{N-1} ($E_f^N = E_f^{N-1} + E_{kin}$). The interaction with the photon is given by the interaction Hamiltonian $\mathbf{H}_{int}$, which is treated as a perturbation of the following form:

$$\mathbf{H}_{int} = \frac{e}{2mc}(\mathbf{A}.\mathbf{p} + \mathbf{p}.\mathbf{A}) = \frac{e}{mc}\mathbf{A}.\mathbf{p}, \tag{2.5}$$

where $\mathbf{p}$ is the electron momentum and $\mathbf{A}$ is the electromagnetic vector potential of the electromagnetic field from the photon. The commutation relation $[\,\mathbf{p}, \mathbf{A}] = -i\hbar\nabla.\mathbf{A}$ and the dipole approximation $\nabla.\mathbf{A} = 0$ are invoked (i.e the wavelength of the photon is much larger than the characteristic inter-atomic distances, so $\mathbf{A}$ is assumed to be constant).

The initial state and final state wavefunctions of the N electron system can be divided into the product of the photoelectron wavefunction ϕ_i^k and ϕ_f^k with a momentum $\mathbf{k}$, and the N-1 electron wavefunction Ψ_i^{N-1} and Ψ_f^{N-1}, respectively. Ψ_f^{N-1} is taken to be an eigenfunction of the excited state, Ψ_m^{N-1} with energy E_m^{N-1}. The N-electron system can be written as:

$$\Psi_i^N = P\phi_i^k \Psi_i^{N-1} \tag{2.6}$$

and similarly:

$$\Psi_f^N = P\phi_f^k \Psi_m^{N-1} \tag{2.7}$$

where P is an antisymmetric operator that antisymmetrises the N-electron wavefunction such that the Pauli exclusion principle is satisfied [136]. However, this factorisation is only valid alongside the assumption that the photoelectron's ejection is fast enough so that it does not interact with the remaining N-1 system. This is known as the "*sudden approximation*". This approximation is only applied in the first step within the *three-step* model, while a loss function should be taken into account in the second and third step due to possible scatterings. A scenario which does not fit well with the *one-step* model, since the keystone of this model is to consider the full quantum mechanical process, and thus it is somehow not fully precise to assume no interaction of the ejected electron and the system left behind.

The integral from Fermi's Golden Rule (Eq. 2.4) can then be reformulated as follows:

$$\langle \Psi_f^N | \mathbf{H}_{int} | \Psi_i^N \rangle = \langle \phi_f^k | \mathbf{H}_{int} | \phi_i^k \rangle \langle \Psi_m^{N-1} | \Psi_i^{N-1} \rangle \tag{2.8}$$

where $\langle \phi_f^k | \mathbf{H}_{int} | \phi_i^k \rangle \equiv M_{f,i}^k$ is the one electron dipole matrix element, which will be expanded upon bellow, while $\langle \Psi_m^{N-1} | \Psi_i^{N-1} \rangle = c_{m,i}$ is the probability that the removal of an electron from the initial state leaves the N-1 system in the excited state m. The total photoemission intensity at a momentum k and energy E_{kin} can be written over the sum of all m as follows:

$$I(\mathbf{k}, E_{kin}) = \sum_{f,i} w_{f,i} = \sum_{f,i} |M_{f,i}^k|^2 \sum_m |c_{m,i}|^2 \delta(E_{kin} + E_m^{N-1} - E_i^N - h\nu) \tag{2.9}$$

The term $A(\mathbf{k}, E_{kin}) = \sum_m |c_{m,i}|^2 \delta(E_{kin} + E_m^{N-1} - E_i^N - h\nu)$ is called the *spectral function*, which contains the information about the many-body interaction in the photoemission process. A detailed description about the spectral function will be provided in the following section. Since the photoemission intensity observed in ARPES is restricted to the occupied states only, the Fermi-Dirac distribution $f_{FD}(\omega)$ is introduced, and the total photoemission intensity is given by the expression:

$$I(\mathbf{k}, \omega) \propto \sum_{f,i} |M_{f,i}^k|^2 f_{FD}(\omega) A(\mathbf{k}, \omega), \tag{2.10}$$

while f_{FD} is given by:

$$f_{FD}(\omega) = \frac{1}{\exp \frac{\omega}{k_B T} + 1}, \tag{2.11}$$

where ω is the electron energy, k_B is the Boltzmann constant and T is the system temperature.

In the second step of this model, consisting of the propagation of the excited photoelectron to the surface of the crystal, the finite mean free path of an electron in a solid, λ, must be considered. Since the electron energy can be decreased due to inelastic scattering processes, a background can be observed in the spectrum. Therefore, while escaping from the solid into the vaccum, the photoelectron intensity is

reduced exponentially, which is well described by Beer-Lambert law for photoemission [141]:

$$I_d = I_0 \exp -\frac{d}{\lambda}, \tag{2.12}$$

where I_d and I_0 are the photoelectrons intensity escaping from a depth d and the sample surface, respectively. λ is the IMFP, which can be explained as the length an electron can travel in a material without being inelastically scattered. λ does not depend on the material, but rather on the kinetic energy of the electron, as shown in the "*universal curve*" in Fig. 2.4.

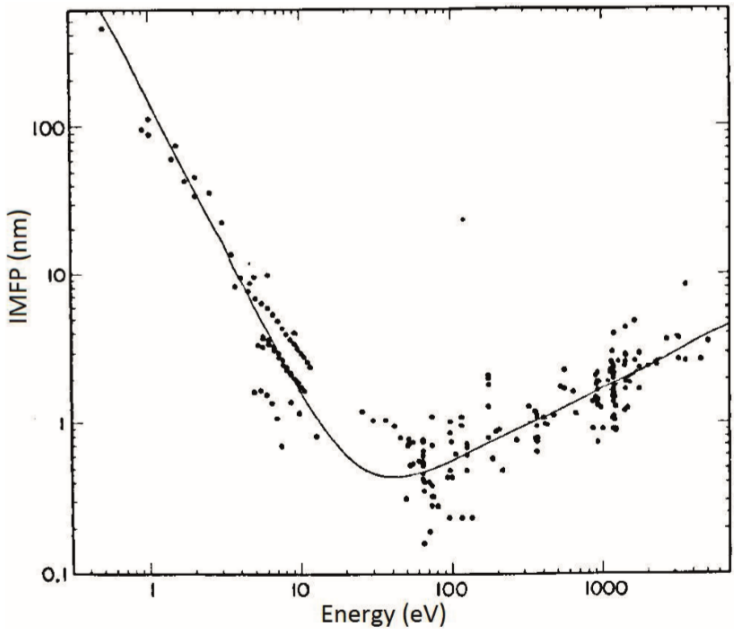

FIGURE 2.4: **Universal curve**. The inelastic mean free path (IMFP) of electrons in various materials as a function of the kinetic energy [141].

In ARPES, the typical incident photon energies range from 5 to 120 eV, where the photoemission cross section in reasonably high, the inelastic mean free path is in the order of only a few Ångstroms (5 to 30 Å). This results in the surface sensitivity of this technique. From the universal curve, it is clear that tuning the photon energy can enhance or reduce the surface to bulk contribution in the obtained spectra.

In X-ray photoemission spectroscopy (XPS) for example, where the photon energies range from 0.1 to 2 keV, the inelastic mean free path is longer, and thus there is a greater probability of photoelectrons to reach the surface, and so the sampling depth is greater, providing information on the chemical composition and atomic environments of the material of interest.

In the third step, where the photoelectron is refracted at the surface and transmitted into the vaccum, the final state wavefunction (Bloch eigenstates inside the solid) must match a free-electron plane wave in vaccum. As mentioned above, by measuring the properties of the emitted/detected photoelectrons in vacuum, which are described by their kinetic energies (E_{kin}) and momenta ($\mathbf{K} = p/\hbar$), the material's

electronic band structure can be directly accessed by relating E_{kin} to E_B and the momentum of the electron in vacuum **K** to its momentum inside the crystal **k**.

The energy conservation law can be written as follows:

$$E_{kin} = h\nu - \phi - E_B, \tag{2.13}$$

while the momentum of the electron in the vacuum **K** can be decomposed into:

$$K_x = \frac{1}{\hbar}\sqrt{2mE_{kin}}\sin\theta\cos\alpha \tag{2.14}$$

$$K_y = \frac{1}{\hbar}\sqrt{2mE_{kin}}\sin\theta\sin\alpha \tag{2.15}$$

$$K_z = \frac{1}{\hbar}\sqrt{2mE_{kin}}\cos\theta \tag{2.16}$$

with m is the electron mass, θ is the polar angle and α the azimuthal angle, with the sample surface in the x-y plane, as highlighted schematically in Fig. 2.1(a). Given the fact that the translational symmetry of the emitted electrons is conserved along the sample surface (in-plane direction: xy), the in-plane (parallel) component of the photoelectron momentum is conserved inside and outside the solid:

$$K_{||} = \sqrt{K_x^2 + K_y^2} = k_{||} = \sqrt{k_x^2 + k_y^2} = \frac{1}{\hbar}\sqrt{2mE_{kin}}\sin\theta \tag{2.17}$$

where $k_{||}$ is defined in the extended zone scheme. However, the translational symmetry perpendicular to the material surface (out-of-plane direction: z) is broken (due to the presence of the surface), therefore, the perpendicular component of the momentum is not conserved inside k_z and outside the solid K_z. To obtain k_z information, we must make an assumption on the dispersion relation of the final state. The natural assumption is a free-electron-like dispersion, which assumes the photoelectron final state to be a neerly-free electron description, giving thus:

$$E_f(k) = \frac{\hbar^2 k^2}{2m} - |E_0| = \frac{\hbar^2(k_{||}^2 + k_z^2)}{2m} - |E_0|, \tag{2.18}$$

where once again the electron momenta k_z is defined in the extended-zone scheme. E_0 corresponds to the bottom of the valence band and $E_f = E_{kin} + \phi$ is the final state energy inside the solid. As depicted in Fig. 2.1(c), both E_f and E_0 are referenced to the Fermi energy E_F, while E_{kin} is referenced to the vacuum level E_v. Taking into account $k_{||}$ obtained in Eq. 2.17, k_z can be approximated as:

$$k_z = \frac{1}{\hbar}\sqrt{2m(E_{kin}\cos^2\theta + V_0)} \tag{2.19}$$

with $V_0 = |E_0| + \phi$ is the *inner potential*. It can be obtained either by fitting the experimentally observed periodicity of the k_z dispersion to the known Brillouin zone size, or by optimizing the agreement between the calculations and the experiments to get the right V_0 [136]. It is clear that by simply detecting the photoelectrons emitted along the surface normal ($k_{||} = 0$), while varying the incident photon energy (and thus E_{kin} of the photoelectrons), k_z can be obtained. Note that the free-electron final state approximation provides more reasonable results at higher kinetic energies of the photoelectron, where the crystal potential is only a small perturbation, and thus the final state bands become so closely spaced in energy to form a continuum, and

the details of the final states become unimportant [136]. In fact, higher photon energies allow transitions into higher energy final states, so that any electrons occupying them are assumed to be "free". However, the interpretation of photon-energy dependent ARPES experiments (k_z dispersion) may not be straightforward due to the k_z uncertainties, which will be discussed further below.

2.1.3 One particle spectral function

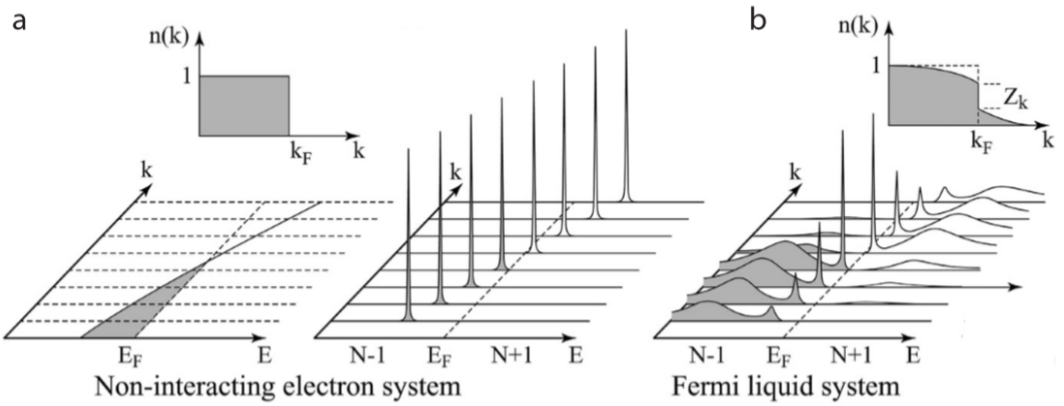

FIGURE 2.5: Schematics of a non-interacting and interacting system, with a single energy band crossing Fermi level E_F, accompanied with the corresponding ground state distribution function $n(\mathbf{k})$ at $T = 0K$. The grey colour highlights the occupied states [136].

As introduced in Eq. 2.9, the spectral function $A(\mathbf{k},\omega) = \sum_m |c_{m,i}|^2 \delta(\omega - E_m^{N-1} + E_i^N)$ contains all the information of the many-body effects in the photoemission process. In the non-interacting case, where the N electrons of the system are independent, Ψ_i^{N-1} is in fact an eigenvalue of the N-1 excited state, therefore, $c_{m,i} = 1$ for one value of m ($\Psi_i^{N-1} = \Psi_m^{N-1}$) and 0 for all others. Since $M_{f,i}^k \neq 0$, the ARPES spectra is a series of delta functions at $E_B^k = -\epsilon_\mathbf{k}$ (the Hartree-Fock energies: $\epsilon_\mathbf{k} = \frac{\hbar^2 k^2}{2m}$), as shown in Fig. 2.5(a). However, in the case of many-body interactions, many $c_{m,i}$ will have non-zero contributions, since the removal of the photoelectron results in a strong change of the system effective potential and thus, Ψ_i^{N-1} will have an overlap with several eigenstates Ψ_m^{N-1}. Consequently, the ARPES spectra consist of a main line and a spread of many satellite peaks for these additional final states (Fig. 2.5(b)) [136]. In other words, when no interactions are present, the final N-1 particle system is similar to what it was before the photoemission process occurs, and the photohole lifetime is infinite. On the other hand, the stronger the interaction in the system, the higher the probability to annihilate the photohole, and hence the higher excited states.

It is convenient to apply a Green's function approach $G(\mathbf{k},\omega)$ in order to obtain the spectral function, since the one-electron propagation in the many-body system can be described by the time-ordered Green's function, $G(t - t')$ (the probability that an electron added to a lattice at position $\mathbf{r}$ and time t will still be in the initial state after a time $t - t'$). $A(\mathbf{k},\omega)$ can be defined as the imaginary part of the Fourier transformed Green's function:

$$A(\mathbf{k},\omega) = -\frac{1}{\pi} ImG(\mathbf{k},\omega) \tag{2.20}$$

For a non-interacting system, the Green's function is written as:

$$G(\mathbf{k},\omega) = \frac{1}{\omega - \epsilon_{\mathbf{k}} - i\eta} \tag{2.21}$$

where $\eta \to 0$. The spectral function in Eq. 2.20 is given by:

$$A(\mathbf{k},\omega) = -\frac{1}{\pi}\delta(\omega - \epsilon_{\mathbf{k}}) \tag{2.22}$$

Therefore, the resulting ARPES spectra correspond to a delta function at an energy defined by the Hartree-Fock orbital energy as depicted in the left side of Fig. 2.5(a).

For a strongly-correlated system, the interactions leading to changes in energy and lifetime are formally included in the Green's function as a complex electron self-energy written as: $\Sigma(\mathbf{k},\omega) = \Sigma'(\mathbf{k},\omega) + i\Sigma''(\mathbf{k},\omega)$, giving thus:

$$G(\mathbf{k},\omega) = \frac{1}{\omega - \epsilon_{\mathbf{k}} - \Sigma(\mathbf{k},\omega)} \tag{2.23}$$

As a result, the spectral function is written as:

$$A(\mathbf{k},\omega) = -\frac{1}{\pi}\frac{\Sigma''(\mathbf{k},\omega)}{[\omega - \epsilon_{\mathbf{k}} - \Sigma'(\mathbf{k},\omega)]^2 + [\Sigma''(\mathbf{k},\omega)]^2} \tag{2.24}$$

In $A(\mathbf{k},\omega)$, the real part, Σ', renormalises the band positions from the bare electron energy, whereas the imaginary part of the self energy, Σ'', increases the linewidths of bands due to the different scattering processes, which in turn contributes to the finite quasiparticle lifetime (τ) due to the many body effects such as electron-impurity, electron-electron and electron-phonon interactions. In conclusion, high resolution ARPES does not only measure the electronic structure of independent particle system (the "bare band" $\epsilon_{\mathbf{k}}$), but also allows direct measurement of many-body effects present in strongly correlated systems [142]. However, the imaginary part of the self energy is not the only reason of the increase in linewidths of the bands, notably in systems with significant k_z dispersion, where the effect of k_z *broadening* can be important and hence should be considered.

2.1.4 Matrix element

As introduced in Eq. 2.8, the one electron dipole matrix element is given by:

$$M^k_{f,i} \propto \langle \phi^k_f | \mathbf{A}.\mathbf{p} | \phi^k_i \rangle \tag{2.25}$$

an important contribution to the photoemission intensity (Eq. 2.10), since it can lead, in certain circumstances, to strong selection rules. In other words, depending the polarization and the energy of the incoming photons, the optical selection rules between the initial and the final states of the single particle wavefunctions as well as the experiment geometry, the matrix elements can cause the suppression of the ARPES intensity [136, 22].

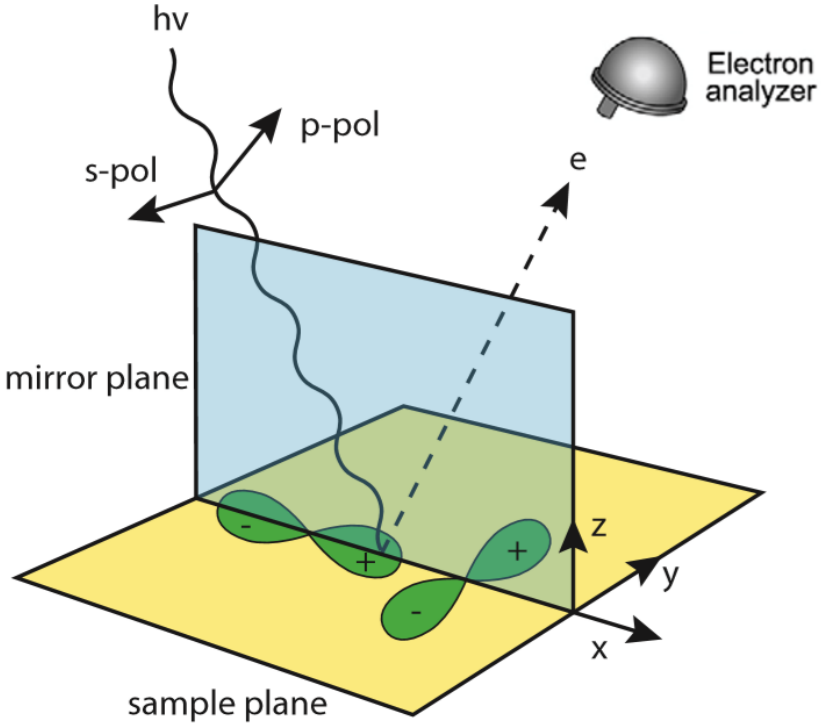

FIGURE 2.6: Idealised geometry of an ARPES experiment, highlighting the matrix elements effects dependencies on the parity of the light polarisation and initial state orbitals with respect to the mirror plane [82].

As shown in Fig. 2.6, by considering photoemission from p-orbitals using linearly polarised light, with the electron analyser located in the mirror plane (the scattering plane formed by the incident light vector and outgoing photoelectron vector), the integrand in the overlap integral (Eq. 2.25) must be an even function under reflection with respect to the mirror plane in order to have a non-vanishing photoemission intensity. Since the final states which have an odd parity will have a node on the mirror plane and so the amplitude of the wavefunction at the detector will be zero. Therefore, the final state wavefunction ϕ_f^k must be even parity [136].

On the other hand, the dipole operator parity, which is governed by the light polarisation vector consists of an even parity (+) for p-polarised light with respect to the mirror plane, since its polarisation vector is perpendicular to the sample surface, and an odd parity (-) for s-polarised light, as a result of its parallel polarisation vector to the sample surface (Fig. 2.6). Hence, the matrix element can be expressed as:

$$M_{f,i}^k \propto \langle \phi_f^k | \mathbf{A}.\mathbf{p} | \phi_i^k \rangle = \begin{cases} \langle + | + | + \rangle \neq 0, & \text{for p-pol} \\ \langle + | - | - \rangle \neq 0, & \text{for s-pol} \end{cases}$$

Thus, p-polarised light will probe even parity (+) initial states orbitals, while s-polarised light will excite odd parity (-) initial states orbitals, with all other combinations intergrating exactly to zero, and so the one-electron transition matrix element is vanished, resulting in a complete suppression of the ARPES intensity.

As depicted in Fig. 2.6, $p_{x,z}$ orbitals have even parity eigenvalues with respect to the mirror plane, therefore, they are excited solely by p-polarised light. On the contrary,

p_y orbitals have an odd parity (opposite phase of the wavefunction on each side of the mirror plane), and so they are probed using s-polarised light. This is, however, an idealised picture to what really happens in an ARPES experiment. Practically, both the propagation vector of the light and the electron analyser can be at an angle to the mirror plane, meaning that the light polarisation vector might not be purely p- or s-polarised, and the final state is not strictly required to be of even parity, respectively. Furthermore, the bonding and hybridization of the orbitals make the symmetry reasoning not fully valid. Accordingly, the photoemission intensity will be predominantly from the symmetry expected from the initial states orbitals, but instead of leading to a complete vanishing matrix element for the other orbitals, these factors result in a rather quantifiable reduction in the one-electron transition matrix element and therefore in the photoemission intensity.

Additionally, by considering both the vector potential $\mathbf{A}$ and the final state wavefunction $\phi_f^{\mathbf{k}}$ to be plane waves, giving thus $\mathbf{A} = A_0\boldsymbol{\epsilon}$ and $\phi_f^{\mathbf{k}} = \exp i(\mathbf{k}.\mathbf{x})$, respectively ($\boldsymbol{\epsilon}$ is a unit vector along the direction of the light polarisation). The matrix element from Eq. 2.25 can be written as:

$$\begin{aligned} M_{f,i}^{k} &\propto \langle \exp i(\mathbf{k}.\mathbf{x}) | A_0\boldsymbol{\epsilon}.\mathbf{p} | \phi_i^k \rangle \\ &\propto (\boldsymbol{\epsilon}.\mathbf{k}) \langle \exp i(\mathbf{k}.\mathbf{x}) | \phi_i^k \rangle \end{aligned} \tag{2.26}$$

In addition to its dependency on the initial state wavefunction and the experiment geometry, as discussed above, this equation illustrates the dependency of the matrix element on the outgoing $\mathbf{k}$-vector, which in turn can be affected by the photon energy. For instance, upon changing the photon energy $h\nu$, both the photoelectron kinetic energy E_{kin} and the magnitude of $\mathbf{k}$ will change. The matrix element $M_{f,i}^{\mathbf{k}}$ changes, however, are not necessarily monotonic upon the photon energy variation [136]. To conclude, it is evident that matrix element effects can lead to a remarkable enhancing/diminishing of the ARPES intensity with respect to their dependencies on photon energy, photon polarisation, experiment geometry as well as the initial states orbital character.

2.1.5 $\mathbf{k}_z$ uncertainties

As briefly discussed above, despite its large validity at higher photon energies, the free-electron final state approximation can be not fully compelling at lower photon energies, due to the uncertainties arising from the out-of-plane k_z dispersion.

Explicitly, the finite mean free path of the photoelectrons results in a damping of the final state in the z direction (perpendicular to the sample surface) into the bulk of the material over a distance λ (Fig. 2.7(a,b)) [143, 140]. Additionally, the broken translational symmetry along the z direction implies a finite broadening to k_z, which can be expressed by: $\Delta k_z = \lambda^{-1}$, evidencing a larger broadening for smaller probing depths (shorter λ). To demonstrate this, the wavefunction of an ejected electron within the material ($z < 0$) can be approximated as [144]:

$$\psi(z) = \frac{1}{\sqrt{\lambda}} \exp\left(ik_{z0}z\right) \exp\left(\frac{z}{2\lambda}\right) \tag{2.27}$$

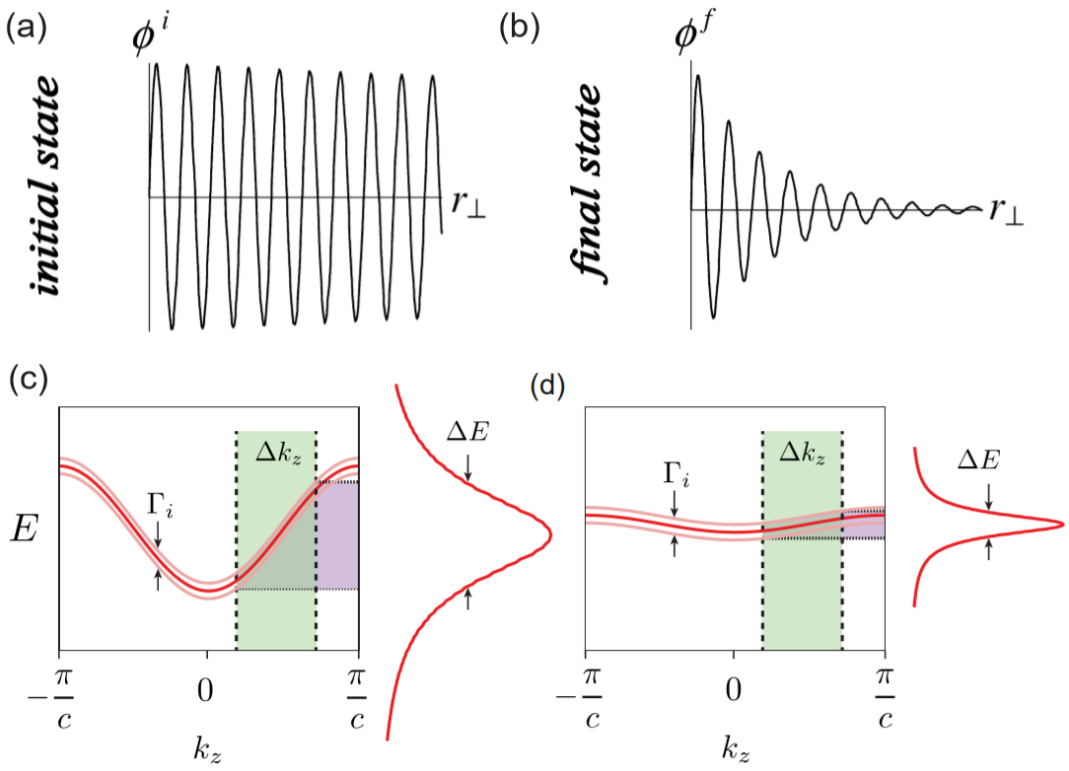

FIGURE 2.7: **k_z broadening**. (a,b) Initial ϕ^i and final ϕ^f state wavefunctions characteristic behavior as a function of the out-of-plane z direction, respectively, highlighting a damping of the final state wavefunction into the solid (b) [143]. (c-d) Effect of the k_z broadening for 2D and 3D states. (c) For a strongly k_z dispersing band, the energy broadening ΔE is predominantly due to the k_z broadening. (d) For a 2D state, however, where the k_z dispersion is not significant, the energy broadening is limited by the lifetime Γ_i [82].

with k_{z0} is the out-of-plane k_z momentum of the photoelectron for a selected photon energy. It is clear that the amplitude of the wavefunction decreases exponentially into the bulk over a scale characerised by λ. The Fourier transform of $\psi(z)$ can be written as:

$$\phi(k_z) = \frac{1}{i(k_z - k_{z0}) - \frac{1}{2\lambda}} \tag{2.28}$$

Consequently, the envelope of k_z integration, given by the squared modulus of the Fourier transform is given by:

$$|\phi(k_z)|^2 \propto L(k_z) = \frac{1}{2\pi\lambda} \frac{1}{(k_z - k_{z0})^2 + (\frac{1}{2\lambda})^2} \tag{2.29}$$

Manifestly, the uncertainty in k_z is well described by a Lorentz function centered at k_{z0} with a full width at half maximum (FWHM) of λ^{-1}. As highlighted in Fig. 2.7(c,d), the k_z broadening however, is only a problem for three-dimensional systems, since for quasi-2D states, which are dispersionless in k_z, the k_z broadening is less significant and thus the bands are much sharper in energy than three-dimensional bands (Fig. 2.7(d)). This implies that the one-particle spectral function linewidths are only limited by Σ'' in 2D systems (i.e. the total energy broadening is predominantly reflecting intrinsic photohole and photoelectron lifetimes). Conversely, in

3D systems, where the electronic states disperse greatly in k_z, a large k_z broadening results in a large energy broadening ΔE (Fig. 2.7(c)). Therefore, rather than a sharply-defined value, the ARPES spectrum probes a distribution in k_z, which can be described by the sum of one-particle spectral functions for all k_z, with a maximum contribution arising from $k_z = k_{z,0}$ and the width of integration set by the Lorentzian function $L(k_z)$, giving thus:

$$A'(\omega, k_x, k_y, k_{z,0}) = \int_{-\infty}^{+\infty} L(k_z) A(\omega, k_x, k_y, k_z) dk_z \tag{2.30}$$

Empirically, for the typical photon energy range used in ARPES (20-120 eV), the corresponding mean free path is about 5Å, resulting in a significant k_z integration, which can reach 25% of the Brillouin zone size [145]. This broadening will be included in the band structure calculations to simulate the ARPES measurements in Chapter 3 and 4.

2.1.6 Core level photoemission spectroscopy

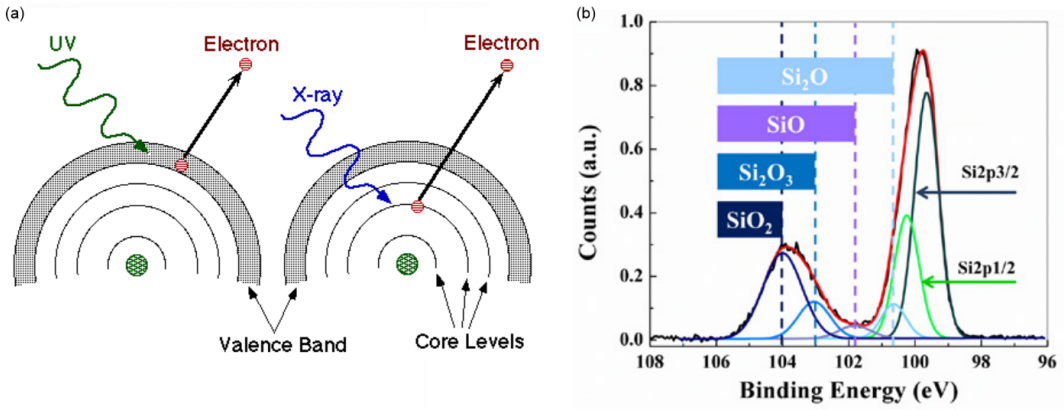

FIGURE 2.8: (a) A sketch showing the difference between ARPES and XPS, where the used photon energies probe electrons from the valence band and core levels, respectively. (b) XPS on core levels reveals a variety of chemical compositions within a silicon sample from surface oxidation [146].

Unlike ARPES, where the photon energy range can go from 20 to 120 eV, X-rays photons, often generated using the atomic spectral **K**-α emission lines of magnesium (1253.7 eV) or aluminium (1486.7 eV) in laboratory setups, are used in core level measurements, referred to as x-ray photoemission spectroscopy (XPS). The merit of this technique is the capability of determining the chemical composition and atomic valence of a material, giving access to identify the oxidation states and changes in the electronic structure due to the interaction with neighbouring atoms such as intercalants, adsorbants and substrate. Furthermore, XPS is a momentum-integrated technique, and hence the provided information is only energy related [147, 148, 149, 150].

As shown in the *universal curve* in Fig. 2.4, the increase in photon energy greatly increases the electron escape depth, allowing the determination of the elemental composition of a sample, including a dopant concentration. However, the cross-section for photoemission generally decreases, unless there is a resonance. More explicitly,

when increasing the concentration of a substitutional dopant, the measured core levels relative intensities of different elements permits the determination of the relative composition, given that the corresponding binding energies of the dopant and host material core levels are well-separated and their photoemission cross-sections are sufficiently large.

In addition to the main peaks observed from the XPS spectral lines, Auger peaks are also present in the spectrum. These Auger peaks arise as a result of the transition of electrons in the atom filling in inner-shell vacancies, causing the emission of other electrons. In other words, following the removal of an electron from a core level leaving a vacancy, an electron from a higher energy level may fall into the vacancy, and thus may lead to a release of energy. This energy can either be released as an emitted photon, or transferred to another electron, resulting in its ejection from the atom. The second ejected electron is called an Auger electron. However, the observed kinetic energies of Auger electrons are independent of the photon energy, making thus Auger peaks easy to identify [149].

2.2 ARPES experiments

So far the principles and theory behind ARPES have been presented, but the practical considerations of performing these measurements have not been discussed yet. In this section, the different light sources used for ARPES experiments will be introduced, with a particular focus on synchrotron radiation. Furthermore, the I05-ARPES endstation, where all the data presented in this thesis was collected will be described. On the other side, while this technique has revolutionised condensed matter physics with its ability to directly measure the electronic structure, this chapter will finish by giving insights on its difficulties and limitations, notably the surface sensitivity and the need for ultra-high vacuum (UHV).

2.2.1 Light sources

To achieve the highest energy and momentum resolution, an ARPES experiment requires a monochromatic light source. In laboratories, the most commonly used light sources are gas discharge lamps and lasers. Gas discharge lamps, typically He, are used as a light source which has characteristic atomic spectral lines (Xe and Ne can be used as well), giving thus a well defined source of light at few discrete photon energies ($h\nu$ (HeI) = 21.2 eV and $h\nu$ (HeII) = 40.8 eV). Due to their high intensity and significantly small light spot size (tens μm vs. few mm for lamp sources), laser-ARPES has become very eminent and significantly improved the data quality, particularly for small non-uniform samples. The photon energy range provided by lasers is generally between 5 and 11 eV, depending on the laser type.

These sources, however, only provide photons at few energies, and hence the electronic band structure along the out-of-plane k_z momentum cannot be probed. This is problematic and limits the full investigation of sample whose band structures have significant out-of-plane dispersion (3D systems). Also, the lack of a wide photon energy range in ARPES makes it challenging to disentangle 3D bulk bands from 2D surface states.

In addition, the low photon energies produced by either gas discharge lamps or lasers only allow to cover a small area of the Brillouin zone (eq. 2.17). Therefore, these light sources are only suitable for crystalline structures with large lattice spacings and hence small Brillouin zones, or for systems where the electronic bands of interest are in the vicinity of the normal emission angle $k_{||} = 0$. To fully map the Brillouin zone under such conditions is very challenging as it requires a significant alteration of the sample orientation, which in turn can be restricted by the manipulator motions.

To overcome these issues, synchrotron radiation, which offers significant advantages compared to gas discharge lamps or lasers can be used. The large photon energy range (18 to 240 eV in the case of the I05 beamline of Diamond Light Source [151]), and the significantly high photon flux compared to a gas discharge lamp, especially in the core operating energy range (18 to 100 eV), allows the probing of the electronic band structure along the out-of-plane k_z momentum, as well as increases the data collection rate, respectively.

Briefly, the basic physics underpinning synchrotron operation consists of the acceleration of electrons by bending magnets within the synchrotron ring forming a stored beam (3 GeV storage ring for Diamond Light Source). This beam is passed through an *undulator*, which produces the radiation used in experiments. The undulator, formed by a periodic array of electromagnets (Fig. 2.9), allows both for the selection of the beam energy by varying the gap size between these parallel magnetic arrays, as well as its polarisation by creating a magnetic field, dictating for the electrons to oscillate and produce a highly collimated synchrotron radiation of a particular light polarisation; i.e. linear horizontal, linear vertical, circular right or circular left. The latter two are effectively a combination of linear and vertical polarised light. Except the part useful for the experiment, and thus allowed to carry on to the beamline axis, the rest of electrons are retained in the synchrotron storage ring.

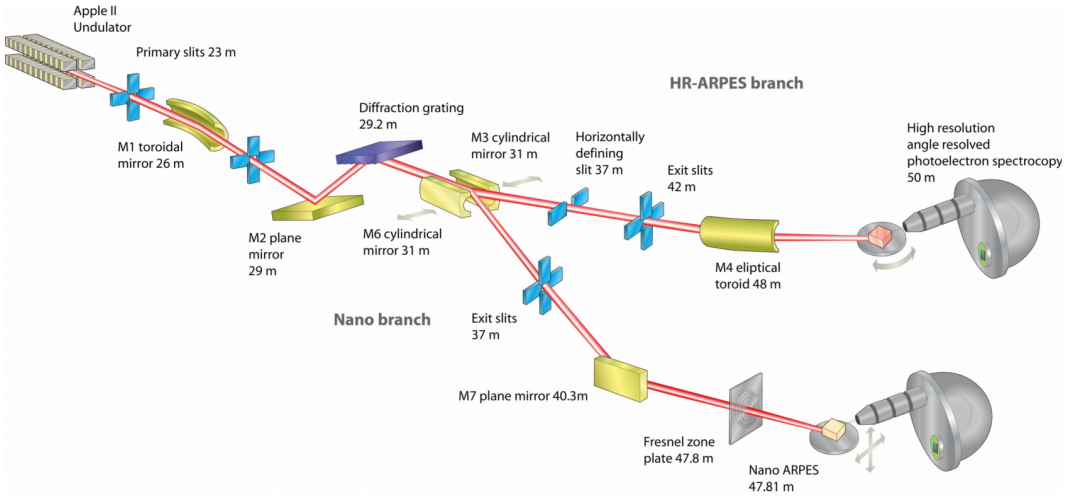

FIGURE 2.9: Schematic layout of the i05 beamline of Diamond Light Source, showing each component with its name and distance from the undulator up to the two branches HR-ARPES and nano-ARPES [151].

Although the highly collimated light produced by the undulator is centered at the

desired photon energy, the bandwidth has still a significant broadening. In order to be practically useful in ARPES measurements, a monochromator, consisting of a diffraction grating is required to diffract the incoming light and discard unwanted wavelengths (collimated plane grating monochromator cPGM at the I05 beamline). Through Bragg's law, the diffraction grating is pitched, diffracting thus the desired peak wavelength down the beamline. The incident light is further improved by refocusing mirrors, as well as variable slits to filter out the outermost part of the beam. At a final stage, the photon beam is focused onto the sample with a spot size of 70×100 μm^2 for the case of the I05 end station.

The photon flux (i.e. intensity) is usually desired to be maximised (up to 2.10^{13} ph/s at the I05 beamline of Diamond Light Source). However, this can sometimes lead to detector saturation and energy resolution broadening due to space charge effects [151], where emitted electrons form a cloud outside the solid which repels and limits the emission of further electrons from the surface. Therefore, the intensity can be reduced for a better defined photon energy and thus a better resolution.

A schematic of the 50 m long beamline of the high-resolution 'HR' branch of the i05 beamline at Diamond Light Source, where all the ARPES results in this work were collected, is depicted in Fig. 2.9 [151]. A more detailed description of synchrotron radiation and some applications can be found in [152], from where the main aspects of this section were derived.

Not used for this work and thus not described in this section, the second branch of the I05 beamline is dedicated for spatially resolved ARPES and its nano-ARPES end station (Fig. 2.9).

2.2.2 I05 HR-ARPES endstation

The main element of every ARPES endstation is the electron analyser, which is made of three key components: the electrostatic lenses, the hemispherical deflector with entrance and exit slits, and the electron detector. After being emitted from the sample surface with an appropriate in-plane emission angle θ, photoelectrons enter the transfer lens section, where they are accelerated or decelerated by the electrostatic lenses to the *pass energy*, E_{pass}, and focused into the entrance slit of the analyser. Photoelectrons follow then curved trajectories around the hemisphere section, with their kinetic energy after the transfer lens section dictating their curvature radius. This means that only electrons within a narrow range in energy, centred at the pass energy, E_{pass} will pass all the way through the hemisphere section and make it to the detector. However, if the kinetic energy region of interest is larger than is available for a given pass energy, then a *swept mode* is required to be set for a full dataset visualisation. The pass energy can be written as follow:

$$E_{pass} = \frac{e\Delta V}{\frac{R_1}{R_2} - \frac{R_2}{R_1}}, \tag{2.31}$$

given the fact that the analyser consists of two concentric hemispheres of radii R_1 and R_2 with a potential difference ΔV applied accross them.

The final step for the photoelectrons, now sorted by their kinetic energy, is their incidence on a 2D electron detector, consisting of multichannel plates (MCP) and a

phosphor screen, with a CCD camera providing a live image of the electronic structure.

The theoretical energy resolution of ARPES is set as [136, 153, 151]:

$$\Delta E = \sqrt{\Delta_{h\nu}^2 + E_{analyser}^2} \tag{2.32}$$

$$\Delta_{h\nu} = \frac{h\nu}{R_m} \tag{2.33}$$

$$E_{analyser} = E_{pass}(\frac{\omega}{R_0} + \frac{\alpha^2}{4}) \tag{2.34}$$

with $R_0 = \frac{R_1+R_2}{2}$, ω is the width of the entrance slit of the analyser, and α is the acceptance angle.

Empirically, the main contributions to the energy resolution in ARPES are from the monochromator, $\Delta_{h\nu}$, and the analyser, $E_{analyser}$, as shown in Eq. 2.32. The latter is predominantly governed by the pass energy, E_{pass} (Eq. 2.34), while the earlier is set by the monochromator resolving power, R_m, which can surpass 20000 at low photon energies in the case of the I05 beamline [151]. Generally, in the core operation energy range (18 to 100 eV), the energy resolution is kept well below 10 meV but slightly increases at higher photon energies due to the larger uncertainty in the kinetic energy. However, the total energy resolution may further be influenced by other effects such as the sample grounding noise and the temperature [151]. For instance, Fermi-Dirac distribution (Eq. 2.11) dictates that every electronic band is measured with an energy broadening of a width of k_BT, with k_B representing Boltzmann constant and T the temperature, as well as any intrinsic temperature dependent interactions such as electron-phonon coupling. Nevertheless, modern ARPES endstations have overcome most of the resolution limitations, allowing the reliable measurement of sub-meV features, such as superconducting gaps [120, 121].

The monochromator resolving power, R_m, does not only contribute to the energy resolution, but affects the momentum resolution as well, yet as a limiting factor. The in-plane momentum $k_{||}$ resolution is given as [153]:

$$\frac{\Delta k_{||}}{k_{||}} = \sqrt{(\Delta\theta cot(\theta))^2 + R_m^{-2}} \tag{2.35}$$

From Eq. 2.35, it is evident that the higher θ, the better the momentum resolution, providing insights to measure outside the first Brillouin zone. Whereas the angular resolution, $\Delta\theta$, is typically set on the order of 0.1° [151].

The HR-ARPES endstation at Diamond Light Source, sketched in Fig. 2.10, is composed from three ultrahigh vacuum (UHV) chambers, an entry load lock and a docking port for a UHV suitcase [151]. These three chambers include an interface chamber IC, consisting of a wheel used for sample storage, an upper chamber UC, where cleaving single-crystal samples, low energy electron diffraction LEED and alkali metal deposition are performed, and a lower chamber LC in which ARPES measurements take place. Except the load lock, the vacuum levels are kept below 2.10^{-10} mbar in all chambers. Additionally, a molecular beam epitaxy (MBE) and a

preparation chamber which contains the majority of in-situ characterisation equipments as well as few-layer and sub-monolayer growth capabilities. These chambers can operate on their own alongside ARPES experiments.

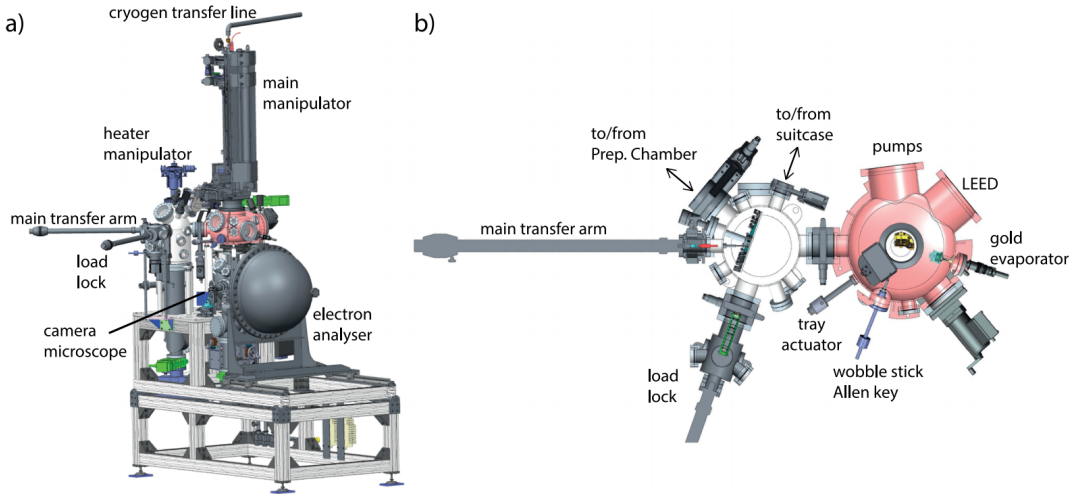

FIGURE 2.10: HR-ARPES end station of the i05 beamline depicting the Lower Chamber (LC, grey), Upper Chamber (UC, red), Interface Chamber (IC, white) and Load Lock (LL, grey again). (b) Cut through the transfer level of the LL, IC, and UC showing the multi-position load-lock recipient (green), the main transfer arm, the sample storage wheel in the IC, wobble stick used for cleaving and the tray for capturing broken off cleavage posts in the UC. Also, additional ports on the IC for transfers in and out of the Preparation Chamber and a vacuum suitcase are shown as well [151].

The hemispherical electron analyser is a Scienta R4000 model with a standard lens operated in the angle-resolving mode with a $\pm 15^{\circ}$ window, and the possibility of selecting either a straight or a curved entrance slit [151]. The manipulator consists of a cryogenic sample goniometer with 6 degrees of freedom (x, y, z, polar angle θ, azimuthal α and tilt ϕ), allowing thus the translation and rotation of the sample over a large range of orientations and giving the ability for reliable sample measurement and accurate repositioning using optical encoders. Cryogenic cooling is provided using liquid helium, permitting temperatures as low as 5K to be easily stabilized. Besides, as well as improving the base pressure, the additional closed-cycle helium cyro-shield further allows the stabilization of lower temperatures, required for superconducting gap measurements for example (3.7K during a FeSe measurement), while sample temperatures up to 350 K can be obtained using a heater near the cold-head of the cryostat [151]. All these assets provide excellent conditions for reliable measurements and sample lifetimes.

A full description of the HR-branch of the I05 beamline can be found in [151].

2.2.3 Sample preparation

Besides the monochromatic light source and the electron analyser, the final element of any ARPES end station is the sample. As discussed, ARPES technique is extremely surface sensitive (the inelastic mean free path IMFP in the solid is on the order of 5 Å

for the photon energy range using within this work), and hence it is indispensably required to have atomically-flat surfaces that are free from any contaminants. For instance, in addition to the intrinsic lifetime broadening, the Fermi function and any interactions that contribute to the broadening of the electronic bands (the k_z uncertainties, as discussed above for example), any surface contamination will result in extra incoherent elastic and inelastic scattering, which decreases the probability of a collision-free journey of the photoelectron from the sample to the detector, and thus penalise the energy and momentum resolution.

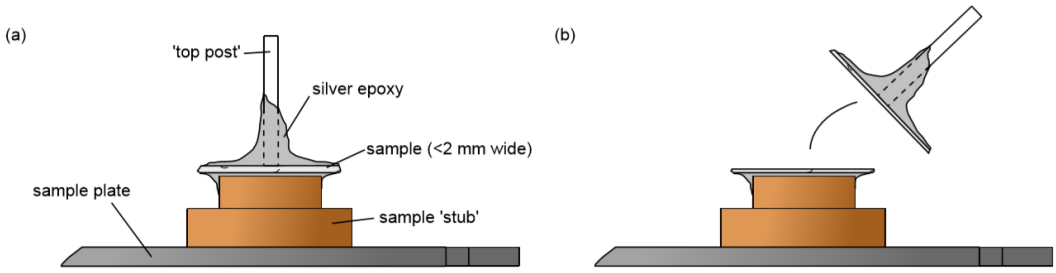

FIGURE 2.11: **Cartoon demonstration of sample cleaving in UHV environment**. (a) Top post firmly bound to the sample surface using cured silver Epoxy. (b) Cleaved crystal at the Van der Waals gap revealing a clean surface [14].

At a vacuum pressure of $p = 10^{-6}$ mbar, the formation of a monolayer-worth of adsorbates takes place within a few seconds only (1ML $\propto 6 \times 10^{14}$ particles.cm^{-2} [22]). De facto, the rate, R, of adsorption of a number of residual gas molecules ΔN onto an area ΔA of the sample surface in an amount of time Δt can be approximated by [22]:

$$R = \frac{\Delta N}{\Delta A \Delta t} \approx 4 \times 10^{22} \frac{p S_c}{\sqrt{MT}} [cm^{-2} s^{-1}], \tag{2.36}$$

with p is th pressure in mbar, M is the molecular mass of the gas and T is the temperature in Kelvin while $0 \leq S_c \leq 1$ is the 'sticking coefficient'. Therefore, the need for *ultra-high vacuum* (UHV) is vital to drastically reduce the build up of contaminants and achieve the cleanest sample surfaces. This will consequently improve the IMFP of the electrons outside the solid and hence ameliorate the resolution.

An ultra-high vacuum environment is significantly important in ARPES measurements but not enough, notably for samples that have been exposed to air and therefore have considerable contamination layers on their surfaces. To remove these layers, in-situ sample preparation methods are necessary to achieve and maintain clean surfaces. The three procedures which are usually used for this purpose consist of sputtering and annealing, which relies upon the bombardment of contamination atoms on the surface using inert gases with large kinetic energies and the subsequent annealing of the sample to reconstruct a clean surface. In-situ deposition of material or epitaxial growth techniques and in-situ sample cleaving. The latter is the exclusive technique used in this work.

As illustrated in Fig. 2.11, in-situ cleaving consists of gluing a ceramic 'top post' to the sample surface using silver epoxy (Epotek H21D in our work), and covering the

whole sample surface with epoxy (Fig. 2.11(a)) such that the sample will cleave at the weakest point in the structure after knocking off the ceramic top post, intended to be within the Van der Waals gaps (Fig. 2.11(b)). This method is thus highly desirable for layered materials such as the transition metal dichalogenides, where the weak interlayer bonding allows the breaking of part of the sample.

Chapter 3

Bulk and surface electronic states in the dosed semimetallic $HfTe_2$

This chapter will begin with a description of the crystal structure of 1T-$HfTe_2$ and its underlying symmetries, followed by establishing the link between this material and other TMDs with the transition metals from the group-IV of the periodic table of elements, whose electronic band structures are very analogous to $HfTe_2$, giving rise to intriguing questions about this layered material and making the investigation of its electronic band structure of interest. A review of the previous works devoted to this material and its physical properties will be given, and transport measurements will be extensively described, being a part of the motivation to study this system. The first section will finish by reporting the recent works carried out to investigate the electronic structure of this system, being directly relevant to the work performed in this thesis.

In the following sections of this chapter, we will provide a detailed investigation of the electronic band structure of the pristine $HfTe_2$. A comprehensive description of the obtained k_z dispersion, Fermi surfaces and in-plane electronic band dispersion at different photon energies will be presented, with considerable insights on the used band structure calculations approach to quantitatively explain the particular features in the measured ARPES spectra. Furthermore, the importance of dimensionality reduction in condensed matter physics as a key method in determining exotic physical properties and quantum phenomena will be described, with a focus on alkali metal dosing as an effective way to achieve it. The dosed surface data obtained from both in-plane and out-of-plane momentum dependence ARPES, accompanied with our shallow core levels measurements will be reported, evidencing the effects of alkali metal dosing on 1T-$HfTe_2$, both structurally and electronically. Finally, the topological features supported by the electronic band structure of these materials will be theoretically and experimentally illustrated.

The results presented in this chapter are published in Physical Review B 101, 235431 (2020), DOI: 10.1103/PhysRevB.101.235431.

3.1 Background and motivation

Recently, there has been an increasing interest in semimetallic TMDs, whose properties are still relatively unexplored compared to the semiconducting materials, which have been extensively investigated in the last decade. The crossing of both electronlike and holelike bands of the Fermi level E_F embodies the hallmark of the electronic

band structure of semimetallic systems, and thus underpins their electronic properties.

3.1.1 Crystallography: atomic structure and symmetry

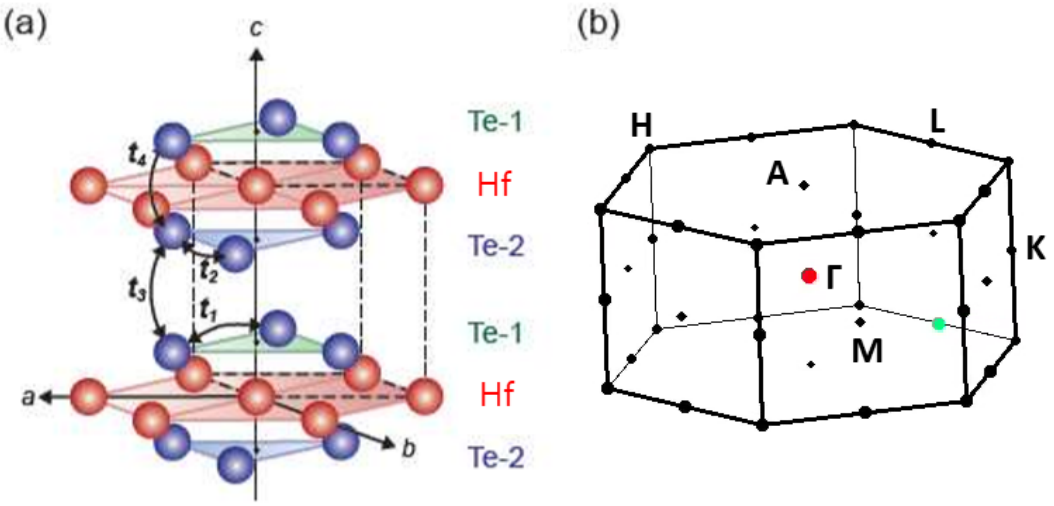

FIGURE 3.1: (a) Crystal structure of 1T-$HfTe_2$ (space group: $P\bar{3}m1$), composed of hexagonal basal planes (ab-planes) of Hf-atom (red sphere) sandwiched between triangular layers with inequivalent Te atomic site (blue sphere) above (Te-1) and below (Te-2) the basal plane along the c-axis. The hopping parameters between 2-site Te p orbitals are categorised as intra-layer hopping ($t_1 = t_2$), interlayer hopping (t_3) within the unit cell and between two unit cells (t_4) [154]. (b) Brillouin zone.

1T-$HfTe_2$ is a transition-metal dichalcogenides material (space group 164, $P\bar{3}m1$) which possesses a C_3 rotational and three mirrors (σ_v) symmetries (C_{3v}). As shown in Fig. 3.1, $HfTe_2$ consists of hexagonal-packed transition metal Hf layers (group IV, $Z = 72$) in red (D_{3d} coordination as indicated by the trigonal structure T), sandwiched between two chalcogen Te ($Z = 52$) layers in blue. In the unit cell, the Hf atoms at the center are octahedrally coordinated to six Te atoms, with the lattice parameters are $a = b = 3.911$Å and $c = 6.649$Å [155]. The upper (Te_1) and lower (Te_2) atomic layers are rotated by 180° between each other, preserving the inversion symmetry within each Te-Hf-Te trilayer. These trilayers are stacked on top of each other (along the c axis) by van der Waals forces, making their exfoliation straightforward and leading thus to few layer or even single layer samples [156].

In reciprocal space, $HfTe_2$ has a hexagonal Brillouin zone, with Γ point being its center. The high symmetry planes Γ-M-K and A-L-H correspond to an out-of-plane momentum $k_z = 0$ and $k_z = \pm\frac{\pi}{c}$, respectively. However, due to the $\bar{3}$ symmetry and octahedrally distorted coordination (D_{3d}), M and M′ points are not equivalent, as for K and K′, L and L′ and H and H′ high symmetry points.

3.1.2 Group IV 1T-TMDs

HfS_2 and $HfSe_2$ are well-established as layered semiconducting materials [72, 73]. In the case of $HfTe_2$, however, the more extensive Te 5*p* orbitals have a larger overlap with the Hf 5*d* orbitals, and results in a semimetallic ground state. Thus, the electronic structure of 1T-$HfTe_2$ has more in common with isostructural 1T-$ZrTe_2$ and 1T-$TiTe_2$, well-known semimetals [157, 158, 159]. The common point between $HfTe_2$ and these layered TMDs or even the isovalent $TiSe_2$ is that the transition metal (Ti, Zr and Hf) belongs to the group *IV* of the periodic table, which dictates both the crystal structure (1T coordination, D_{3d} point group) and the orbital manifolds filling. This results in an analogous electronic band structure for these materials, which consists of a semimetallic (or small indirect band gap semiconducting) nature of the ground state, due to the overlap between the chalcogen *p* orbital derived valence band and the transition metal *d* orbital derived conduction band for $ZrTe_2$, $TiTe_2$ and $HfTe_2$ ($TiSe_2$), giving rise to hole pockets at the Brillouin zone center (Γ and A) and electron pockets at M (L) high symmetry points (Fig. 3.2).

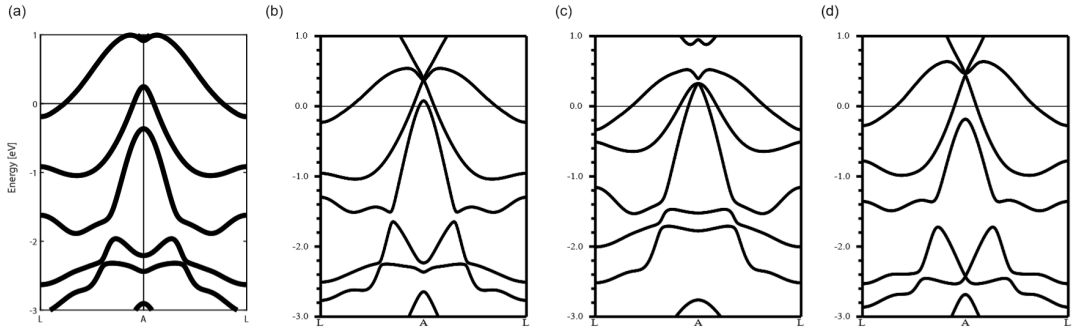

FIGURE 3.2: Low-energy electronic band dispersion of (a). $HfTe_2$, (b). $TiSe_2$, (c). $TiTe_2$ and (d). $ZrTe_2$ as performed with standard DFT calculations using GGA functional, showing the Te (Se) *p* orbital derived valence band at A (Γ) point and the Hf (Ti, Zr) *d* orbital derived electron pockets at the conduction band at L (M) point.

In early reports, $HfTe_2$ was assumed to be very similar to 1T-$ZrTe_2$ [160], another semimetal of the TMDs family, with the transition metal belonging to group *IV*, and their electronic properties were found to be closely analagous, as they are both semimetallic with a simple electronic structure and the absence of any phase transition [75]. $ZrTe_2$, however, has received less attention compared to the other compositions and crystal structures such as $ZrTe_3$ and $ZrTe_5$, which possess exotic physical properties [161, 162, 163, 164, 165, 166]. In a very recent study on epitaxially grown thin films, where ARPES measurements and DFT calculations were performed, $ZrTe_2$ has been suggested to host massless Dirac fermions [167], as another example of layered materials which support the existence of topologically nontrivial phases, characteristic of TMDs which possess a C_3 rotational symmetry [13]. However, due to the limited energy resolution of UV-HeI lamp (21.22 eV) ARPES experiments [167], further investigations, especially photon-energy-dependent measurements, are strongly required to confirm the observed bulk Dirac point (BDP) and verify the existence of other topological features such as an inverted band gap.

1T-$TiTe_2$ is another semimetallic TMDs material which has been extensively investigated, and whose band structure is very similar to $HfTe_2$. The attraction to study

$TiTe_2$ was mainly due to its interesting structural and electronic properties [157, 168, 158, 169, 170, 171, 172, 173, 174, 175, 176]. First, $TiTe_2$ has been considered as a model material of Fermi liquid in ARPES [157, 168, 158, 169], more importantly, phonon coupling has been suggested to induce superconductivity in this material [172, 174, 175], while the appearance of nontrivial topological surface states under pressure was predicted [170, 171]. In particular, single-layer $TiTe_2$ has been claimed to undergo a charge density wave phase transition at 92 ± 3 K [173]. The similar electronic band structure and the absence of phase transition in the bulk make a good resemblance between 1T-$TiTe_2$ and 1T-$HfTe_2$. In this respect, the understanding of quantum phenomena in both bulk and monolayer $HfTe_2$ is of great importance to disentangle the underlying mechanisms of any such exotic properties and explore potential applications of this system.

The experimental determination of the electronic band structure of $HfTe_2$ will be extensively explained below, where the results will be presented, obtained from both high-resolution ARPES experiments and orbital-projected Density Functional Theory (DFT) calculations, including the in-plane band dispersion at different photon energies, measured Fermi surfaces, and photon-energy-dependent ARPES, giving detailed insights underlined within the electronic band structure of this prototypical layered semimetal.

3.1.3 Literature review

Characterization of the physical properties

Early studies on the layered TMD $HfTe_2$ consisted of X-ray diffraction experiments, and focused on the crystalline structure and symmetry, lattice parameters and details of the composition and phase density, demonstrating a non-stochiometric structure of $HfTe_2$ arising from random vacancies on the Te sublattice [177, 160]. Further characterization of the synthesis and electrical properties showed $HfTe_2$ to have a metallic conductivity, as a consequence of the band overlap between Te p and Hf d orbitals [178, 75]. Klipstein *et al*. [179] carried out more transport properties measurements, and estimated the semimetallic band structure of $HfTe_2$ with a band overlap of $\sim$0.3 eV, and although some anomalies in the low-temperature transport properties at ambient pressure were observed, no structural instabilities such as a charge density wave were reported. Later investigations on the thermopower and electrical resistivity demonstrated the absence of any phase transition in $HfTe_2$, with the complications in the transport data arising from the different temperature-dependence mobility of the electrons and holes [180, 181]. A theoretical study of the electronic and optical properties of $HfTe_2$ using *ab initio* calculations confirmed the semimetallic nature of its ground states, having a density of states of $\sim$0.9 states/eV.unit cell at Fermi level [182].

Interpretation of the transport measurements

One of the most prominent reasons for the recent attraction to investigate semimetals is the exhibition of peculiar transport properties, manifested principally in their large and non-saturating magnetoresistance (MR), as well as novel electronic states and topological features [155]. This large MR in semimetals has been suggested to be often attributed to the topological features within their nontrivial electronic

structure, such as Dirac or Weyl fermions, as it is the case for WTe_2 and $MoTe_2$ [155]. However, even in the absence of Dirac or Weyl points, at the Fermi level vicinity at least, $HfTe_2$ still reveals a large non-saturating MR of 1350% at T = 2 K and $\mu_0 H$ = 9T, raising thus intriguing questions about the origin of the large MR in this material [155].

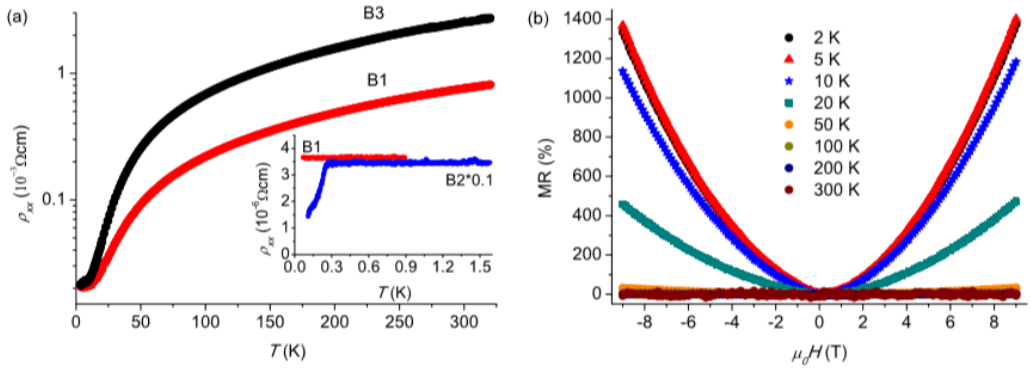

FIGURE 3.3: Magnetotransport properties of $HfTe_2$. (a) the temperature dependence of the in-plane electrical resistivity ρ_{xx} (H = 0,T) for different samples; the inset shows the resistivity of B1 and B2 down to 0.1 K. (b) Field dependence of the transverse magnetoresistance (MR), ρ_{xx} (H,T), for HfTe2 (crystal B3) for selected temperatures. Taken from [155].

As mentioned above, the particularity of semimetallic materials consists of the existence of electrons and holes in their Fermi surface, leading to their contribution, both, to the electrical conductivity of the system [155]. Within the framework of the orbital magnetoresistance, as well as the carrier mobility, this compensated Fermi surface is the keystone to explain the MR effect, and thus higher (perfect) carriers compensation consequently yield larger MR [155, 183].

Although fundamentally governed by the carriers compensation at the Fermi level, there are major limiting factors to MR value, notably the sample purity [183]. For instance, a direct link of sample purity, illustrated in its residual resistivity ratio (RRR), the carrier mobility and the MR value is well established [155, 183]. This makes the sample synthesization approach of extreme interest, especially when the material under consideration is particularly demanding, as it is the case for $HfTe_2$, which is very air-sensitive and reveals substantial intrinsic purity issues, arising mainly due to the complex separation of Hf and Zr [183]. Indeed, different crystal growth methods gave strikingly different results. Mangeslen et *al*. [183] performed measurements of the physical properties of $HfTe_2$ depending on the protocol of synthesis. Whilst the best chemical vapor transport (CVT) grown crystal shows a RRR of 262 and a MR of 5950%, the crystals obtained with the Te self-flux procedure exhibit RRR and MR values of 404 and 9480%, respectively, greatly exceeding the previous reported values [155].

The empirically larger success of the self-flux protocol is attributed to the absence of a transport agent as source of defects in this method, as well as its ability to significantly reduce the Zr impurities compared to the CVT. All these evidences confirm the intimate interdependence between the carrier compensation, the carrier mobility,

the purity, the RRR and the MR [183]. Finally, the detailed investigation of the electronic band structure of $HfTe_2$, and notably its Fermiology, is of utmost importance, as this can provide clear insights for the unusual properties of this compound, which makes it of interest for both fundamental research and promising applications.

Electronic structure

Recently, more investigations, either on MBE grown $HfTe_2$ thin films or single crystals, including electron diffraction, STM and more relevant for this thesis, DFT calculations and ARPES measurements have been performed, giving more insights about both the structural and electronic structure of this material [184, 155, 185, 186, 183]. Aminalragia-Giamini *et al*. claimed that 1T-$HfTe_2$ might be classed as a topological Dirac semimetal [184], while the transport measurements carried out by Mangelsen *et al*. showed a notably large and non-saturating magnetoresistance, resulting from the carrier compensation [155, 183]. Using first-principle calculations, Cheng *et al*. uncovered a hidden spin polarisation in monolayer $HfTe_2$ [185], following the mechanism suggested previously for centrosymmetric 1T-TMDs [187]. Much closer to the first part of the data presented here, Nakata *et al*., using ARPES measurements and DFT calculations, observed a dimensionality crossover in the electronic structure of $HfTe_2$ upon dosing with alkali metal [186].

3.2 DFT calculations: effects of the used functional

DFT calculations presented here were performed within the Wien2k package [188], accounting for spin-orbit coupling. The modified Becke-Johnson (mBJ) functional [17] was implemented. The used lattice parameters are $a = b = 3.911$Å, $c = 6.649$Å and $z_{Te} = 0.266$ [155], and the $R_{MT}K_{max}$ parameter was equal to 7.0.

The merit of the used functional in the DFT calculations is seen best in the sketched 3D Fermi surface in Fig. 3.4(a,d). Whether or not the Fermi surface is closed (i.e. a 3D pocket, as in $TiSe_2$ and $TiTe_2$ [189, 86]) or open along k_z (i.e. forming a warped 2D cylinder) is a subtle question, but important for the understanding of transport data [155, 183]. In DFT calculations using the Generalized Gradient Approximation (GGA) functional the pockets are open along kz (Fig. 3.4(a)), but GGA calculations also give an unrealistically large overlap of the Te 5p and Hf 5d states. Using the mBJ functional, however, gives a much more accurate low-energy band structure, and yields a closed electron pocket around the L points and a much smaller hole pockets at the Brillouin zone center (Fig. 3.4(d)). Therefore, the mBJ functional results in a much reduced band overlap, as shown in the DFT calculations of the near Fermi level along M'ΓM and L'AL directions; in other words, the lowest Hf 5d state at the M point in Fig. 3.4(e) is slightly above E_F, compared to the GGA-based DFT calculations in Fig. 3.4(b), while at the L point, the conduction band minimum reduces from 500 meV in the standard DFT (GGA) in Fig. 3.4(c) to $\sim$ 200 meV in the semi-empirical mBJ functional DFT calculations (Fig. 3.4(f)). However, the position of the electron pockets at the L point still appears to be slightly deeper with respect to the experimental data, as will be shown in the following sections. This small overestimation arises from the limitations of the accuracy of the functional. In this regard, the Heyd–Scuseria–Ernzerhof (HSE) exchange–correlation functional or GW approximation [18, 19] are expected to give an even better agreement between

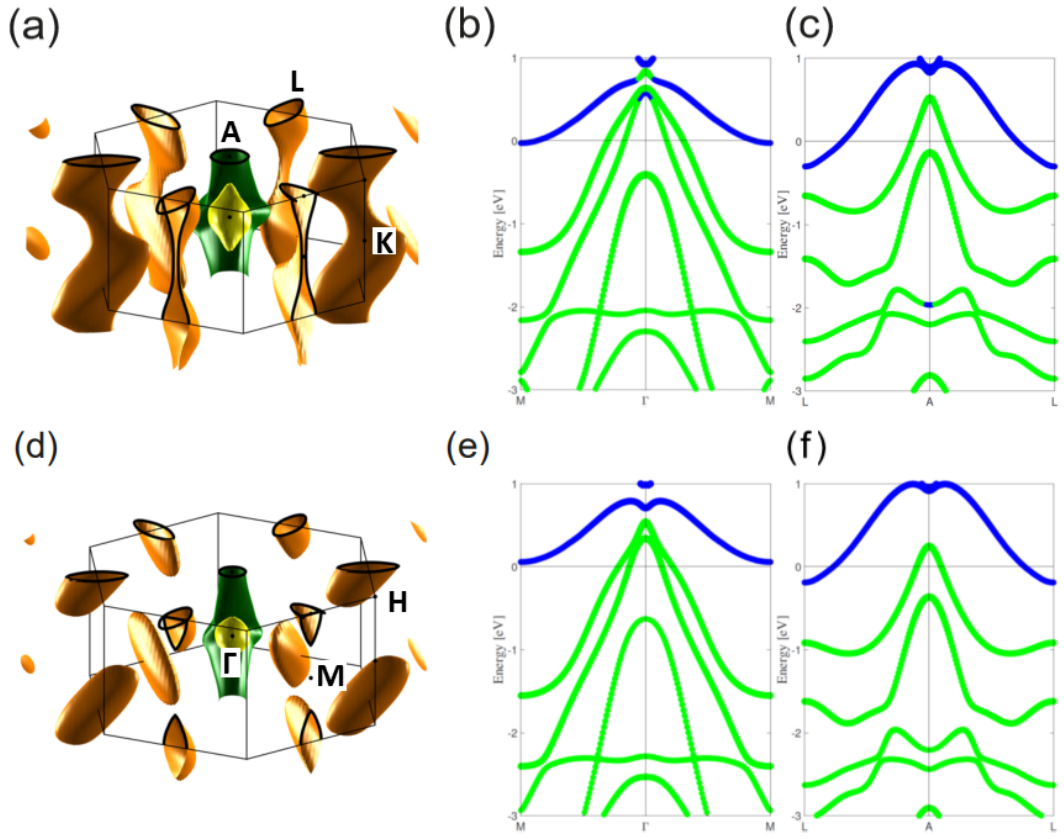

FIGURE 3.4: 3D Fermi surface of $HfTe_2$ and near Fermi level electronic band structure along ΓM and AL direction, as calculated by a standard DFT course using the GGA function (a-c) and the mBJ functional (d-f).

the DFT and the ARPES measured data. However, the fact that they are "computationally very expensive" makes them less appealing from an experimentalist point of view.

3.3 The 3D bulk character of the electronic band structure of $HfTe_2$.

Our DFT calculations with the orbital character projection (Fig. 3.5) gives an overview of the electronic structure. We have a manifold of 6 bands deriving from Te $5p$ orbitals, which are mostly occupied but reach up to the Fermi level around the Brillouin zone center (Γ and A points), forming hole pockets. Conversely, the bands deriving from Hf $5d$ orbitals are mostly unoccupied, but dip below the Fermi level to form electron pockets around the L points. Thus, $HfTe_2$ is a compensated semimetal, though the hole and electron pockets have very different orbital characters.

Although $HfTe_2$ is a layered material, the out-of-plane dispersion is crucial to understand the full three-dimensional electronic structure. In the calculation in Fig. 3.5 at the A point, two hole-like bands are present near E_F. These derive from Te $5p_{x,y}$ orbitals only, but the separation of the bands due to the spin-orbit coupling is so large ($\sim$ 0.65 eV) that the lower branch is shifted fully into the occupied states, leaving

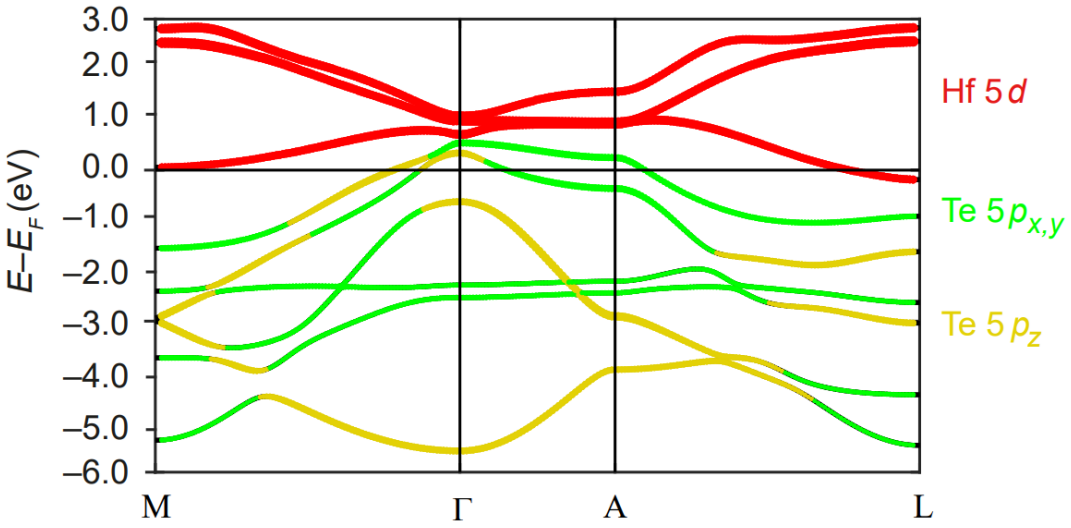

FIGURE 3.5: Electronic structure of 1T-$HfTe_2$. DFT calculations along M-Γ-A-L direction with orbital character projection of the valence and conduction bands.

a single hole pocket here. At the Γ point, three bands are present as the $5p_z$ orbital is also relevant, but again there is a strong spin-orbit interaction which mixes the orbital character and separates the bands; the result is a pair of hole bands crossing E_F and a lower hole band which remains fully occupied. Thus, as illustrated in the 3D Fermi surface in Fig. 3.4(d) and Fig. 3.8(a), only one hole band crosses E_F at the A point (green band), but two hole pockets exist around Γ (green and yellow bands).

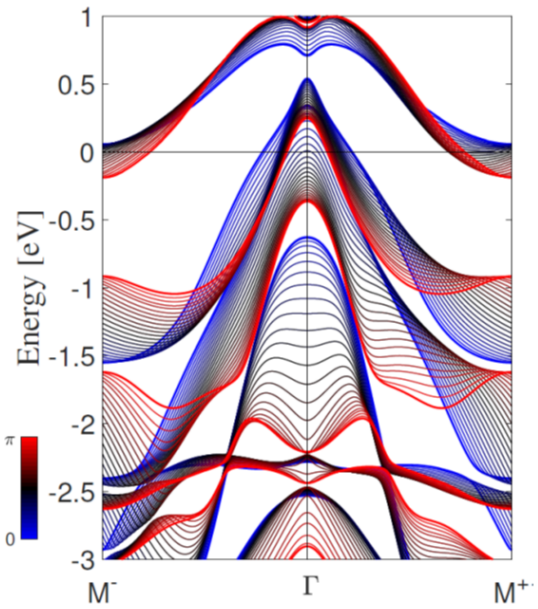

FIGURE 3.6: Simulation based on DFT calculations using the mBJ functional of the low-energy electronic band structure of $HfTe_2$ along $\bar{\Gamma}\bar{M}$ direction, using 25 k_z slices between $k_z = 0$ (M'ΓM direction, blue spectra) and $k_z = \pi/c$ (L'AL direction, red specra).

The 3D character of the electronic band structure of $HfTe_2$ is well highlighted in the

simulation depicted in Fig. 3.6, where 25 k_z slices are projected between $k_z = 0$ (M'-Γ-M direction) and $k_z = \pi/c$ (L'-A-L direction). At the L point, a clear electronlike conduction band is observed (red), but the band disperses significantly along the k_z axis such that it is well above Fermi level at M point (blue curve). At the Brillouin zone center, however, the crossing of holelike electronic bands to the Fermi level gives rise to two hole pockets at the Γ point and a third band at ~ 0.7 eV (blue bands). When moving along the k_z axis from $k_z = 0$ to $k_z = \pi/c$, the top valence band pair of Te $5p_{x,y}$ shift slightly downwards to higher binding energies, leaving only one hole pocket at the A point, whereas the p_z orbital character causes a strong out of plane dispersion of the third band, resulting thus in a M-shaped band at ~ 2.0 eV (red bands). Note that the spin-orbit coupling is very large in $HfTe_2$ that it significantly hybridizes the electronic valence bands and causes most of them to have a mixed orbital character (Fig. 3.5). Therefore, as highlighted in Fig. 3.7, along Γ-M direction (Fig. 3.7 (a)), two holelike electronic bands cross the Fermi level, with a third one at ~ 0.7 eV, although no electron pockets are present here. Whereas along A-L, only one holelike band crosses the Fermi level with a Te $5p_z$ orbital-derived M-shaped band at ~ 2.0 eV at the A point, with electron pockets centered at each L point of the Brillouin zone (Fig. 3.7 (b)).

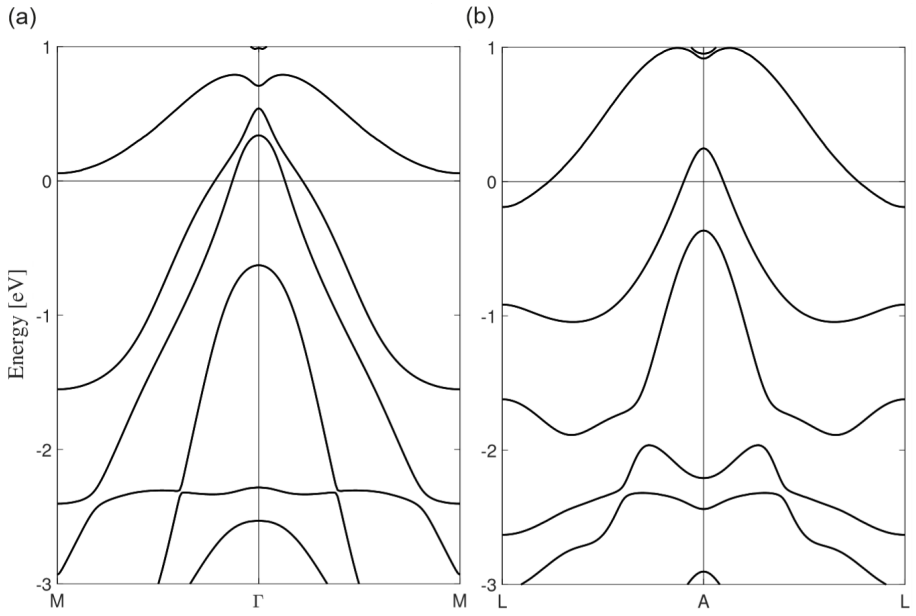

FIGURE 3.7: Low-energy electronic band structure of $HfTe_2$ along (a) ΓM and (b) AL direction of the Brillouin zone, as performed by DFT calculations.

3.4 ARPES measurements

In the results presented in this chapter, the photon energy was varied between 80 and 120 eV, and the light was linearly polarized in the horizontal plane (LH, or p polarization). The samples were commercially obtained from HQ Graphene, cleaved in situ and measured at a temperature of T = 10 K, and the energy resolution was typically 10 meV.

3.4.1 Fermi surface

Fermi surface is fundamental to explain transport and other physical properties in condensed matter physics [190]. As introduced in Chapter 2, Fermi-Dirac distribution dictates that electrons can only fill up energy states up to Fermi level E_F at T = 0 K (Eq. 2.11), therefore, Fermi surface is the boundary between the occupied and unoccupied electronic states, making it very crucial since the electrical and thermal properties of a material arise solely from electrons near this region. This is characteristic of a metal, for an insulator or a semiconductor, where Fermi level falls in a gap between the valence and conduction band, there is no Fermi surface. Fermi surface can be probed either by quantum oscillations measurements [191] or, in the frame of this thesis, by ARPES. Its topology reflects the symmetry and structure of the crystalline lattice, and the occupation of the electronic states. In the case of the semimetallic 1T-$HfTe_2$, for instance, both electron and hole pockets are present in the Fermi surface, resulting from the multiple bands crossing of the Fermi level along the out-of-plane k_z momentum.

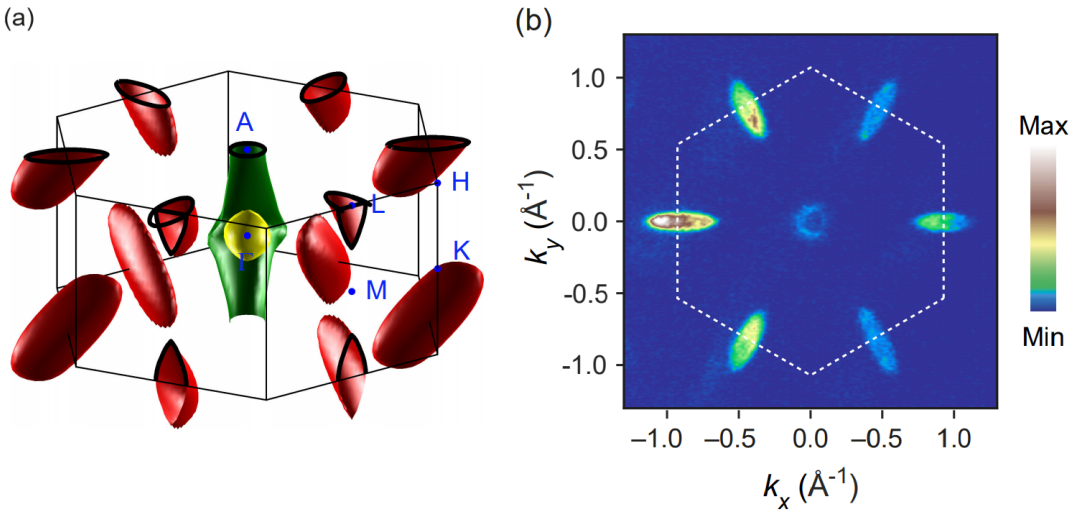

FIGURE 3.8: (a) 3D Fermi surface of $HfTe_2$ calculated with a DFT code using the mBJ functional. Hf 5d orbital-derived electron pockets are sketched in red, whereas green and yellow colours represent Te 5$p_{x,y}$ and Te 5p_z orbital-derived hole pockets, respectively. (b) Constant energy map at E_F (Fermi surface), measured at a photon energy $h\nu$ = 100 eV to probe the A-H-L plane. The threefold in-plane intensity distribution of the electron pockets located at the L points reflects the trigonal symmetry of the crystal structure.

Fig. 3.8 (a) depicts the three-dimensional Fermi surface of $HfTe_2$, as performed by DFT code. A vase-shaped valence band hole pocket disperses along the rotation axis (k_x=0, k_y=0, k_z), confirming its 3D character, with a single Te 5$p_{x,y}$ orbital-derived hole pocket at $k_z = \pm\pi/c$, and an additional one at the Brillouin zone center (k_z = 0), derived from Te 5p_z orbitals. On the other hand, six Hf 5d orbital-derived electron pockets are centered at L points of the Brillouin zone. These conduction band electron pockets are strongly three-dimensional, as obvious from their closing along the k_z axis, resulting in a clear electronlike conduction band at L points but not at M points of the Brillouin zone, as shown in the in-plane electronic band dispersion in Fig. 3.7, where the band form electron pockets at L but it is well above E_F at M point. As highlighted in the 3D Fermi surface in Fig. 3.8 (a) also, the electron pockets

substantially tilts away from the k_z axis. The threefold symmetry of the crystalline structure ($\bar{3}$), however, dictates that the the pockets centered at L and L' point tilt in opposite direction along the k_z axis. Furthermore, the electron pockets have an elliptical cross section in the k_x-k_y plane, evident in a constant energy map at E_F measured at a photon energy $h\nu = 100$ eV, chosen to probe the A-H-L plane ($k_z = \pi/c$, Fig. 3.8 (b)).

As exlained in Chapter 2, the damping of the final state in the z direction [143, 140], normal to the sample surface dictates that the k_z is not strictly conserved in the photoemission process [136], which results in a significant k_z broadening, especially in 3D systems. In general, the existence of multiple possible final states, and their non-parabolic dispersions, makes the full treatment of photoemission a complex problem. The commonly used approximation is the so-called free-electron final state model, which assumes a simplistic dispersion for the final state that allows a mapping between the photoelectron kinetic energy and the k_z value of the initial state.

Since the k_z dispersion of the initial state in $HfTe_2$ is clearly as significant as the k_x, k_y directions, the "uncertainty" in k_z will have an important impact on the measured spectra. Thus despite the large success of the free-electron final state approximation for $HfTe_2$, our measurements at a given photon energy appear to probe a distribution in k_z, rather than a sharply-defined value. Such k_z broadening is evident from the constant energy map in Fig. 3.8 (b). Here, the electron pockets are "filled-in", with intensity localised within the bounds of the electron pocket, but we do not observe sharp ellipsoidal countours that might be expected from slicing the 3D Fermi surface in the $k_z = \pi/c$ plane (Fig. 3.8 (a)). The effect of k_z uncertainty is more pronounced for the electron pockets as they have a slanted 3D shape. Whereas the hole pocket is centered on an axis of rotation ($\bar{3}$) which forbids any such slanting, and thus appears relatively sharp at the A point.

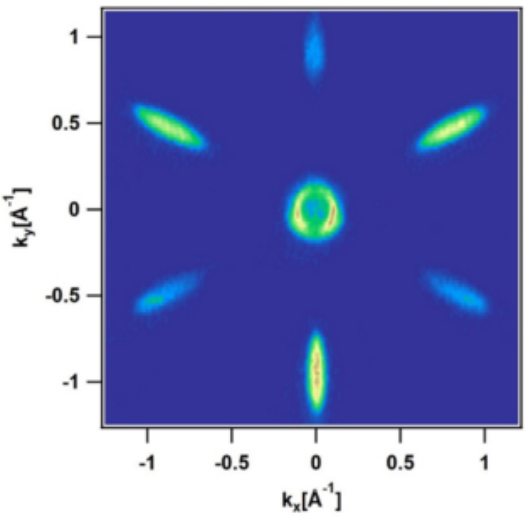

FIGURE 3.9: Constant energy map at E_F, measured at a photon energy $h\nu = 80$ eV to probe the Γ-K-M plane. The observed electron pockets result from the k_z broadening in the photoemission process, and not quasiparticle bands existing at M points.

The threefold symmetry of the system is more pronounced in the constant energy

map in Fig. 3.9, measured at a photon energy $h\nu = 80$ eV to probe the Γ-K-M plane. As expected from the 3D Fermi surface in Fig. 3.8 (a), two hole pockets are present at the Brillouin zone center. However, the existence of electron pockets can be misleading, since no such pockets would be expected from slicing the 3D Fermi surface in the $k_z = 0$ plane. This is another picture reflecting the significant k_z uncertainty in the photoemission process. The observed features here arise solely from signals collected from inital states at $k_z \neq 0$ at the bottom and top of the electron pockets above and below the $k_z = 0$ plane, respectively, as might be understood from their weak spectral weight compared to cuts at other photon energies ($h\nu = 100$ eV, Fig. 3.8 (b)). Therefore, only the two hole pockets are expected at the Γ-K-M plane, but the k_z uncertainty leads to additional intensity at M points which are in reality absent at the specific value of $k_z = 0$. Such effects are more prominent in the dosed surface, as will be shown in the photon-energy-dependent ARPES in Fig. 3.16.

3.4.2 Valence band dispersion: assymetries and uncertainty in the spectral function of $HfTe_2$

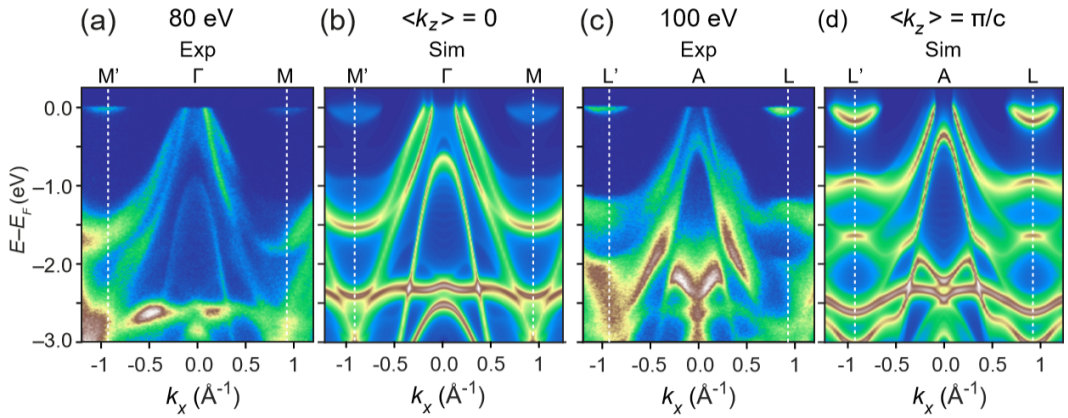

FIGURE 3.10: (a,c) Valence band dispersion along Γ-M ($h\nu = 80$ eV) (a) and A-L direction ($h\nu = 100$ eV) (c). (b,d) Simulations based on DFT calculations, averaging over a substantial fraction of the Brillouin zone width in the k_z direction. Panels (b),(d) correspond to an average k_z value of $k_z = 0.0\pi/c$ and $k_z = \pi/c$ respectively.

The measured high-symmetry dispersions are also influenced by the uncertainty in k_z. Therefore, we do not simply compare the measurements with the calculated dispersions from DFT, which assume a particular k_z value. Rather, we simulate the effect of k_z broadening by averaging over a substantial fraction of the Brillouin zone. We first construct a spectral function for each calculated k_z by adding a finite scattering rate of 50 meV to the calculated in-plane band dispersions, and then perform a summation over k_z in which the weight of each k_z slice is modelled by a Lorentzian distribution with FWHM of $0.2 \times (\frac{2\pi}{c})$.

Since the 80 eV data in Fig. 3.10 (a) corresponds to a Γ point, according to the free-electron final state approximation, the simulation in Fig. 3.10 (b) is centered around $k_z = 0$. Matrix elements are not included in the simulation, and the variation of k_z with in-plane momentum is not accounted for. Moreover, the calculated band energies are typically ∼100 meV offset compared to the experiments, and correspondingly both the hole and electron pockets are larger in the calculation than in the

experiment. However, there is excellent correspondence in understanding where features are sharp in the data (e.g. the inner hole pocket) or rather broader, due to the k_z averaging effect [192]. Some weak spectral weight of the electron pockets appear at the M points, however, this should be understood strictly as a result of smearing of spectral weight along k_z, and not as quasiparticle bands existing at M. At the L points, in Fig. 3.10 (c), the electron pockets are brighter and better defined, though somewhat smaller than in the simulation based on DFT projection in Fig. 3.10 (d), due to the limitations of the accuracy of the functional.

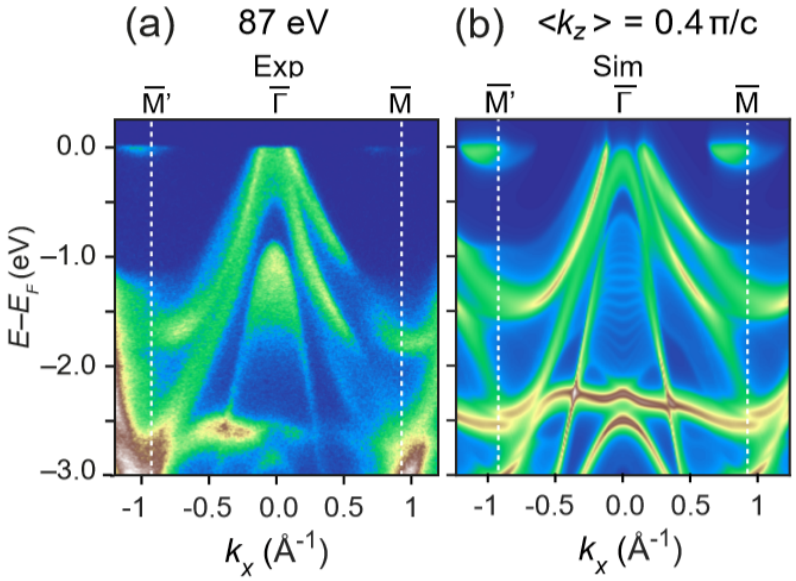

FIGURE 3.11: (a) Valence band dispersion at an arbitrary k_z between Γ and A point ($h\nu = 87$ eV). (b) Simulations based on DFT calculations averaging over a k_z value of $k_z = 0.4\pi/c$,

The merit of this approach is seen best for data measured away from any high-symmetry k_z value, such as in Fig. 3.11 (a). Here, the data show a substantial asymmetry, as well as a large degree of broadening. However, these complexities are well-captured by the simulation in Fig. 3.11 (b), where the k_z distribution is centered at $0.4\pi/c$. The asymmetry in the spectrum arises because of the $\bar{3}$ symmetry; away from the high-symmetry k_z=(0, $\pm\pi/c$) planes, band dispersions towards the $\bar{M}$ and $\bar{M}'$ directions are not equivalent. The simulation also shows that the spectral weight of the electron pocket is centered away from the $\bar{M}$ point, which is due to the slanting of the electron pockets. The spectral weight is shifted inside the Brillouin zone near the $\bar{M}$ point and outside of the first Brillouin zone at the $\bar{M}'$ point. Therefore, in the general case we expect threefold and not sixfold symmetry in measured "Fermi maps", which is already present to some degree in Fig. 3.8 (b) but is pronounced in measurements at other photon energies (Fig. 3.9) [176]. Overall, then, the agreement with our simulation based on DFT calculations confirms that the observed features are projected bulk bands resulting from the k_z uncertainties during the photoemission process.

3.5 Dimensionality reduction by potassium K dosing on the surafce

Dimensionality reduction plays a crucial role in the emergence of novel physical properties in condensed matter physics [51, 89, 193, 90, 91, 91, 116, 194, 195]. A 3D to 2D crossover can lead to exotic physical properties and quantum phenomena absent in the bulk counterparts, ranging from massless Dirac fermions in Graphene [51], valley-selective circular dichroism [193, 90, 91, 45] to the enhancement of CDW temperature in TMDs [116]. The emergence of these physical properties goes hand-in-hand with significant changes of the electronic band structure, such as an indirect to direct bandgap transition [89, 196, 197] or a Rashba-like spin-splitting due to the inversion symmetry breaking (ISB) [198, 33].

Widely used approaches to control the dimensionality reduction would be the chemical or mechanical exfoliation (top-down approach) [199], or MBE or CVD, which consist of the deposition of atoms or molecules on a substrate (bottom-up approach) [200, 201, 202, 102]. A more effective way for a systematic control of the dimensionality of a material, notably a TMD, alongside with the evolution of the electronic band structure can be achieved by alkali metal evaporation on the surface.

Alkali metal deposition on layered materials has turned into a commonly used approach in angle-resolved photoemission spectroscopy (ARPES) experiments, due to the possibility to stabilise and tune novel electronic states with properties that can significantly differ from those of the pristine material. It has been shown that dosing can suppress the charge density wave (CDW) phase in $TiSe_2$, and induce a metal-to-insulator transition alongside with a novel CDW phase in TaS_2 [203]. In the semiconducting Black Phosphorus, the bandgap was tuned via K dosing, prompting the emergence of Dirac fermions due to the surface Stark effect [204, 205, 206, 207]. This effect has been announced as a universal mechanism of band-gap engineering in 2D semiconductors [31]. Besides, dimensionality reduction, whether upon alkali metal evaporation, hydrogenation or water vapor exposure has been widely reported [208, 30, 33, 186, 209, 28].

It has been suggested that dosing semimetals could be qualitatively different to dosing semiconductors [33]. In semiconductors, the most familiar scenario is "band-bending", where a strong variation of the electrostatic potential near the surface results in the effective spatial confinement and emergence of quantum-well-like states [28, 29, 30, 31]. Whereas in semimetals, the existence of both hole-like and electron-like free carriers makes the underlying mechanism complex to predict [33]. On the other hand, in some cases the alkali metals are known to migrate into the van der Waals gaps of the sample, decoupling a top layer with a monolayer-like electronic structure [208, 186].

There are several factors which play a crucial role in making one scenario more favourable to occur compared to the other. First, it is believed that at low dosing amounts and low temperatures, the alkali metal atoms are more likely to stay at the surface (Fig. 3.12(b)), whereas higher dosing amounts and higher temperatures favour the intercalation scenario (Fig. 3.12(a)). The third factor is the time, and it has been experimentally proven using XPS that immediately after the evaporation, the alkali metal atoms are still on the surface, while few minutes afterwards (10 min)

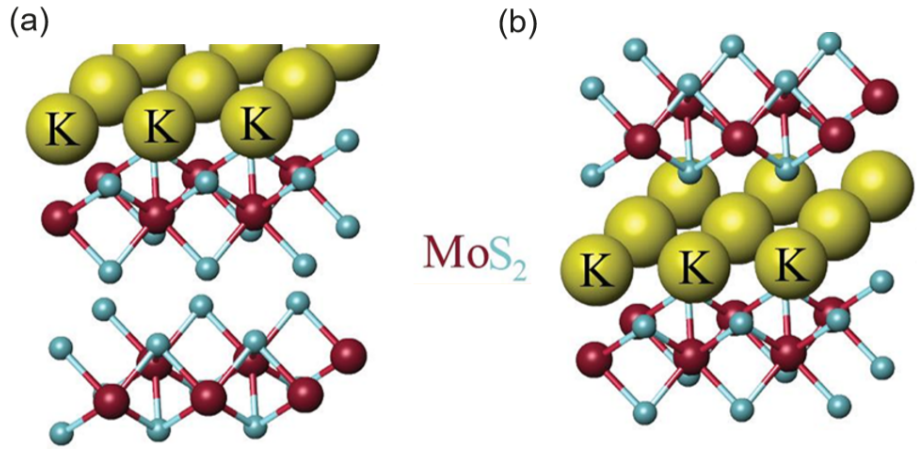

FIGURE 3.12: Scenarios of the alkali metal dosing of TMDs. (a) Adsorption of the alkali metal atoms on the surface, resulting in a band-bending model, consisting of the effective spatial confinement of the charge carriers at the surface along the out-of-plane axis and emergence of quantum-well-like states. (b) Intercalation of potassium K atoms within the first vdW gaps, decoupling the topmost layer both structurally and electronically and resulting in a quasi-free standing monolayer [208].

they have already migrated to the vdW gaps [208]. Lastly, the alkali metal atoms size is as well considered to affect the resulting scenario. Rb is often used to avoid intercalation due to its large atomic size [31], while in the case of Na or K, intercalation is expected to take place, resulting thus in quasi-free standing monolayer, as sketched in Fig. 3.12(a).

3.6 Tuning the electron density by K dosing

We now turn to the question of how a 2D electronic structure can emerge upon K dosing of the surface of $HfTe_2$. Before the presentation of the obtained results and their interpretation, we start this section by the introduction of Luttinger's theorem, which was used to estimate the electron carrier density n_e from the area of Fermi surface at each level of alkali metal dosing.

To estimate the size of the Fermi surface after every dosing sequence, the Fermi wave vectors along the shorter k_s and longer k_l axes of the ellipsoidal electron pockets are extracted from the Momentum Distribution Curves (MDCs) and fitted with Lorentzian functions. Luttinger's theorem can therefore be written as follows:

$$n_e = g_s \times g_v \times \frac{k_s \times k_l \times \pi}{BZ_{area}} \tag{3.1}$$

with $g_s = 2$ is the spin degeneracy factor, $g_v = 3$ is the number of electron pockets within the Brillouin zone (valley degeneracy) and $k_s \times k_l \times \pi$ represents the surface of the ellipse. Whilst the area of the hexagonal Brillouin zone is given by:

$$BZ_{area} = \frac{3\sqrt{3}}{2} \times \frac{4}{3}[\frac{\pi}{a}]^2 \tag{3.2}$$

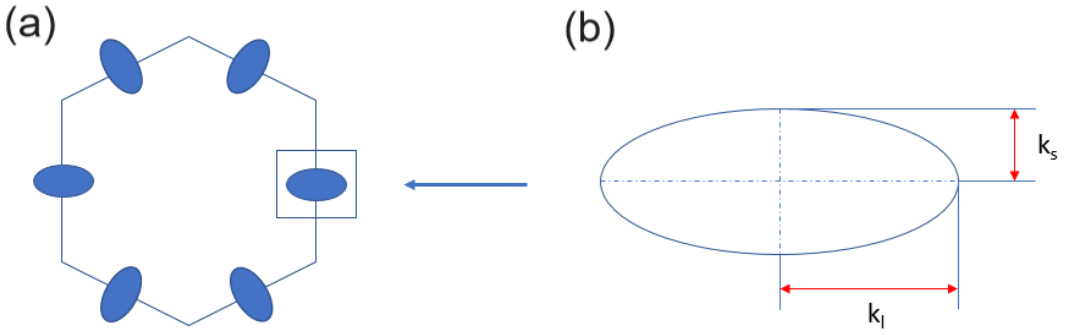

FIGURE 3.13: Cartoons of Fermi surface of 1T-$HfTe_2$ highlighting the semi-major k_l and semi-minor k_s axis of the elliptic electron pockets, estimated as a function of potassium K dosing by fitting the extracted MDCs with a Lorentzian function.

with $a = 3.911$Å is the in-plane lattice parameter of $HfTe_2$.

3.6.1 Emergence of monolayer-like electronic structure by K dosing

At first glance, the ARPES data in Fig. 3.14(a-c) might seem like a simple rigid shift of the band structure, where the electron pockets start to become substantially occupied and the hole pockets eventually shift fully into the occupied states, reaching an effective carrier density of n_e=0.32 el/u.c in Fig. 3.14(c). However, there are a number of important effects beyond the rigid shift model. First, the bands in the heavily-dosed spectra (Fig. 3.14(c)) appear sharper than in the pristine bulk case (Fig. 3.14(a)). The increased sharpness is somewhat counter-intuitive, since in many cases surface dosing (and doping more generally) goes hand-in-hand with increased disorder, thereby leading to broader, not sharper, linewidths [31]. We must consider, however, that for the pristine surface, the k_z-broadening effect is the dominant source of linewidth broadening for most of the bands. The increasing sharpness is therefore the first experimental signature that the states that emerge after dosing have 2D character, with wavefunctions confined to the topmost layer of $HfTe_2$, thus suppressing the k_z-broadening. Similar phenomenenology has been observed in other TMDCs with more 3D characteristics in their bulk electronic structure [33]. The sharpness also confirms that the K coverage must be homogeneous, at least on the scale of the beam spot size.

A recurrent question in the study of alkali-metal dosed surfaces of 2D materials is whether the dosed atoms remain on the surface and set up a vertical electric field, or intercalate into the sample [203, 204, 205, 206, 31, 208, 30, 33, 186, 209, 28, 29, 210, 211, 85, 212, 213]. A number of recent studies on TMDCs and similar materials have claimed that the alkali metal atoms remain on the surface [30, 204, 205, 206, 31, 213, 33, 207], in the case that the sample remains at low temperatures throughout. In this scenario, the alkali metal ions create a charge accumulation at the surface, causing a band-bending potential that affects primarily the top-most layer of the TMDC. The new bands that emerge thus appear electron-doped compared with the bulk, and their wavefunctions are localised close to the surface [29, 33]. Without detailed calculations, we cannot specifically predict what band dispersions would be expected in our case, however it would be reasonable to imagine that, broadly speaking, the conduction band will become increasingly filled, while the observed valence bands

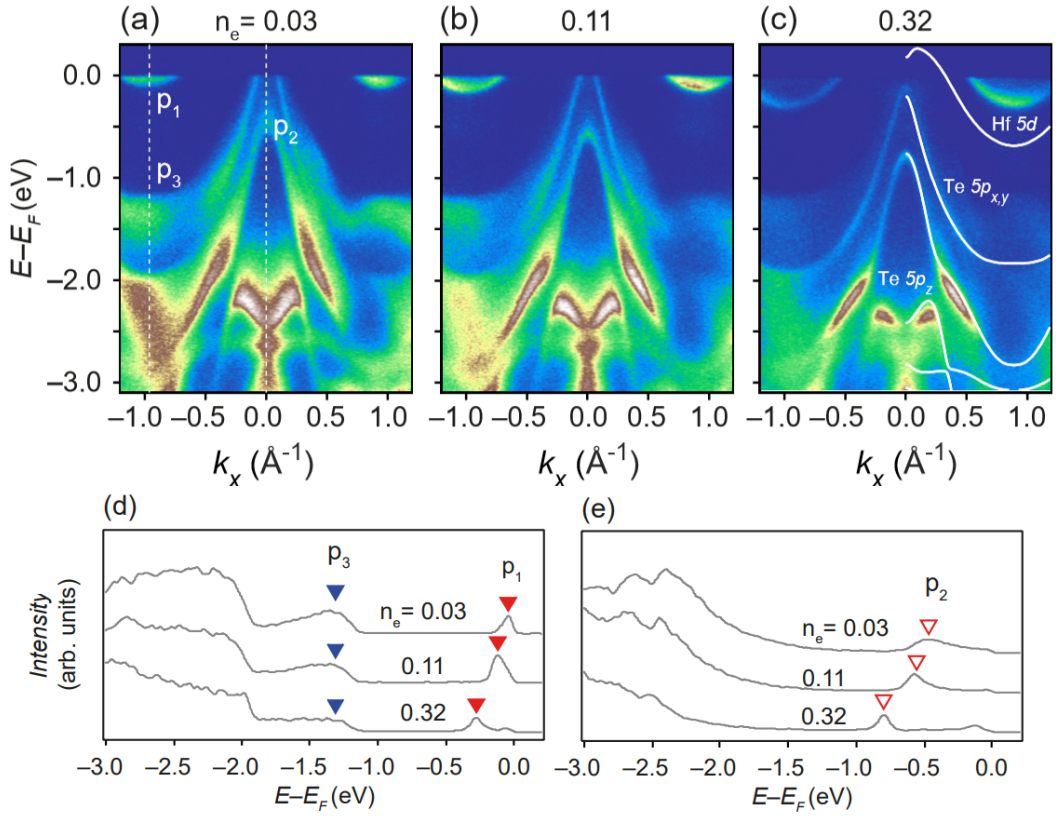

FIGURE 3.14: Dosing sequence of $HfTe_2$ at $T = 10$ K, measured at a photon energy of $h\nu = 100$ eV. (a) Valence band dispersion along A-L direction of the pristine surface, (b) at a carrier density of n_e=0.11 and (c) at n_e=0.32 el/u.c., together with $HfTe_2$ monolayer DFT calculations (white solid lines), shifted downwards by 650 meV. Due to the overestimated band overlap in DFT, the energy of the electron pocket is lower in the calculation than the data, however the agreement on the valence band structure is more important here. (d) Energy Distribution Curves (EDCs) showing the evolution as a function of the charge carrier density. The labelled features correspond to the electron pockets at the L point (p_1), and the remnant bulk-like bands (p_3). (e) Equivalent EDCs at A, highlighting a peak from the inner valence band (p_2).

would develop more 2D character.

The alternative scenario is intercalation, in which the K atoms migrate into the van der Waals gap between layers, leading to an increased van der Waals gap that causes decoupling of the topmost layer both structurally and electronically. This scenario is known to occur almost immediately at room temperature [203] but is also often applied to dosing studies of TMDCs even when the sample is held at low temperatures [208, 85, 186]. This topmost layer also becomes doped due to the donated electrons from the K^+ ions.

The two scenarios lead to somewhat similar effects electronically, since in both cases electron-doped 2D surface-confined states emerge (i.e. wavefunctions localised in the topmost layer of $HfTe_2$). The vertical field scenario is a plausible scenario for our low-dosing data in Fig. 3.14(b). Indeed, the data in Fig. 3.14(b) largely resembles

the bulk band structure, but with an overall energy shift, which could be accounted for by a band-bending potential at the surface. Whereas after further dosing the appearance of the data changes qualitatively (the first point beyond n_e=0.11 el/u.c in our dosing series), especially in the structure and intensity distribution of the bands around -2.5 eV. Moreover, we find very good agreement overall between the shape of the valence bands in Fig. 3.14(c) and the DFT calculations for an isolated monolayer (for the monolayer calculation, we fix the c parameter of the mBJ functional using the bulk value, rather than calculating it during the self-consistent cycle.). This is evidence in favour of the intercalation scenario, as it implies that the topmost layer is structurally decoupled, suppresses out-of-plane hopping, which particularly affects the p_z orbital, leading to the emergence of monolayer-like dispersions of the valence bands. Thus at least for our highest-dosing samples, we are in agreement with Ref. [186] that the intercalation scenario is most likely.

For a more detailed analysis we extract energy distribution curves (EDCs) from the L and A points and track their evolution with K dosing. The feature p_1 in Fig. 3.14(d) shows a shift of $\sim$ 0.22 eV to lower energy, reflecting the filling of the Hf 5d-derived conduction band at L. The inner Te 5p-derived hole pocket in Fig. 3.14(e), p_2, shows qualitatively a similar shift but with a slightly larger magnitude of $\sim$ 0.37 eV. The different behavior of these bands as a function of K deposition at the surface may be related to their different orbital character. Assuming that the shift of p_2 is representative for the hole bands overall, the different magnitude of the shift implies that the band overlap decreases somewhat with dosing. This indicates that a rigid shift model is not applicable in this material. The lineshape of p_2 in Fig. 3.14(e) also becomes noticeably sharper, as the surface confinement takes effect and the state loses any k_z-dependence. However, other features such as p_3 simply lose intensity (though still weakly contributing even at high dosing) and show low or negligible energy shifts with increasing dosing in (Fig. 3.14(d)). These correspond to remnant intensity from bulk states, which we will focus on later.

3.6.2 Tracking the electronic changes by core levels spectroscopy

In addition to the shifts of the Te 5p-derived valence bands, the Te 4d shallow core levels also show a significant change with K dosing (Fig. 3.15(a-e)). Consistent with a single environment for the Te atoms, these appear as a sharp doublet in the pristine case. As we dose the surface with K, however, fitting the data using two Voigt function pairs becomes necessary, reflecting the separate chemical shifts in the surface layer and the bulk. The intensity of the surface contribution (red) relative to the bulk-like (blue) signal increases with increasing dosing, concomitant with their energetic separation increasing also. Fig. 3.15(b) shows that the energetic shift of the Te 4d state has approximately the same tendency with the shifts of the valence bands.

Thus overall, as has been pointed out by [186], this electronic structure may be understood as being close to a doped monolayer of 1T-$HfTe_2$, with the Te 4d levels experiencing a similar shift of the chemical potential to the valence bands, but the Hf states showing a smaller shift.

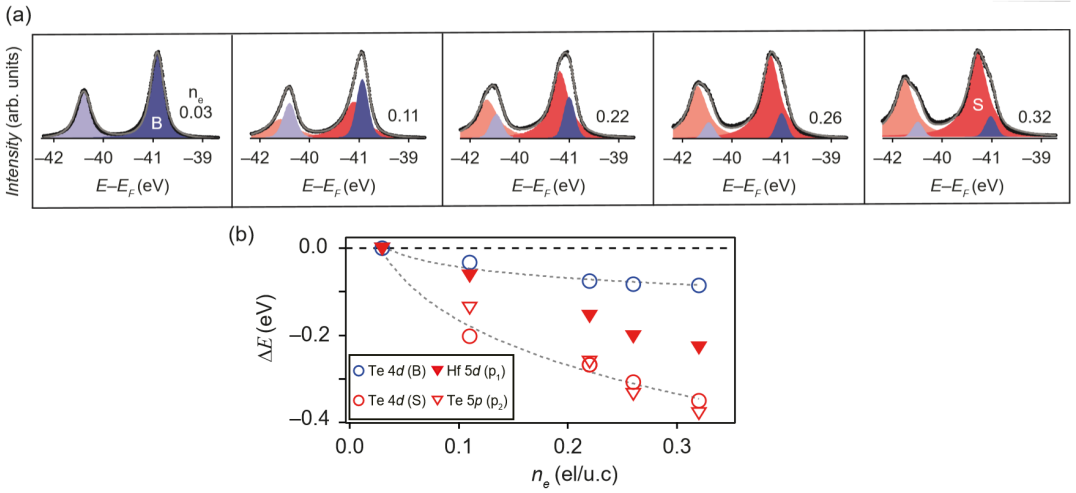

FIGURE 3.15: (a) Core level spectroscopy of Te 4*d* as a function of charge carrier density. The spectra were fitted using two pairs of Voigt functions, depicted as blue (bulk) and red (surface) shaded areas. The SOC peak separation and areal ratio of Te $4d_{3/2}$ to Te $4d_{5/2}$, were fixed to the values obtained from the pristine surface (n_e=0.03). (b) Comparison of the energy shift of shallow core levels of Te 4*d* (blue and red circles), the inner Te 5*p*-derived state of the valence band (p_2, filled red triangles) and the Hf 5*d*-derived electron pockets (p_1, empty red triangles). The data reveals a similar trend of the p_2 valence band state (Te 5*p*) and Te 4*d* shallow core levels.

3.6.3 Photon-energy-dependent ARPES: k_z maps

Figure 3.16(a,b) shows photon-energy-dependent ARPES measurements before and after K deposition on $HfTe_2$, mapped into k_z by employing the standard free-electron final state approximation: $k_z = \frac{1}{\hbar}\sqrt{2m_e(V_0 + E_k \cos^2\theta)}$, where θ is the in-plane emission angle, E_k is the photo-electron kinetic energy and V_0 is the inner potential. We use an inner potential of 11 eV. The k_z map of the pristine surface shows a pair of Te $5p_{xy}$ with the contribution $5p_z$-orbital derived state at the Γ point, and electron pockets centered at each L point (Fig. 3.16(a)). The asymmetry of these pockets reflects the trigonal symmetry of the crystal and the matrix element effects during the photoemission process. Nevertheless, all the states forming the band structure of the pristine surface have a 3D character, as discussed in details above.

Upon alkali metal deposition, we observe the emergence of states without k_z variation, which confirms that the electron pockets in the surface-dosed system are strictly 2D surface-confined states. In addition to these 2D states, there exists a noticeable contribution of 3D bulk states as shown in Fig. 3.16(b). These resemble the 3D electronic structure of the pristine surface, though with some subtle shifts. We interpret these weaker features as photoelectrons being excited deeper in the material and have a non-negligible chance to escape, analogous to the remnant bulk-like contribution to the core level spectra in Fig. 3.15(a). Interestingly, the spectral weight of these remnant 3D states appears to be shifted along the k_z axis (using the same value of the inner potential for the k_z-mapping). In other words, a modified inner potential may be applicable for these photoelectrons. Within the three-step model, the inner potential includes a term from the material work function [135, 136, 22], and this is known to be strongly dependent on K dosing [214]. We speculate therefore that even though the initial states of this bulk-like contribution are essentially unaffected

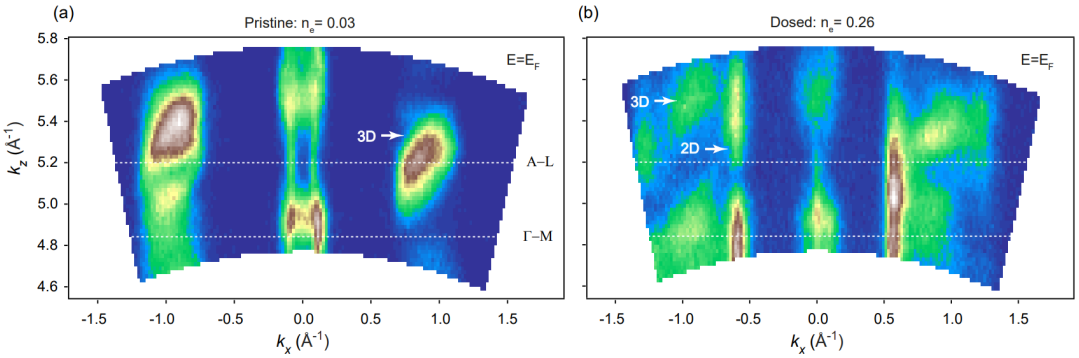

FIGURE 3.16: Photon energy-dependent ARPES. (a)-(b) k_z maps, processed from photon-energy dependent data at E_F before and after Potassium dosing on $HfTe_2$ surface along M-Γ-M′ [L-A-L′] direction, providing clear evidence of the emergence of surface-confined states and the remnant bulk-like contribution due to the non-negligible chance of the deep photoelectrons to escape.

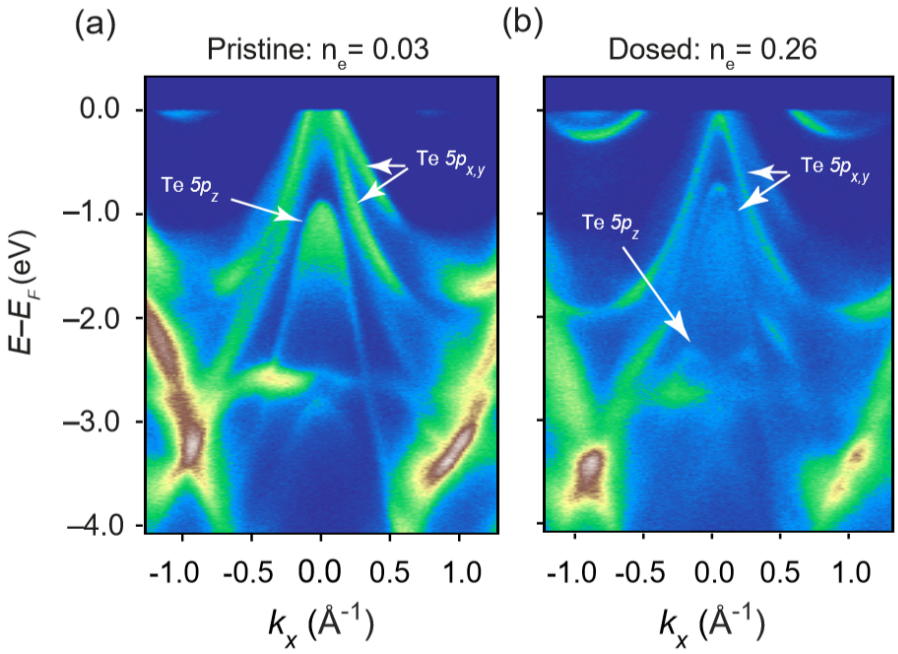

FIGURE 3.17: (a)-(b) Valence band dispersion at a photon energy $h\nu = 87$ eV of the pristine and dosed surface, showing unambiguously the asymmetry disappearance and sharpness of the bands due the monolayer-like electronic structure after dosing. The observed features inside the electron pockets and the center are a clear evidence of the remnant bulk states of deeper photoelectrons in the material.

by the dosing, the photoelectrons experience a different surface potential, and thus come out with a different effective k_z.

In addition to the increased sharpness of the electronic structure, due to their 2D character after dosing, the asymmetry present in bulk spectra disappears in the surface-confined states (Fig. 3.17(a,b)). This occurs because in the 2D limit, the band structure is expected to be sixfold symmetric. However, the weaker, asymmetric, and broader, spectral features come from a remnant contribution of the bulk states.

In particular, our understanding of the spectral weight inside the electron pockets in Fig. 3.17(b) comes from such bulk-like states, as evidenced from their 3D character in the k_z map after dosing (Fig. 3.16(b)). Similar bulk-like features are often observed even after a substantial dosing is applied [215].

3.7 Topological features in the valence band structure of $HfTe_2$

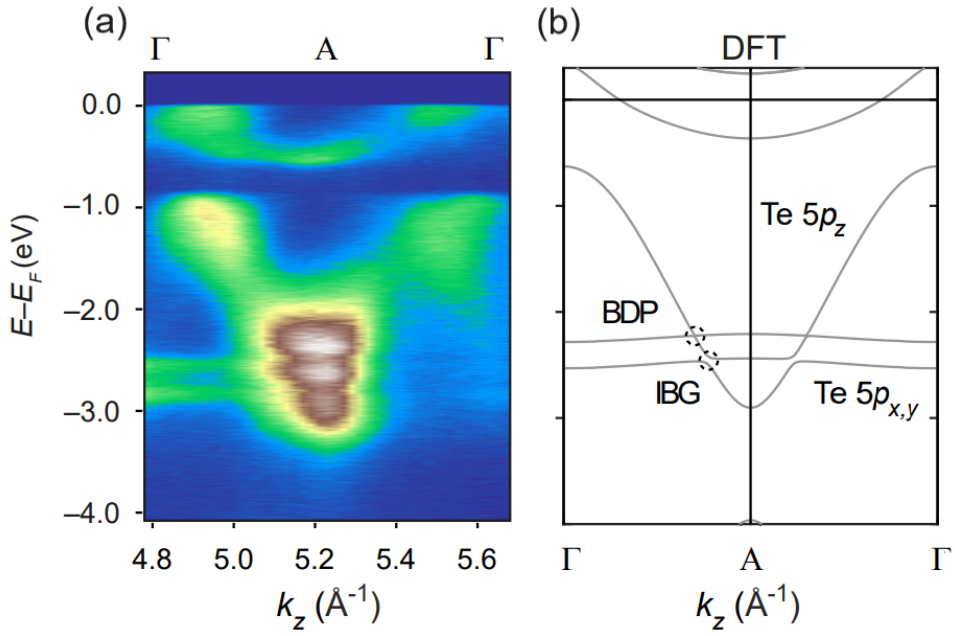

FIGURE 3.18: (a)-(b) Band dispersion along the out-of-plane k_z direction at the Brillouin zone centre [Γ-A direction] of the pristine surface, highlighting the expected crossings of the Te p_z orbital and Te p_{xy} orbital-derived states, giving rise to a bulk Dirac point (BDP) (upper crossing) and an inverted bandgap (IBG) (lower crossing), as labeled in our DFT calculations.

One of the interesting features of the 3D electronic structure is that it supports the existence of the bulk Dirac fermions as well as an inverted bandgap. These topologically-protected features arise from within the manifold of Te p-orbitals [13]. In this layered material, with a trigonal crystal field, p-orbital states form dispersive bands due to bonding, crystal-field splitting and spin-orbit coupling. In the out-of-plane k_z direction, a band with Te p_z orbital character behaves very differently to the in-plane p_{xy}-derived states. This gives a general expectation of a strongly k_z dispersion of the out-of-plane Te p_z orbital and a dispersionless pair of in-plane p_{xy}-derived states, thus naturally causing a set of k_z-dependent crossings [13, 107, 108, 216, 217].

Indeed, our valence band dispersion between Γ ($\mathbf{k}$ = (0,0,0)) and A ($\mathbf{k}$ = (0,0,π/c)) high-symmetry points of the Brillouin zone shows the p-orbital-derived manifold of states along the out-of-plane k_z direction (fig. 3.18(a,b)). The crossing of the p_z orbital-derived state with the upper p_{xy} derived state forms a symmetry-protected 3D Dirac point, due to their belonging to different irreducible representations. However, p_z and the lower p_{xy} derived state share the same symmetry character and angular momentum but opposite parity, their hybridization thus opens an inverted

bandgap which is expected to host topological surface states [13]. The location of these crossings at deeper binding energies E-$E_F \sim 3$ eV, and the small size of the inverted bandgap makes the resolution of such features challenging due to the broadening of the bands.

3.8 Conclusions

In conclusion, our findings show how the electronic structure of the $HfTe_2$ has undergone significant changes upon alkali metal deposition at the surface. The measured ARPES spectra revealed a 3D semimetallic ground state in the pristine sample. The broadening of the bands and asymmetries in the spectral weight were ascribed to the k_z uncertainties in the photoemission process and the crystal structure, respectively. This then evolves into 2D surface-confined states, with correspondingly sharper linewidths and more symmetric intensity. After substantial doping, a monolayer-like electronic structure was revealed, indicating intercalation of the alkali metal and decoupling of the topmost layer of $HfTe_2$. However, we also found evidence of bulk-like features, arising from photoelectrons from deeper in the material, even after substantial K dosing. Furthermore, we show that $HfTe_2$ hosts topological features such as a BDP and an IBG, a further example of the generic mechanism described for other TMDCs in the same space group [13]. Our methodical study of this prototypical layered semimetal gives evidence of the complexity that can occur upon alkali-metal dosing, showing qualitatively different behaviour to recent studies in another semimetal, $PtSe_2$ [33]. Finally, we suggest that tuning the electronic structure of the narrow-band-overlap material $HfTe_2$ could lead to the discovery of novel electronic ground states.

Chapter 4

Fermiology and Electron-Phonon Coupling in the 2H and 3R polytypes of NbS_2

This chapter starts with a brief recall of the instabilities in 2H-NbS_2, raising the question about the peculiarity of this materials among the metallic TMDs family of group V, since it stands out as the only system which hosts superconductivity without a CDW phase. A brief introduction of many-body interactions, and more specifically electron-phonon coupling as the origin of the novel electronic states in TMDs will be given, followed by its important role in driving the superconductivity in 2H-NbS_2. Previous results showing the two gap nature of this compound both theoretically and experimentally will be presented and rigorously described. This literature review will finish by bringing back the phonon dispersion in 2H-NbS_2, evidencing anharmonicity as the key factor in the absence of a CDW phase in this material.

The second part of this chapter consists of the results achieved within this work, where ARPES and DFT calculations were combined to examine the low-energy electronic structure of 2H-NbS_2 and 3R-$Nb_{1+x}S_2$, giving unambiguous insights on the momentum and orbital character dependence of the electron-phonon coupling strength in the 2H phase in one hand, and evidencing the absence of superconductivity in the 3R in the other.

The results presented here have been accepted for publication in Physical Review B (a pre-print of the paper can be found on arXiv, DOI: https://arxiv.org/abs/2012.12595).

4.1 Literature review of superconductivity and "latent" CDW in 2H-NbS_2

2H-NbS_2 is a prototypical system of the TMDs family, which unlike other TMDs in the same group of the periodic table, TaS_2, $TaSe_2$ and notably the isostructural and isovalent $NbSe_2$ [218], does not undergo a charge-density-wave (CDW) phase. However, its ground states still host some novel electronic states, as this system has been evidenced, both theoretically and experimentally (i. e. spectroscopy [122] and thermodynamics [123]) to exhibit two well-defined superconducting gaps below T_c = 6.2 K. The absence of a CDW phase in 2H-NbS_2 is attributed to the anharmonic effects [110, 126, 219]. The low-energy phonons, which put this material on the brink of a CDW phase [110], however, exhibit a strong electron-phonon coupling which is

in turn considered to be the driving factor to the superconductivity in 2H-NbS_2 [126].

4.1.1 Electon-phonon coupling effects in ARPES

Many-body effects play a crucial role in modern condensed matter physics, as they are at the core of several fascinating phenomena. One of the most interesting effect among this family is the electron-phonon interaction (EPI), which as demonstrated in Fig. 4.1, takes place as a result of electron scattering from an initial electron state with momentum **k** to a final electron state by a phonon with momentum **q** through phonon emission and phonon absorbtion [220].

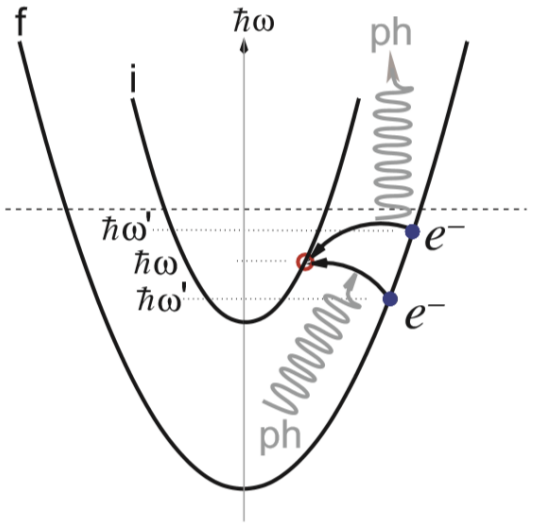

FIGURE 4.1: Phonon-mediated interband scattering from an initial electron state (i) (blue filled circle) with momentum k to a final electron state (f) (red empty circle) by phonon emission and phonon absorption [220].

By standing out as a major factor in several properties that are found in complex materials such as electrical resistivity, heat capacity and BCS-type superconductivity, the electron-phonon coupling is a fundamental many-body interaction that decreases the lifetime of excited electrons or holes, and information about its strength can be thoroughly investigated by both theoretical and experimental approaches. Tunneling spectroscopy and heat capacity measurements have always been unitized to gain insights about the electron-phonon coupling in materials. However, modern ARPES has allowed the investigation of many-body effects and el-ph interaction in particular in unprecedented details, since it unambiguously gives the energy and momentum k dependence of the interaction, thus providing a detailed study rather than averaging the e-ph strength over the whole Fermi surface of metals, as it is the case for the previous techniques [220].

As depicted in Fig. 4.2, within a typical phonon energy range $2\hbar\omega_D$ at the vicinity of the Fermi level, the electron-phonon coupling renormalises the band dispersion in a way that it is flatter at E_F, resulting in an significant increase of the density of states (DOS) and effective mass of the electrons at E_F. This increase can be expressed as follow:

$$m* = m_0(1+\lambda), \tag{4.1}$$

where λ is the electron-phonon strength parameter, whereas $m*$ and m are the effective masses with and without e–ph interaction, respectively [220].

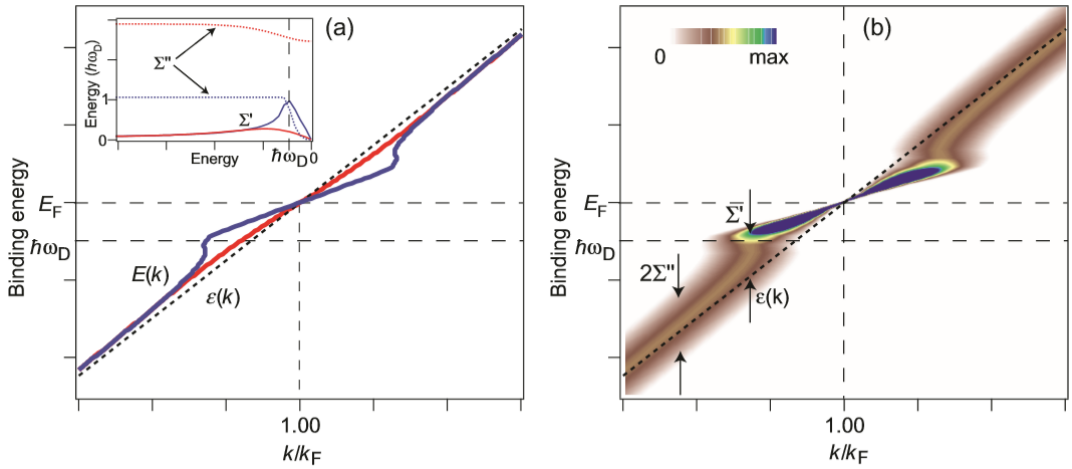

FIGURE 4.2: (a) Renormalization of the electronic dispersion at the Fermi vicinity. The dashed line is the bare dispersion $\epsilon(k)$, while the solid line is the renormalized dispersion $E(k)$ for a low temperature (blue) and a higher temperature (red). Inset: real and imaginary parts of the complex self-energy for the e–ph coupling, Σ' and Σ'' for a low temperature (blue) and a higher temperature(red). (b) Spectral function $A(\mathbf{k}, \omega, T)$ at a low temperature showing the sharpening of the quasi-particle peak near E_F. The arrows indicate how Σ' and Σ'' correspond to the renormalization of the dispersion and the finite width of the peak, respectively. The inset bar gives the color scale [220].

In ARPES, information about the electron-phonon coupling can be directly obtained from the spectral function $A(\mathbf{k}, \omega, T)$ through the complex self-energy Σ, where its real Σ' and imaginary Σ'' part indicate the effect of the e–ph coupling on the dispersion (i. e. band renormalization) and quasiparticle lifetime τ respectively. This lifetime τ, the inverse lifetime Γ or the imaginary part of the self energy itself Σ'', which are in fact the same quantity simply describe the decay of the excited electrons or holes.

Both the real and imaginary part of the self-energy, Σ' and Σ'' respectively, are related by a Kramers-Kronig transformation, implying that the determination of either of them is sufficient. The inset of Fig. 4.2(a) shows the typical results for Σ' and Σ'' at a low (blue) and a higher temperature (red). Σ' is very small except at the vicinity of the Fermi level, but vanishes exactly at E_F. Σ'' in contrast, is constant at high binding energies but promptly decreases close to the Fermi level and only vanishes at E_F for $T = 0$ [220].

4.1.2 Electron-phonon coupling and other contributions to the linewidth broadening in ARPES

Although we are merely considering the electron-phonon coupling here, the simultaneous presence of other many-body effects such as electron-electron (e-e) and defects (df) interactions in the material, which leads to other scattering events and contribute to the total function of the inverse lifetime as follows [220]:

$$\Gamma = \hbar/\tau = \Gamma_{df} + \Gamma_{e-e} + \Gamma_{e-ph} \tag{4.2}$$

Γ_{df} represents the elastic scattering events that are caused by defects in the sample and that limit the mean-free path of a carrier. This component enters as a pure offset to the total inverse lifetime Γ since it is generally not strongly energy or temperature dependent. The number of defects, on the contrary, is temperature dependent as these can be thermally excited at higher temperatures resulting in the increase of Γ_{df} [220].

On the other hand, Γ_{e-e} reflects the inelastic electron-electron scattering, which is energy-dependent, as it increases for higher binding energies because the phase space for inelastic e–e scattering is extended. The temperature dependence of Γ_{e-e}, however, is very weak [220].

At very low temperatures, high excitation energies and in the absence of defects, the most relevant limiting factor to the excitation lifetime is the e-e scattering. However, at high temperatures and close to the Fermi level, Γ_{e-ph} becomes the dominant parameter as it increases because of the increased phonon excitations probability. Therefore, Γ_{e-ph} is the only contribution to the total total inverse lifetime Γ which has a significant temperature dependence in Eq. 4.2, allowing thus the isolation of the electron-phonon coupling from the other contributions experimentally [220].

4.1.3 Superconductivity driven by k-dependent strong electron-phonon coupling in 2H-NbS_2

Although isostructural and isoelectronic to the well-known 2H-$NbSe_2$, which exhibits a $\sim 3 \times 3$ CDW and also superconducts at 7.2 K [121], 2H-NbS_2 sticks out as an exception in the metallic (V,Nb,Ta)(S,Se,Te)$_2$ family of TMDs. It is the only system which doesn't undergo a CDW phase. However, Scanning tunneling spectroscopy (STS) [122], specific heat measurements [123], in-plane magnetic penetration depth [124] and pressure dependence measurements [125] have all evidenced the presence of two superconducting gaps below T_c = 5.7 K in this component, similar to the isovalent 2H-$NbSe_2$.

Multi-gap superconductivity is a very fascinating phenomenon in condensed matter physics, and one of the rare examples of a *multi-gap* superconductor is MgB_2, a material in which the superconducting properties were discovered in 2001 with a relatively high T_c of 39K [221], and subsequently established as a conventional superconductor, where the pairing mechanism is mediated by the electron-phonon interaction [222]. However, early experiments indicated that MgB_2 might have two distinct superconducting energy gaps [223, 224, 225, 226, 227, 228], whereby the Fermi surfaces of different orbital character couple to different phonon modes with

different strengths.

Yet the two-gap scenario is not quite the full story, tunnelling spectroscopy measurements of the superconducting gap showed that not only are there two distinct gaps in MgB_2, but that there is a distribution of gaps on each Fermi surface [229], confirming the theoretical predictions [230, 231, 232, 233, 234]. This distribution of gaps is directly explained by the anisotropy of the electron-phonon coupling around the Fermi surface [235]. Similar phenomenology can be expected in other systems where there are multiple Fermi surface sheets of different origins, and NbS_2 is such a case, albeit with a much lower T_c of ∼6.2 K [122].

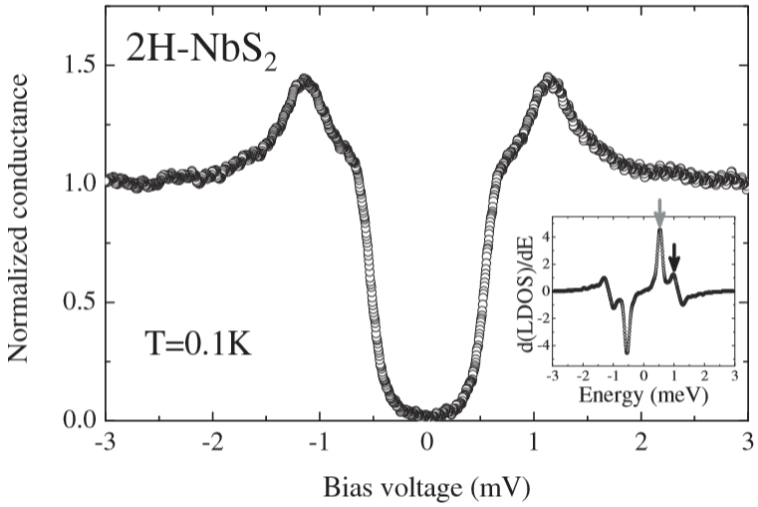

FIGURE 4.3: Characteristic tunneling conductance curve measured at T = 0.1 K (conductance: σ = 1.6 μS at 4 mV). The derivative of the associated local superconducting density of states (LDOS), shown in the inset presents two peaks, at 0.97 and 0.53 meV, marked by black and gray arrows, respectively, which correspond to two peaks in a gap distribution [122].

Fig. 4.3 shows the tunneling conductance measurements as a fucntion of the bias voltage at T = 0.1 K of 2H-NbS_2, performed by Guillamon *et* al., highlighting the distribution of the superconducting gap, which reveals two principal values $\Delta_1 = 1k_BT_c$ = 0.53 meV (grey arrow) and $\Delta_2 = 1.8k_BT_c$ = 0.98 meV (black arrow), as obtained from the peaks in the derivative of the local superconducting density of states (d(LDOS)/dE) in the inset.

While the features observed in the tunneling conductance disappear, the ones in the LDOS are scaled to lower energies close to T_c, as can be seen in Fig. 4.4(a), which shows a smooth temperature dependence of both σ and LDOS. Furthermore, in Fig. 4.4(b), the temperature dependence of the two peaks in d(LDOS)/dE is shown, where the two peaks are located above (0.97 meV) and below (0.53 meV) the value for the superconducting gap expected within the single band *s*-wave BCS model ($\Delta_{BCS} = 1.76k_BT_c$ = 0.87 meV, solid black line), respectively, and both disappear at T_c = 5.7 K, in a very close similarity to the two-gap nature in 2H-$NbSe_2$ [122]. Supporting evidence for two-gap superconductivity in 2H-NbS_2 from Andreev reflections [236] and heat capacity measurements [123] have been as well reported.

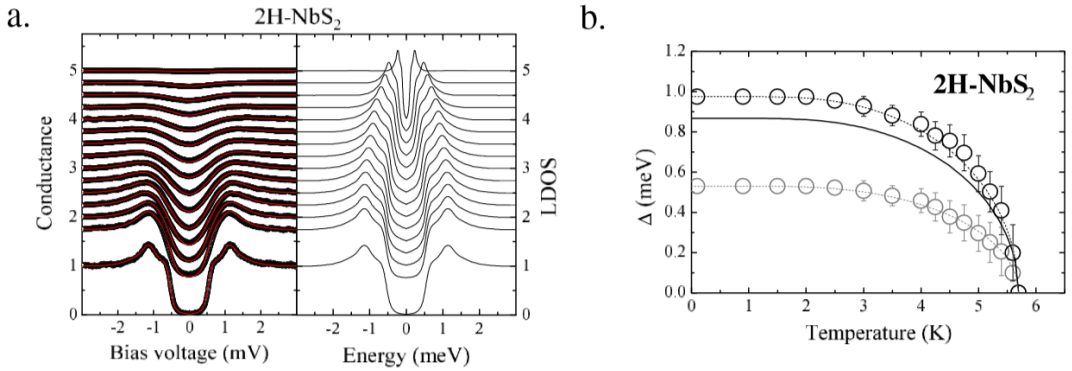

FIGURE 4.4: (a) Temperature dependence of tunneling conductance spectra (σ = 0.65 μS at 4 mV) and superconducting LDOS (right). The data are, from bottom to top, taken at 0.1, 0.9, 1.5, 2, 2.5, 3, 3.5, 4, 4.25, 4.5, 4.75, 5, 5.2, 5.4, and 5.6 K, respectively. (b) Temperature dependence of the two peaks in d(LDOS)/dE (gray and black points, corresponding to the features marked by gray and black arrows in Fig. 4.3; The solid line is the BCS expression taking $\Delta = 1.76 k_B T_c$ = 0.87 meV, with T_c = 5.7 K [122].

In metallic systems where superconductivity usually coexists with a charge density wave (CDW), CDW occurs at a certain T_{CDW} and reduces a considerable part of the density of states but it is the superconductivity, occurring at a lower T_c which fully gaps the Fermi surface, as it is the case in $NbSe_2$ [121]. However, the presence of superconductivity and peculiar absence of CDW in 2H-NbS_2 raises intriguing questions whether these two novel states cooperate or compete in these compounds [126].

Heil *et al*. used the fully anisotropic *ab initio* Migdal-Eliashberg theory including electron-phonon and electron-electron interactions to elucidate the origin of the superconductivity and latent CDW in 2H-NbS_2, and demonstrated that the superconducting pairing is associated with regions in the Fermi surface exhibiting a strong electron-phonon coupling. This interaction is predominately driven by low-energy anharmonic phonons, which in turn place the system on the brink of a charge density wave instability [126], as will be explained later. These phonon anharmonicity is responsible for lowering the T_{CDW} in other TMDs.

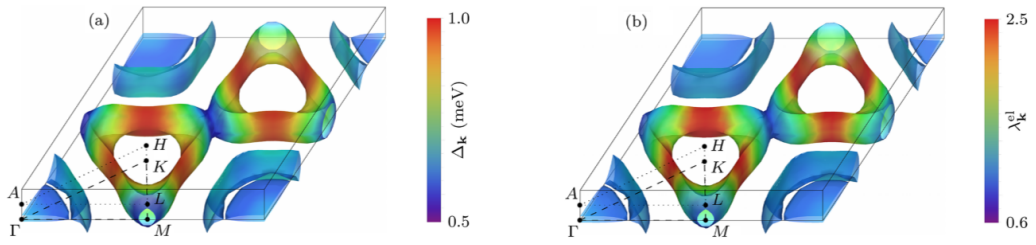

FIGURE 4.5: Momentum-resolved superconducting gap Δ_k (a) and electron-phonon interaction (EPI) strength λ_k^{el} (b) on the Fermi surface, calculated within the *ab initio* Migdal-Eliashberg theory for T = 1.7 K. [126].

Fig. 4.5 depicts the calculated momentum-resolved superconducting gap Δ_k (Fig. 4.5(a)) and electron-phonon interaction (EPI) strength λ_k^{el} (Fig. 4.5(b)) on the Fermi

surface of 2H-NbS_2 calculated at T = 1.7 K. The first glance shows that the Fermi surface is fully gapped below T_c (Fig. 4.5(a)), with the Brillouin zone center exhibiting substantially lower gap value ($\sim$ 0.57 meV) compared to the straight sections of the triangle-shaped pockets around the K point ($\sim$ 1 meV). These regions of the Fermi surface with the largest superconducting gap Δ_k coincide with the "hot spots" of the electronic electron-phonon coupling parameter λ_k^{el}, as highlighted in Fig. 4.5(b). In analogy to the superconducting gaps values, the electron-phonon interaction is much stronger in the straight sections of the K barrel ($\sim \lambda_k^{el} = 2.5$) compared to the Γ pockets ($\sim \lambda_k^{el} = 0.8$) [126].

Taken together, this shows that the full consideration of electron-phonon coupling, rather than a simplistic picture based on nesting is necessary to understand the superconductivity and proximity of a CDW phase in 2H-NbS_2. Furthermore, by recalling the orbital character of the bands forming the Fermi surface (Fig. 4.9(a)), it is apparent that low values of the superconducting gaps/EPI are found on those regions of the Fermi surface with out-of-plane orbital character (S $3p_z$ and Nb $4d_{3z^2-r^2}$), while large values correspond to regions with in-plane character (Nb $4d_{x^2-y^2,xy}$), predicting that the electron-phonon coupling, and consequently the superconductivity is strongly dependent of the orbital character of the bands in 2H-NbS_2 [126].

4.1.4 Supression of the charge density wave in 2H-NbS_2 by anharmonic effects

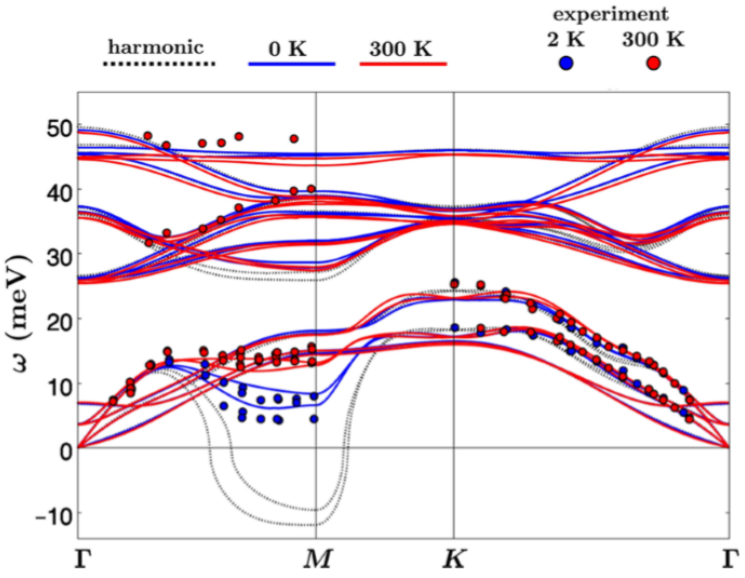

FIGURE 4.6: Harmonic (black dashed lines) and anharmonic phonon dispersion, performed from the stochastic self-consistent harmonic approximation (SSCHA) at 300 K (red solid lines) and 0 K (blue solid lines) using the experimental lattice parameters. The results are compared with the inelastic X-ray scattering (IXS) measurements of Ref. [110] performed at 300 K (red dots) and 2 K (blue dots). The SSCHA dispersion corrects the errors of the pure harmonic result near M: the instability of the two longitudinal acoustic and optical modes is removed and the softening on lowering temperature is well reproduced [219].

From the analysis performed by Heil *et al*., it was clear that the two low-energy anharmonic phonon contribute significantly to creating a *k*-dependent electron-phonon hot spots, which in succession leads to the larest superconducting gaps on the straight sections of the triangular pockets of the Fermi surface around the K points [126]. These anharmonic modes, however, are the ones which place this system on the verge of a charge density wave instability [110, 219].

In Fig. 4.6, harmonic (black dashed lines) and anharmonic phonon dispersion for bulk 2H-NbS_2 is shown, performed by Bianco *et al*. within the frame of first principles calculations at 300 K (red solid lines) and 0 K (blue solid lines) using the experimental lattice parameters. As seen, The phonon dispersion is almost everywhere well reproduced with the harmonic calculation, except close to the M point, where it predicts that two longitudinal acoustic and optical modes become imaginary, whereas the experimental phonon energies show a sizeable temperature dependence in this region of the Brillouin zone (BZ) but stay real all the time. However, quantum anharmonic effects remove the instability found in the harmonic dispersion approach and give a very good agreement to the experimental results at both temperatures, measured by Leroux *et al*. [110] using IXS. From pressure-dependence calculations, these quantum anharmonic effects were found to persist even at high pressures [219].

Therefore, as temperature decreases, electron-phonon coupling causes the softening of two acoustic and optical longitudinal modes close to both M and L points, but no lattice instability takes place due to anharmonic effects. Thus, the anharmonic effects strongly affect the quantum fluctuations in stabilizing 2H-NbS_2, confirming their major importance to describe experimental data and the absence of a CDW instability in this system [110, 219].

4.1.5 Fragile CDW in the monolayer limit of NbS_2

In the monolayer limit, contradictory results about the CDW ordering have been reported. While no CDW phase was observed on a Au(111) supported single layer [237], 1H-NbS_2 samples grown on top of 6H-SiC(0001) has been evidenced to undergo a 3×3 CDW instability [238]. To gain clear insights about the dimensionality and environmental conditions effects (substrate, doping) on the CDW on monolayer NbS_2, Bianco *et al*. used a similar calculation approach and performed the harmonic and anharmonic phonon dispersion for 1H-NbS_2.

In Fig. 4.7(a), the temperature dependence of the harmonic and anharmonic phonon dispersions of free-standing 1H-NbS_2 is shown, calculated using the experimental lattice parameters of the bulk counterpart a_{exp}^{2H}. Although the resulting dispersions are closely similar to the bulk, since at the harmonic level the system hosts a CDW phase, which is eventually suppressed by anharmonic potential down to T = 0 K, the frequency of the phonon softening is 20% harder in the bulk than in the single layer, demonstrating the substantial enhancement of the tendency toward a CDW phase in the 2D limit [219].

When using the theoretical lattice parameters of the monolayer a_{th}^{1H} (Fig. 4.7(b)), the phonon dispersion at T = 0 K now reveals an instability at q_{CDW} = 0.72 ΓM, even when the quantum anharmonic effects are included. At hamonic level, however,

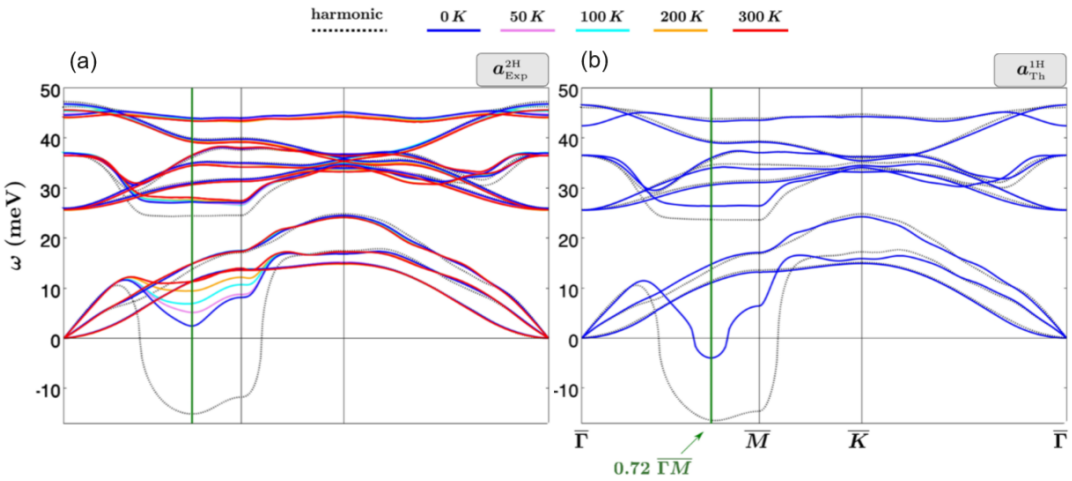

FIGURE 4.7: Suspended 1H-NbS_2 harmonic phonon dispersion (black dashed lines) and SSCHA anharmonic phonon dispersion at several temperatures (colored solid lines), at zero pressure. (a) results obtained with the experimental in-plane bulk lattice parameter a_{exp}^{2H}. The softening of the acoustic mode, localized at q_{CDW} = 0.72 $\Gamma\bar{M}$, is more pronounced than in the 2H bulk case. However, the frequencies remain real even at 0 K. (b) results obtained with the theoretical lattice parameter a_{th}^{1H}, obtained by fully relaxing the structure taking into account quantum anharmonic effecta. At 0 K, the frequency at q_{CDW} = 0.72 $\Gamma\bar{M}$ becomes imaginary [219].

the phonon dispersion is resembling the one calculated with the experimental lattice parameters a_{exp}^{2H}. The emergence of a 3 × 3 CDW phase in single layer NbS_2 is in agreement with the CDW observed for 1H-NbS_2 on the 6H-SiC(0001) substrate, measured by Lin *et al*. [238]. The resulting lattice instability however, is very fragile as the obtained imaginary phonon frequency is very small, and strains as slight as 0.5% are sufficient to put the system away of a CDW.

All together, the achieved findings establish quantum anharmonicity as a key interaction in stabilizing the crystal lattice in bulk 2H-NbS_2, by preventing the complete softening of the phonons, and thus removing the charge density wave found at the harmonic approach [110]. In the 2D limit, however, 1H-NbS_2 hosts a CDW even in the presence of anharmonic modes, but this lattice instability is very weak, suggesting a strong dependence of the CDW on the environmental conditions (substrate, charge transfer, etc), and thus giving an explanation that charge doping from the substrate could be at the origin of the CDW suppression for supported Au(111) samples [219].

4.1.6 Existing ARPES reports on NbS_2

Although of utmost importance, the electronic structure of 2H-NbS_2 has not been fully investigated yet, since most studies were either limited by the data quality [239], performed on Cr, Mn, Ni or Cu doped 2H-NbS_2 [240, 120, 241, 239] or consisted of epitaxially grown single layers [242, 243, 238, 244, 237, 219]. Hence, a systematic study of the electronic structure of 2H-NbS_2 is extremely required, as it can

give significant insights on the mechanisms leading to the peculiar absence and presence of CDW and SC, respectively.

On the other hand, 3R-NbS_2 has received less attention compared to its 2H counterpart. This is mainly due to its relatively deficient electronic properties, embodied in absence of any novel electronic states in this phase. However, unlike 2H and 1T TMDs which both possesses inversion symmetry within their unit cell, the non-symmetric crystal line structure of the 3R leads to a valley-dependent spin polarised states within their bulk electronic structure, making them a firm basis for spintronics and valleytronics applications [43, 245].

4.2 ARPES results

In this work, the photon energy was varied between 30 and 240 eV, and linear horizontal (LH, or *p* polarization) and circular polarised lights were used. 2H-NbS_2 and 3R-NbS_2 single crystals were obtained commercially from HQ graphene. The growth method was chemical vapour transport (CVT), and the growth temperatures were above 1000 and 1080 C, respectively. Samples were cleaved in situ and measured at a temperature of T = 6 K. The energy resolution was typically 10 meV. DFT calculations were performed within the Wien2k package [20], accounting for spin-orbit coupling and using the modified Becke-Johnson (mBJ) functional [17].

4.2.1 Crystalline and electronic structure of 2H and 3R-NbS_2

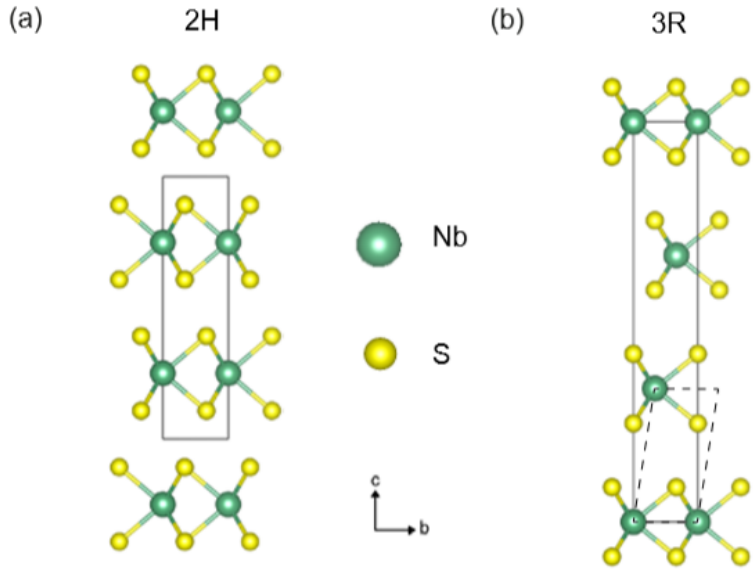

FIGURE 4.8: (a,b) Crystal structures viewed from the side, showing the different stacking modes, with Nb and S atoms are shown in green and yellow, respectively. While the unit cell of the 2H phase contains two monolayers, rotated by 180° between each other to ensure the inversion symmetry in this polytype (a), the primitive unit cell in the 3R contains only one monolayer, resulting in an inversion symmetry breaking in 3R-NbS_2 (b).

In the 2H phase, each layer is rotated by 180° with respect to the layer below it (Fig. 4.8(a)), resulting in a primitive unit cell that contains two formula units. While a single layer of the 2H structure would not possess inversion symmetry due to the trigonal prismatic coordination of the Nb, the stacking creates a centre of inversion symmetry centered between layers (space group 194, $P6_3/mmc$) [40, 41]. Whereas in the 3R phase, there is no rotation between layers but rather each layer is translated by (0,0,a/3) with respect to the layer below. In this case, the conventional unit cell contains three formula units, but the primitive unit cell contains only one formula unit. This stacking structure does not contain any points of inversion (space group 160, $R3m$).

The different stacking arrangements lead to important differences in the electronic structures of the two phases, which we explore with DFT calculations in Fig. 4.9(a, b). On a global scale, there are similarities between the electronic structure of NbS_2 and the well-known MoS_2 and WSe_2 [94, 100, 211, 42, 43, 246, 45], at least as far as the chalcogen orbitals are concerned, which form a manifold of occupied valence bands through bonding and antibonding. However, since Nb has 1 less electrons (d^1 configuration), the states with Nb $4d_{3z^2-r^2}$ and Nb $4d_{x^2-y^2,xy}$ character which would be fully occupied in MoS_2 are only half-filled in NbS_2, ensuring a metallic band structure (Fig. 1.8).

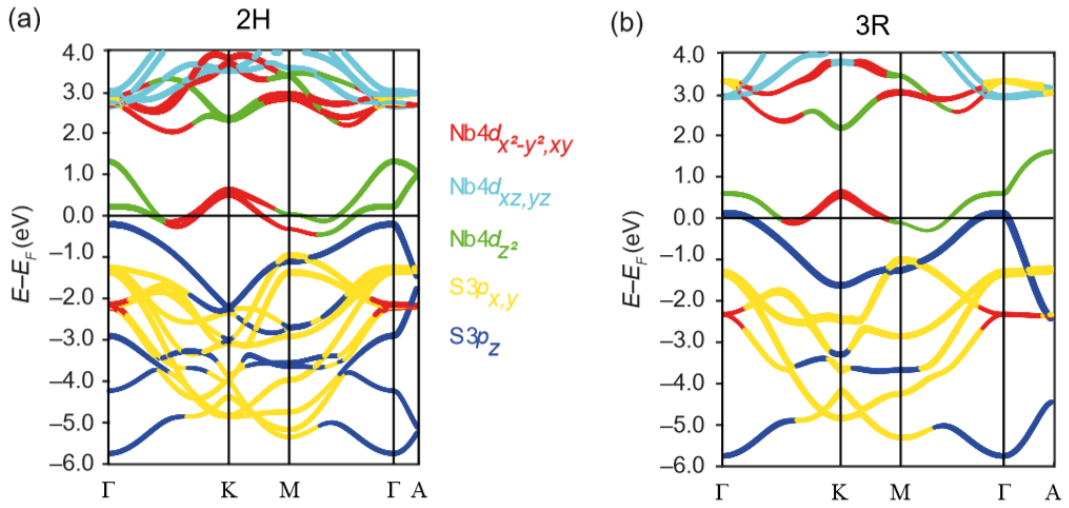

FIGURE 4.9: (a,b) DFT calculations with orbital character projection of the valence and conduction bands for 2H-NbS_2 (a) and 3R-NbS_2 (b).

The first striking difference is that there are twice as many bands in the 2H phase compared to the 3R phase, since there are 2 formula units in the 2H unit cell, giving rise to inequivalent interlayer hopping, whereas in the 3R phase the primitive unit cell contains only one formula unit. This interlayer hopping in the 2H phase depends strongly on the orbital character of the bands; for the in-plane S $3p_{x,y}$ it is a small effect, but notably affects the Nb $4d_{3z^2-r^2}$ orbital-derived bands (Fig. 4.9(a)) much more than other components of the Nb $4d$ (e. g. Nb $4d_{x^2-y^2,xy}$). This has a significant effect for the half-filled manifold of Nb $4d$ states around the Fermi level, as the degree of bilayer splitting varies with the orbital character of the bands, and is thus momentum-dependent, being much larger at Γ than at the K point.

The c^* axis in the 2H phase is also half the length of the 3R phase as can be in the Brilloin zones of both phases (Fig. 4.10), leading to an effective backfolding of bands in the out-of-plane direction (S $3p_z$ orbital derived bands along ΓA direction). Moreover, the different stacking between the two phases does not only affect the electronic structure through the out-of-plane hopping but also the shape of the Brillouin zone. While this has a standard hexagonal shape in the 2H phase, the stacking of the layers in the 3R phase results in a more complex Brillouin zone. For convenience of comparison, however, we use the notation of "K" and "M" also in the 3R phase, even though these are not formal high-symmetry points in this case.

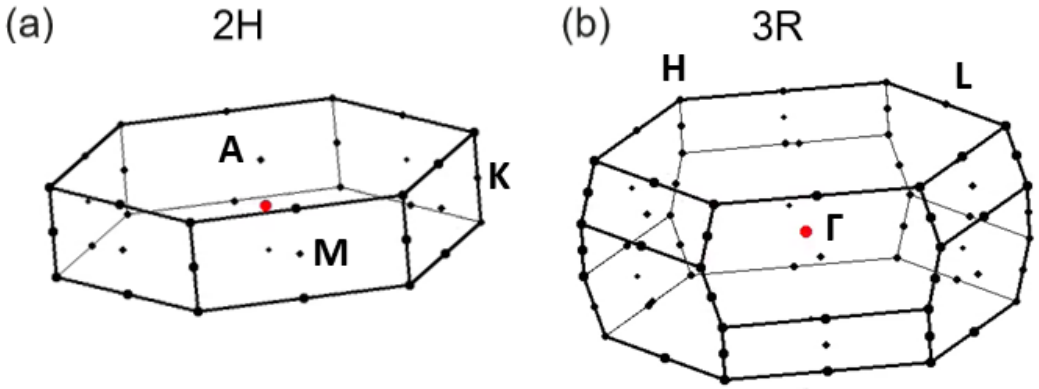

FIGURE 4.10: Brillouin zone of the two phases. While this has a conventional hexagonal shape for 2H-NbS_2 (a), the stacking arrangement results in a warped-like shape in the case of 3R-NbS_2 (b).

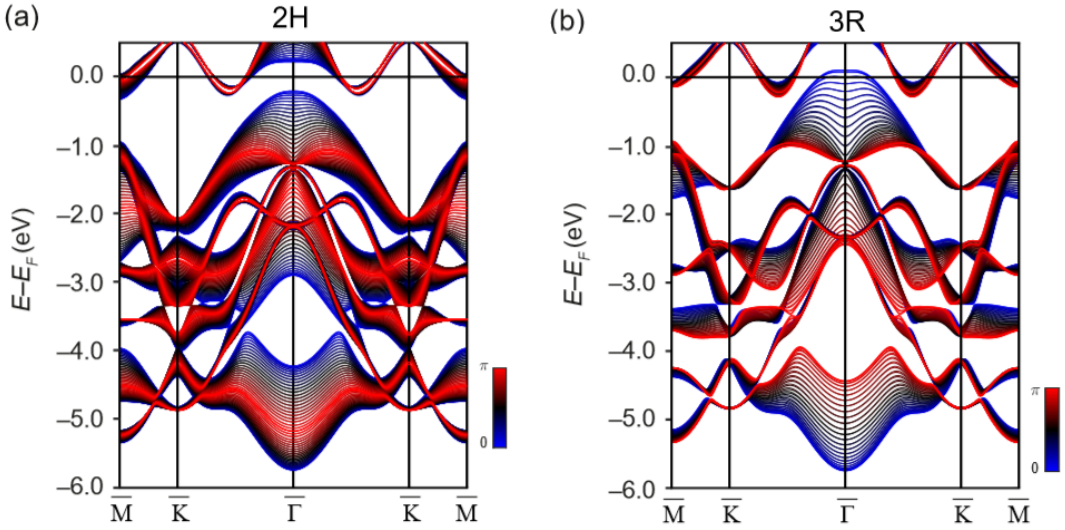

FIGURE 4.11: (a,b) k_z projection of the DFT band structure along the experimentally-relevant M-K-Γ-K-M (L-H-A-H-L) direction for 2H-NbS_2 (a) and 3R-NbS_2 (b), highlighting the 3D and quasi-2D character of the electronic states.

For a more explicit comparison with our ARPES data, in Fig. 4.11(a, b) we show the k_z projection of the DFT band structure along the experimentally-relevant M-K-Γ-K-M (L-H-A-H-L) direction. At a first glance, the k_z projection highlights a dichotomy

in the occupied S valence bands; there are some states which are extremely 3D, derived from the S $3p_z$ orbitals, while others are almost 2D, derived from S $3p_{x,y}$ orbital character. For the Nb $4d$-derived states, there is some k_z dispersion in both the unoccupied states and occupied ones around Γ and M point, respectively. This is because these bands derive from Nb $4d_{3z^2-r^2}$ orbital character. However, around the K point, the electronic states are derived from Nb $4d_{x^2-y^2,xy}$, making them k_z-independent.

This dimensionality difference is clearly seen in our measured ARPES spectra, especially for the 2H phase in Fig. 4.12(a) and Fig. 4.13(a), measured along Γ-K direction at a photon energy $h\nu = 79$ eV and $h\nu = 118$ eV, respectively, where the valence bands closely resemble the k_z-projected calculations, with a superposition of sharp features from quasi-2D states, and broad features from 3D bands that arise due to k_z uncertainties in the photoemission process [143, 140, 145].

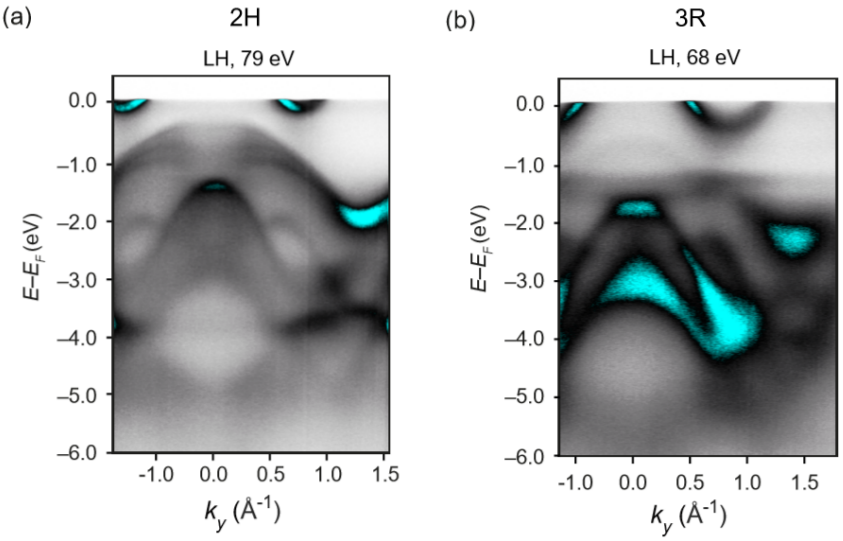

FIGURE 4.12: (a,b) Overview ARPES spectra showing valence band dispersions. Data measured along Γ-K direction at $h\nu = 79$ eV and $h\nu = 68$ eV for 2H-NbS_2 (a) and 3R-NbS_2 (b), respectively, using LH polarised light (p).

However, in the case of the 3R phase, the agreement is not as good. As can be seen in Fig. 4.12(b) and Fig. 4.13(b), measured along Γ-K direction at a photon energy $h\nu = 68$ eV and $h\nu = 120$ eV, respectively, the data quality is lower compared to the 2H phase, where none of the features appear as sharp as in the latter, with a significantly higher background. Secondly, indication of some form of localised impurity-like state in this system as there is evidence for a flat state at E_B = -1.2 eV, not present in the calculations (Fig. 4.12(b)). Additional flat features are clearly seen at higher photon energy data (Fig. 4.13(b)) around E_B = -0.8 eV, as indicated by the black arrow. Finally, the bands at the Fermi level appear to be substantially more occupied than in the calculation, suggesting some form of intrinsic doping in the 3R phase. Therefore, the experimental electronic structure of the two phases are much more different than the DFT calculations would predict, giving strong hints about further important factors rather than the stacking arrangements as the only difference between the two phases.

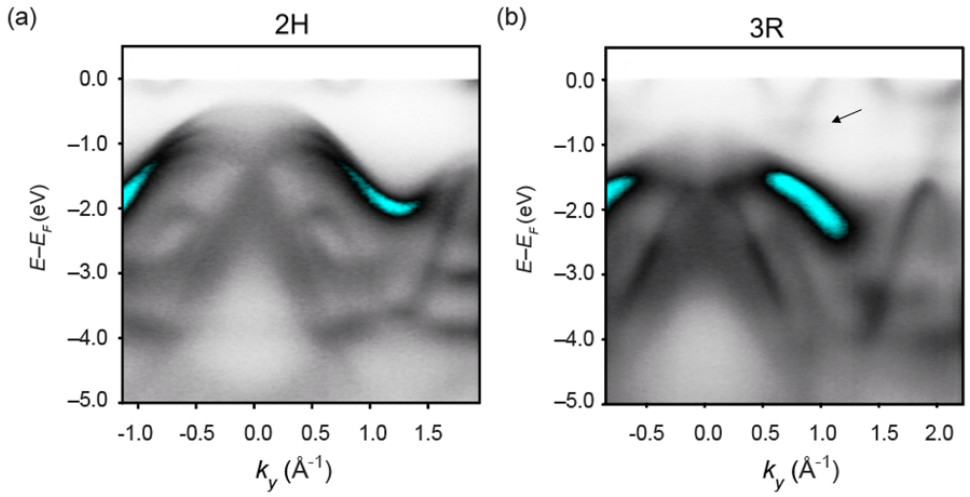

FIGURE 4.13: (a,b) Overview ARPES spectra showing valence band dispersions. Data measured along Γ-K direction at $h\nu = 118$ eV and $h\nu = 120$ eV for 2H-NbS_2 (a) and 3R-NbS_2 (b), respectively, using LH polarised light (p).

4.2.2 Fermiology of 2H and 3R-NbS_2

In order to understand the difference between the two phases and disentangle its driving factors, we perform a detailed investigation of the Fermi surfaces of the two materials. In Fig. 4.14(a,b) we show the calculated 3D Fermi surfaces of both phases, which look broadly similar (except the presence of an additional S $3p_z$ orbital-derived pocket at the Brillouin zone center in the 3R phase), as in both cases cylinders and quasi-2D triangular shaped pockets appear around the Γ and K points, respectively, with the k_z warping of the latter being somehow weaker for the 3R phase, except for the highly 3D S $3p_z$ band that crosses at Γ.

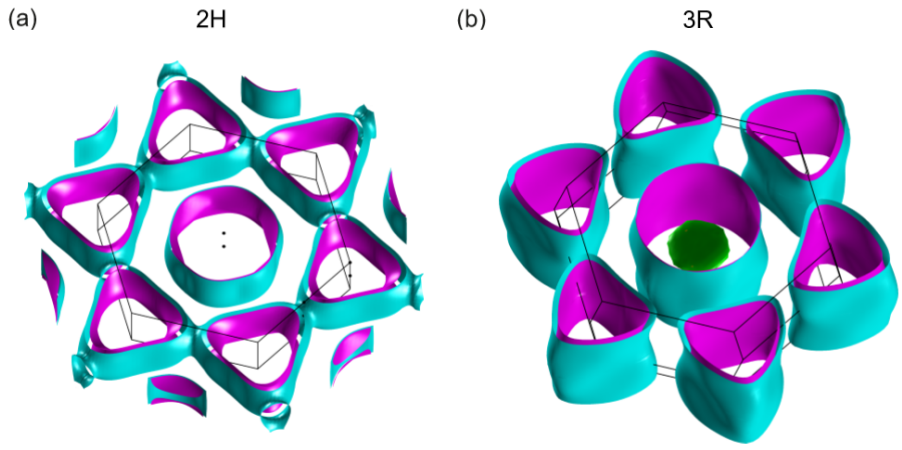

FIGURE 4.14: (a,b) 3D Fermi surface of (a) 2H-NbS_2 and (b) 3R-NbS_2, as calculated by DFT calculations, showing circular and quasi-2D triangular shaped pockets around Γ and K point, respectively for both phases, with an additional S $3p_z$ orbital-derived pocket at the Brillouin zone center in the 3R phase, absent in the 2H counterpart.

Although present in both Fermi surfaces, the band splitting emerges from different origins. While this is due to the interlayer interaction in the 2H phase, which plays

an important role in creating a splitting of inner and outer pockets, the splitting in the 3R phase is a spin-splitting, allowed due to the absence of inversion symmetry in the crystal structure and spin-orbit coupling. A more extended discussion about the basis of the band splitting in each phase, alongside high-resolution ARPES data will be presented later.

In a similar way to the approach considered in the previous chapter to reproduce the asymmetries and k_z broadening in the measured ARPES spectra, the calculation presented in Fig. 4.15(a) shows a simulation of the Fermi surface, obtained by averaging the electronic structure over the entire k_z axis. For instance, while the k_z integration for the typical photon energy range used in ARPES (20-120 eV) can reach 25 or 30% of the Brillouin zone for 1T-TMDs as it is the case in $HfTe_2$ (λ = 5Å) [145], the c^* axis in the 2H phase, however, is only half the length of the 1T phase, leading to a significantly greater k_z integration in the photoemission process, which can reach 80 or 90% of the Brillouin zone size.

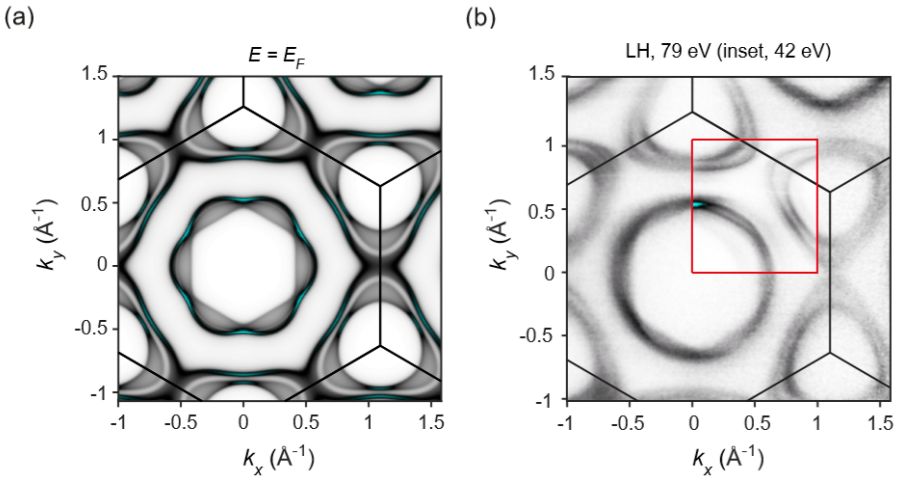

FIGURE 4.15: 2H-NbS_2. (a) Simulated Fermi surface obtained by averaging over the whole Brillouin zone width in the k_z direction for a more straighforward comparison with the data. (b) Fermi surface measured at a photon energy $h\nu = 79$ eV (inset, 42 eV) using LH polarised light.

As depicted in Fig. 4.15, the measured Fermi surface in the 2H phase is quite comparable with the calculation. For the inner pocket, the band splitting is well reproduced, with a mix of sharp and broad states, and a prominent hexagonal warping reflecting the symmetry of the system (space group 194, $P6_3/mmc$). Although the band splitting around the K barrels is well reproduced, there is a notable difference between the data and calculation. Experimentally, the triangular barrels around K form closed pockets (similar to 2H-$NbSe_2$ [247, 248]), however, in our calculation the outer K barrels connect near the M points. We attribute this to a limit to the accuracy of the functional, rather than any off-stoichiometry of the 2H sample. More advanced calculations, e.g. the GW calculations of Ref. [249] find that the K barrels are somewhat reduced in size and no longer touch, while the Γ barrel expands to compensate, giving a better overall match to our data.

In general, there is a very good agreement between the data and calculation, even though the observed electronic structure is highly two-dimensional, somewhat more

so than the calculation (notably the inner triangle around the K barrel), with very little variation observed in the photon energy dependence (Fig. 4.16).

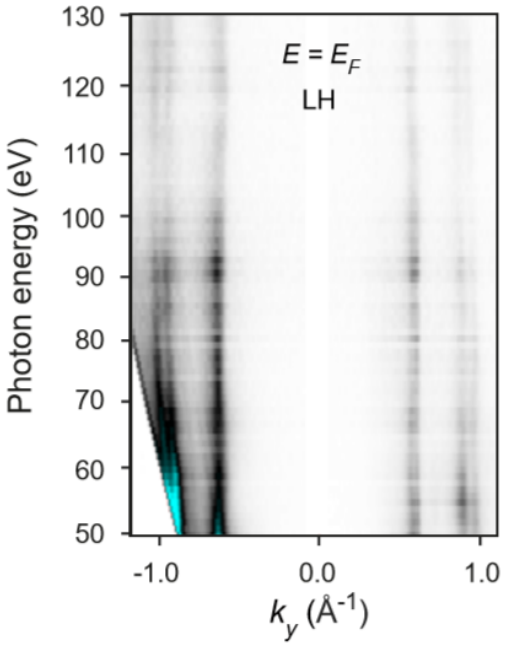

FIGURE 4.16: Photon energy-dependent ARPES of 2H-NbS_2 from 50 to 130 eV, plotting MDCs at E_F along K-Γ-K (H-A-H) direction as a function of photon energy, showing the quasi-2D nature of electronic states with a consistently-resolved splitting of the K barrel bands.

As expected, photon-energy-dependent ARPES of 2H-NbS_2 (Fig. 4.16) shows strictly 2D electronic states spanning along the whole photon energy range, with the larger band-splitting pair derived from Nb $4d_{x^2-y^2,xy}$ orbital only whilst more Nb $4d_{3z^2-r^2}$ orbital weight exists in the inner pair, embodied in their slight broadening.

4.2.3 Evidence of additional Nb interstitials in the 3R phase of NbS_2

Conversely, a stark difference is observed between our measured Fermi surface of 3R-NbS_2 (Fig. 4.18(a)) and the calculated one (Fig. 4.17(a)). The Γ and K barrels of the Fermi surface are found to be both significantly smaller compared to the calculations at the "natural" Fermi level E_F. This is consistent with the increased filling of the valence band in Fig. 4.12(b) and Fig. 4.13(b), and is indicative of a large shift in the chemical potential.

The data more closely resembles the simulation in Fig. 4.17(b) and Fig. 4.18(b), where the Fermi level is set 250 meV above the natural Fermi level of the calculation. This implies a significant amount of extra charge in the system. Fig. 4.19 represents the number of total electrons n in the integrated density of states (DOS) as a function of the energy shift (i.e. rigid shift of E_F). Empirically, it is 12.99 (i.e. 13) for zero shift (at $E = E_F$) but rises for a positive shift of the Fermi level as this results in a more filling of the Nb $4d$ orbitals. A shift of 250 meV corresponds to 0.4828 extra electrons per unit cell.

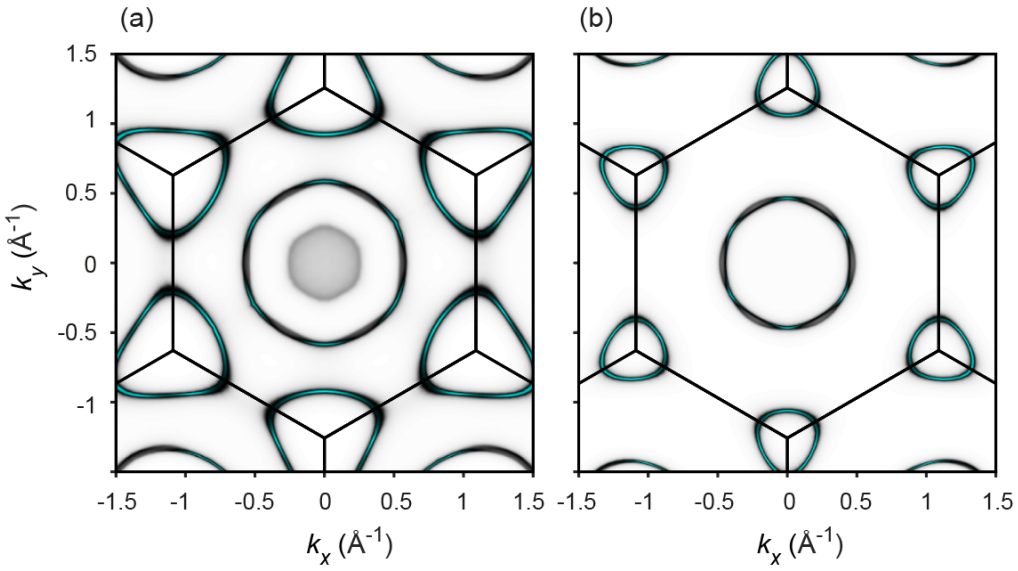

FIGURE 4.17: 3R-NbS_2. (a,b) Simulated Fermi surface obtained by averaging over the whole Brillouin zone width in the k_z direction at E_F (a) and 250 meV above the natural Fermi level (b) to match the data.

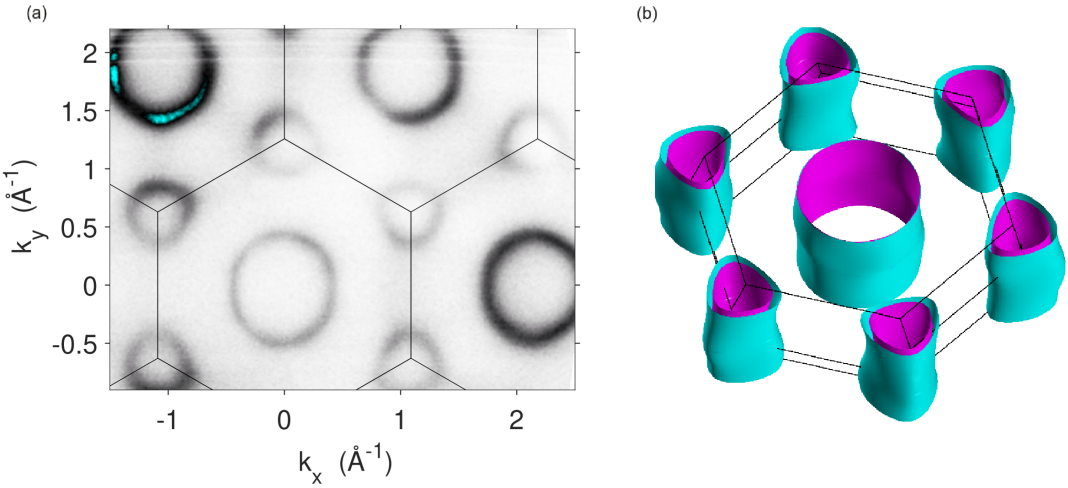

FIGURE 4.18: 3R-NbS_2. (a) Fermi surface measured at a photon energy $h\nu = 120$ eV using LH + CR + CL polarised light. (b) calculated 3D Fermi surface at 250 meV above the Fermi level.

To fully understand this, we take a closer look at the stoichiometry of the two phases, as the experimental data point toward an important role for this, rather than the stacking sequence, in determining the electronic structure differences between the two polytypes. While the 2H phase is reported to exist only as stoichiometric NbS_2, the 3R phase is known to host additional Nb interstitials, resulting in a stoichiometry of the form 3R-$Nb_{(1+x)}S_2$, as depicted in the crystal structure in Fig. 4.20. According to Ref. [68], the range of stability of the 3R phase is within $0.07 < x < 0.18$; consistent with this, Energy-dispersive X-ray spectroscopy (EDX) measurements on our 3R samples indicate $x \approx 0.13$ (EDX measurements provided by HQ graphene).

In reality, as stated in Ref. [250], interstitial atoms are more favoured to be included in the 3R phase due to the relatively longer distance between these extra Nb atoms

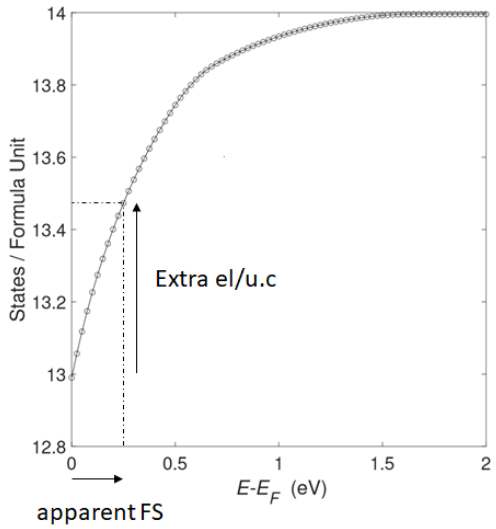

FIGURE 4.19: 3R-$Nb_{1+x}S_2$. Integrated density of states (DOS) giving the number of total electrons n as a function of the energy shift E-E_F.

and the in-plane Nb sites (the existence of such Nb interstitials in the 2H phase would lead to a strong repulsion between the extra Nb atoms and the in-plane Nb sites, due to the shorter distance between them). Thus, the fact that there exist two polytypes at all is intimately related to the stoichiometry.

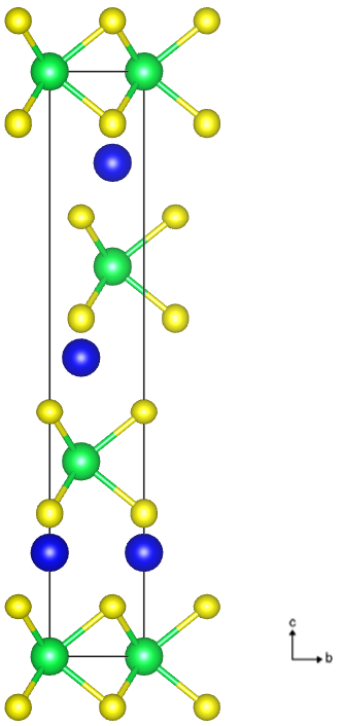

FIGURE 4.20: Crystalline structure of $Nb_{1+x}S_2$, showing the possible additional Nb interstitial atoms in blue, located in the van der Waals gaps of this layered material [250].

These Nb interstitials act as electron donors, giving an increased overall filling of the d shell of the Nb in the main layers. Taking the ratio of the apparent extra electrons

in the Fermi surface to the measured x value, we can estimate that each interstitial Nb donates ~ 3.5 electrons on average. The interstitial sites also act as local impurity potentials, explaining the broadening and extra background in the ARPES data, and consistent with the high density of atomic-scale imperfections observed in STM measurements on 3R-$Nb_{(1+x)}S_2$ [251], compared to measurements on other TMDs.

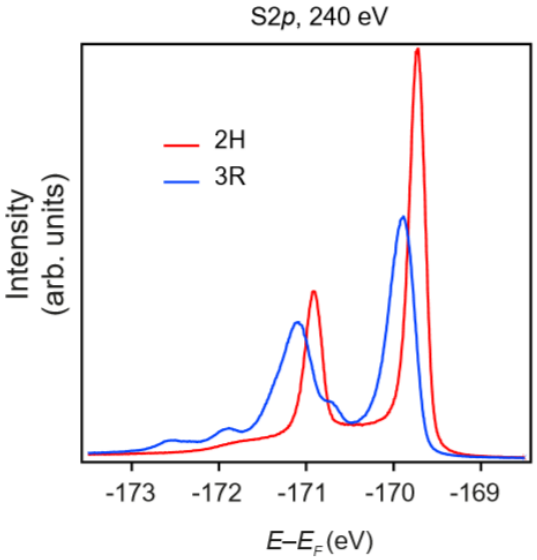

FIGURE 4.21: S $2p$ core levels of 2H-NbS_2 (red) and 3R-NbS_2 (blue) using a photon energy $h\nu = 240$ eV, showing clearly additional satellites in the 3R phase.

The presence of interstitial Nb can also be inferred from the S $2p$ core level spectra in Fig 4.21. In the case of the 2H phase, a sharp doublet is observed, consistent with spin-orbit split $2p_{1/2}$ and $2p_{3/2}$ states from a single chemical site. However, in the 3R phase, there are additional minority peaks, arising from S atoms in a chemical environment with more than the normal 3 nearest-neighbour Nb atoms, due to the interstitial Nb occupancy. The main doublet is also broadened, reflecting electronic inhomegeneity caused by the partial filling of the insterstitial sites. Moreover, the main doublet is shifted by ~ 180 meV, a chemical shift related to the overall chemical potential and average orbital fillings.

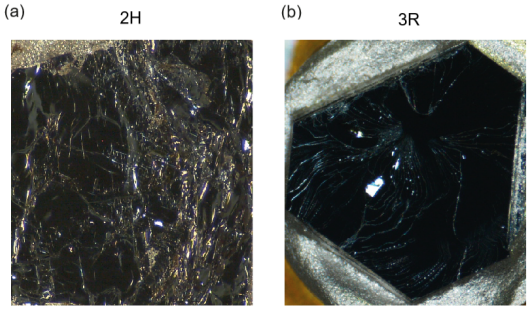

FIGURE 4.22: Microscope images of the single crystals used in this work. While the 2H phase forms thin, flaky samples without clear facets, the 3R samples are beautiful plate-like single crystals with clear crystal facets.

It is worth remarking that the two polytypes also have different physical appearances (Fig. 4.22(a,b)); although both black and metallic-looking, the off-stoichiometric 3R phase forms as beautiful plate-like single crystals with clear crystal facets, while the 2H phase forms thin, flaky samples usually without clear facets. Thus, NbS_2 exemplifies the mantra of not judging by appearances.

4.2.4 Origin of the band splitting in 2H and 3R-NbS_2

The band splitting, although present in both electronic band structures, do not arise from exactly the same origins [40, 41]. While this is due to the inversion symmetry breaking and spin-orbit coupling in the 3R phase, interlayer hopping, emerging from interactions between the layers along the c axis in 2H-NbS_2, results in a larger splitting of the bands in this phase compared to the 3R [43], as illustrated in our DFT calculation of electronic dispersion along ΓK direction of 2H (Fig. 4.23(a)) and 3R-NbS_2 (Fig. 4.24(a)).

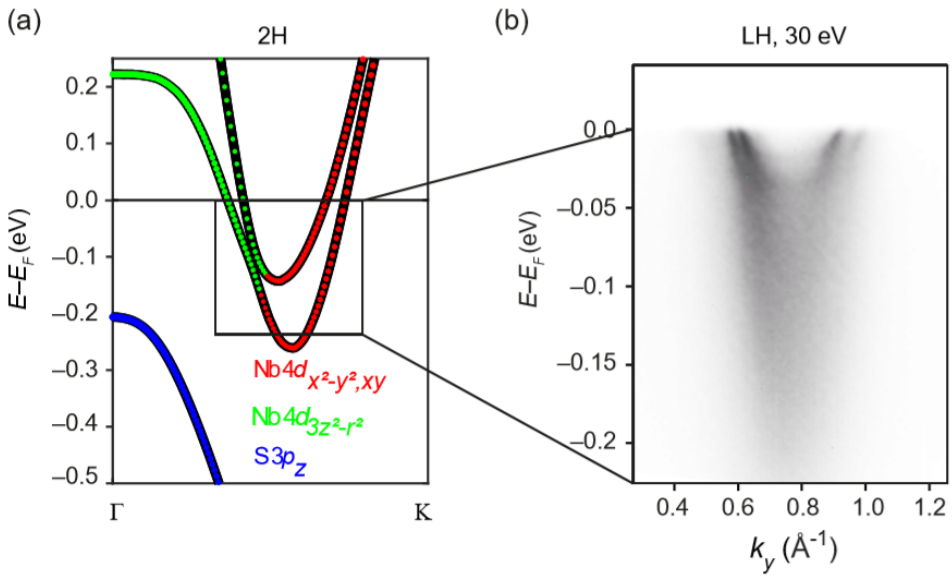

FIGURE 4.23: 2H-NbS_2. Electronic dispersion along Γ-K direction showing the band splitting around K point, as calculated with DFT (a) and measured at a photon energy $h\nu = 30$ eV (b).

As introduced in Chapter. 1, the well-known splitting of the valence band along the ΓK high symmetry direction of monolayer 1H-TMDCs, as discussed in numerous studies of 2H-MoS_2 and WSe_2 [43, 211, 45, 42, 196, 252], is due to strong spin-orbit coupling (because of the high mass of the elements) and lack of inversion symmetry. For the bulk, this splitting is caused by the combination of interlayer interaction and spin-orbit coupling. In this case, there is no spin splitting between these two bands and they are indeed spin-degenerate (Kramers' degeneracy) because of the presence of inversion symmetry along with time reversal symmetry. But the strong spin-orbit coupling in TMDCs results in enhanced splitting of these spin-degenerate bands at the K point of the Brillouin zone [211]. As the interlayer interaction term is a consequence of the layers stacking along the c axis in 2H-NbS_2 and other 2H-TMDs in general, the effect in significantly larger for Nb $4d_{3z^2-r^2}$ compared to Nb $4d_{x^2-y^2,xy}$ orbital derived electronic states, as can be seen in the electronic band structure in

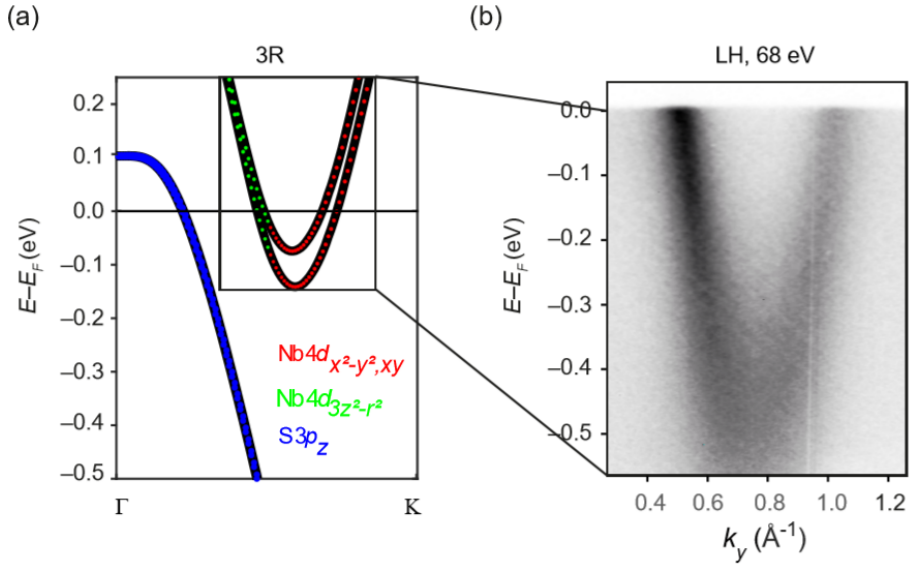

FIGURE 4.24: 3R-NbS_2. Electronic dispersion along Γ-K direction showing the spin-splitting of the bands around K point, as calculated with DFT (a) and measured at a photon energy $h\nu = 68$ eV (b).

Fig. 4.9(a).

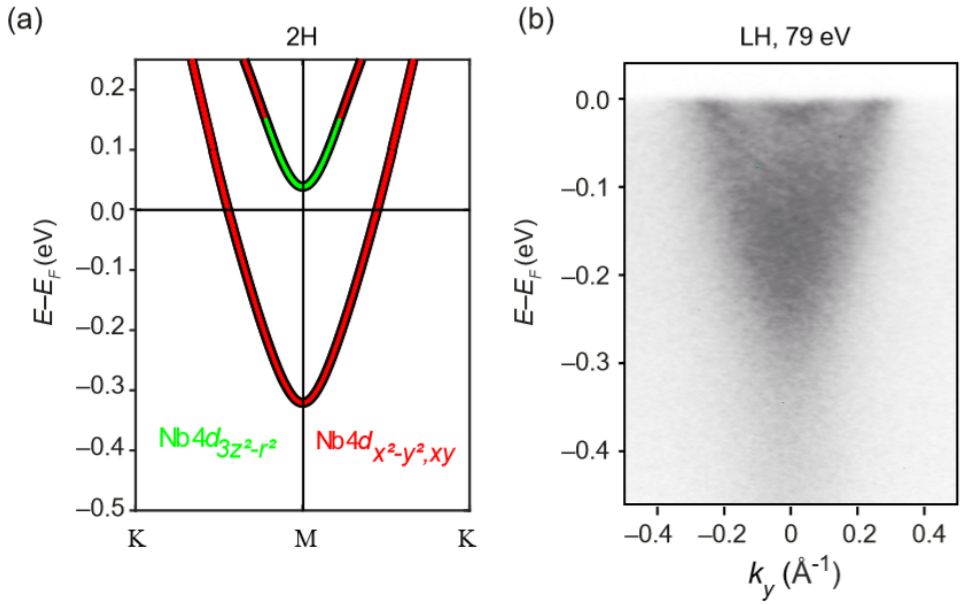

FIGURE 4.25: 2H-NbS_2. Electronic dispersion along K-M-K direction showing the band splitting, as calculated with DFT (a) and measured at a photon energy $h\nu = 79$ eV (b). While the upper band, derived from Nb $4d_{3z^2-r^2}$ orbitals crosses the Fermi level in our data, the DFT suggests that this disperses slightly above E_F, which we attribute to a limitation of the accuracy in the used functional.

The split bands of the 3R polytype however, notably those derived from Nb $4d_{x^2-y^2,xy}$ orbitals, are expected to be spin-polarised states, due to the lack of the inversion symmetry within its crystal structure, with a predominance of the out-of-plane spin component S_z, as a result of the net in-plane dipole at the Nb^{4+} ions due to the

D_{3h} symmetry of the primitive unit cell [40]. The ISB gives rise to a Rashba-type spin-splitting in this phase, as can be seen in the electronic dispersion along KMK direction in Fig. 4.26, with the spin-splitting quenched at the M point as a result of the time-reversal symmetry of the system.

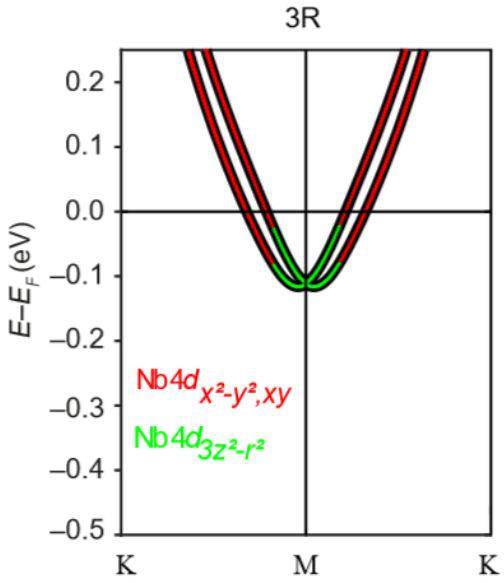

FIGURE 4.26: 3R-NbS_2. DFT calculation of the electronic dispersion along K-M-K direction showing the Rashba-type spin-splitting, allowed by the absence of inversion symmetry in this phase.

Generally, the band-splitting is lower in S compounds compared to their Se or Te counterparts. This is due to both the larger interlayer hopping and notably larger SOC constant in the latter cases as a result of their larger orbital overlap and heavier elements, respectively. For instance, the top-valence band splittings at the K point for MoS_2 and $MoSe_2$ are 0.18 and 0.2 eV respectively, while for WS_2 and WSe_2 they are 0.47 and 0.50 eV, respectively [196].

While the band splitting are nicely resolved in our 2H-NbS_2 data ((Fig. 4.23(b) and Fig. 4.25(b)), the broadening of the bands arising from the interstitial Nb atoms in the 3R phase makes the resolution of such features challenging (Fig. 4.24(b) and Fig. 4.24(b)). These additional Nb atoms are as well responsible for the extra filling of the bands compared to the DFT calculations, resulting in a significantly electron doped electronic band structure, as well described above.

4.2.5 Topology in the band structure of NbS_2

In analogy to all the transition metal dichalcogenides with a trigonal crystal field and spin-orbit coupling like $PdTe_2$, $PtSe_2$, $NiTe_2$, WSe_2, $HfTe_2$, etc [13, 107, 109, 154, 145], the electronic structure of NbS_2 is expected to support the existence topological features such as bulk Dirac fermions as well as inverted bandgaps, arising from within the manifold of S $3p$ orbitals. For instance, S $3p_{x,y}$ orbitals derived bands are dispersionless along the out of plane k_z momentum, while S $3p_z$ derived bands are strongly dispersive along ΓA as a consequence to the out-of-plane hopping of

their orbital character. This naturally causes a set of k_z-dependent crossings along the ΓA direction of the Brillouin zone, giving rise to bulk Dirac points and inverted bandgaps expected to host a ladder of topological surface states.

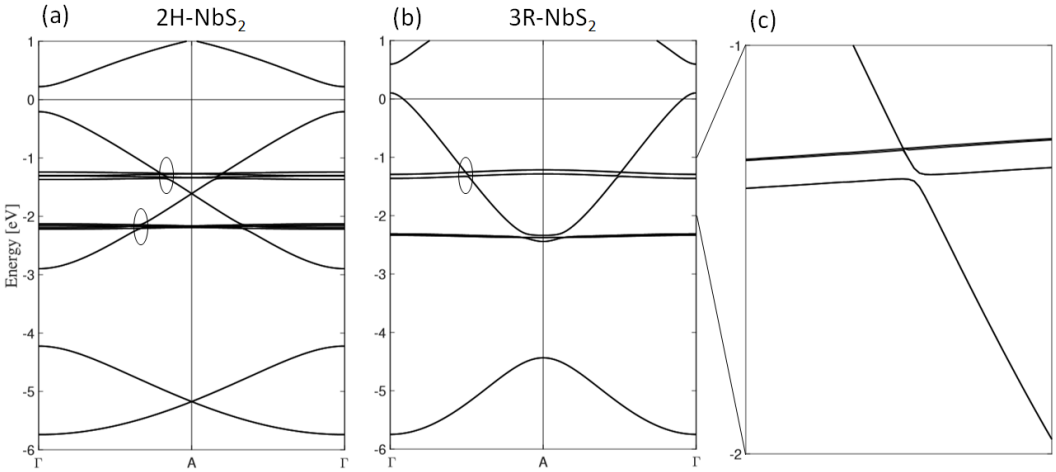

FIGURE 4.27: Electronic band dispersion along Γ-A direction of (a) 3R-NbS_2 and (b,c) 2H-NbS_2, showing the set of bulk dirac points (BDP) and topological surface states (TSS) in the valence band of theses compounds.

As already introduced, the unit cell contains two MX_2 (M=transition metal, X=chalcogen) layers in the 2H structure, as compared to a single such layer in the 3R and 1T structure. This results in an effective backfolding of the bands about the Brillouin zone boundary along k_z, doubling each of the topological features as seen in our DFT calculations along ΓA direction in Fig. 4.27. Yet these topological features are not well separated in energy, which makes their experimental resolution very challenging.

4.2.6 Electron-phonon interaction in 2H-NbS_2

Although neither phase undergoes any structural phase transition, 2H-NbS_2 is considered to be on the brink of a CDW-like transition [122, 123, 124, 110, 125, 126, 219], while the closely related 2H-$NbSe_2$, does stabilise a CDW at 33.5 K. It is generally acknowledged that the charge density waves in this family of materials cannot be explained by electronic "nesting" alone, and it is important to consider the momentum-dependence of the electron-phonon interaction, which itself is related to the orbital character of the bands [253, 128, 129, 247, 121, 254, 255].

For the calculated bands along ΓK in 4.29(a), there is a crossover in orbital character between the doublets corresponding to the Γ barrels (mainly $4d_{3z^2-r^2}$) and the K barrels (mainly $4d_{x^2-y^2,xy}$). The experimental spectral function in Fig. 4.29(b) shows significantly different impact of electron-phonon coupling at the two pairs of Fermi crossings, with the second pair of crossings (corresponding to the K barrels) exhibiting a clear kink structure, characteristic of a strong electron-phonon interaction, whereas for the first pair (Γ barrels) the effect is much less prominent.

For a more quantitative analysis, we performed a fitting analysis to extract the band positions in Fig. 4.30(c). We extract the position and width of peaks in Fig. 4.30(a) by using a Lorentzian function. Because the intensity of the two branches at higher k_F

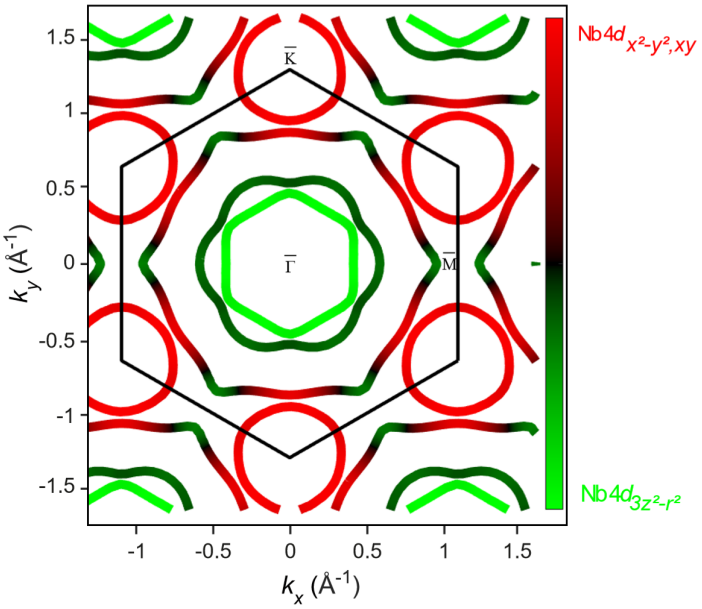

FIGURE 4.28: 2H-NbS_2. 2D Fermi surface with orbital character projection, as performed with DFT calculations using the mBJ functional. While the Γ barrel and the bands near the M point, derived from Nb $4d_{3z^2-r^2}$ reveal only a weak electron-phonon coupling, the K barrels, however, derived from Nb $4d_{x^2-y^2,xy}$ orbitals correspond to "hot regions", showing significantly larger interaction strength, and consequently larger superconducting gap.

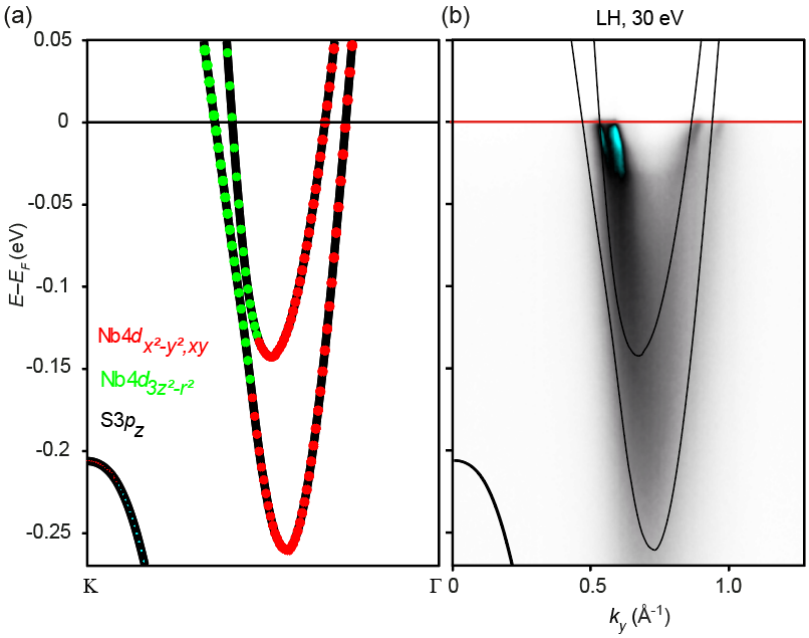

FIGURE 4.29: **Electron-phonon coupling in 2H-NbS_2.** (a) Calculated band dispersion along ΓK direction with orbital character projection. (b) ARPES data of the valence band dispersion along ΓK, measured at a photon energy $h\nu = 30$ eV, overlaid with DFT calculations for comparison.

are significantly decreasing below $B_E \sim 20$ meV, it is hard to extract the dispersion

by using curvature method in Fig. 4.30(b). For proper fitting, we start the MDC fitting from the Fermi level and use the extracted parameters for the subsequent MDC as the initial condition for the four Lorentzian functions. From this, we identify a "kink" energy of -15 meV for the K barrels; the deviation of the bands around this energy can also be visualised in the "curvature" plot in Fig. 4.30(b). Meanwhile the inner bands have a change of slope around -20 meV, but this is a more subtle effect.

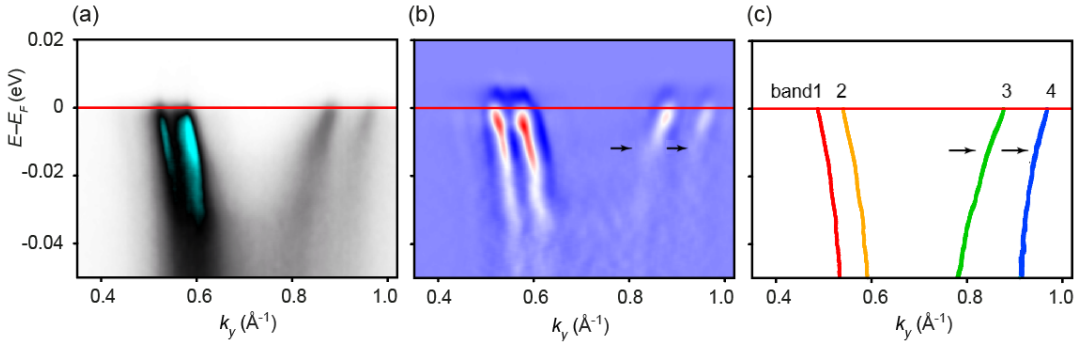

FIGURE 4.30: (a) Closer look at the data near E_F and (b) the 'curvature' plot of the data, highlighting kinks in the spectral function. (c) Momentum distribution curve (MDC) fitting of the data using a multi-lorenztian peak function.

A quantitative measure of electron-phonon coupling is the renormalisation of the Fermi velocity, $\lambda = (v_F(bare)/v_F(exp)) - 1$ [220]. There is some uncertainty here in the choice of bare band, since the k_F values in experiments do not match the DFT bands, there is a procedural subtlety in the determination of the renormalization of the Fermi velocities. In other contexts, it might be appropriate to shift the DFT bands in energy so that the k_F value matches before comparing v_F, but here we simply compare with the DFT v_F values without any shifting. We find a clear dichotomy between the innermost band 1, with $\lambda \approx 0.51$, and the outer crossings of the K barrel with $\lambda \approx 2.32$ for band 3 and $\lambda \approx 2.59$ for band 4.

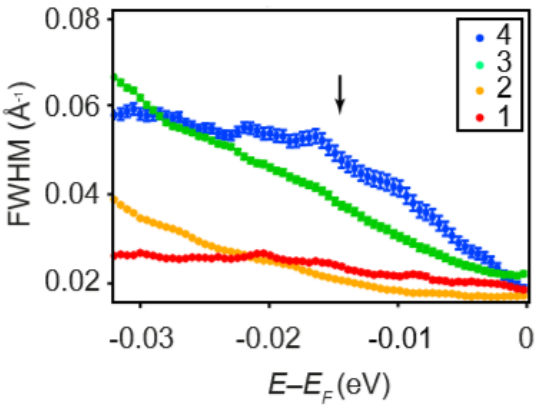

FIGURE 4.31: Peak widths of the four bands, showing the fast increase of the bands corresponding K barrels compared to the Γ barrels. A clear kink around -15 meV can be identified in the outermost band (band 4).

Additionally, in Fig. 4.31 we show a dichotomy in the energy-dependent linewidths,

as the broadening of the K barrels increase much faster with binding energy than the Γ barrels. The outermost band shows the fastest rise, consistent with having the strongest coupling, and also shows a saturation of the linewidth coinciding with the kink energy.

Taken together, this evidence strongly suggests that in 2H-NbS_2, the electron-phonon coupling depends crucially on the orbital character of the bands, and for the ΓK dispersion here the λ value is up to $\sim$ 4-5 times larger for the section with Nb $4d_{x^2-y^2,xy}$ character than for the Nb $4d_{3z^2-r^2}$. Our experiments are highly consistent with the calculations of Heil et al [126], who took the electron-phonon interaction into consideration and also found a significantly larger interaction strength on the sections of the K barrel closest to the K points, correlating closely with the $4d_{x^2-y^2,xy}$ orbital character.

This has important implications for the superconductivity, as it gives a natural explanation for the gap structure with two characteristic energy scales [122]. Presumably, the inner Γ sheets with weaker el-ph coupling would be "cold" areas corresponding to the smaller gap, while the straight sections of the K barrels ("hot" regions) would develop a larger gap.

4.3 Conclusions

We investigated the electronic band structure of 2H-NbS_2 and 3R-$Nb_{(1+x)}S_2$. In the 2H phase, we find sharp features and a Fermi surface broadly consistent with calculations, but our measured Fermi surface of 3R-$Nb_{(1+x)}S_2$ appears significantly smaller compared to the calculation, and also compared to the 2H phase. We assign this to a significant amount of extra charge in the 3R system due to interstitial Nb. It is the stoichiometry, rather than the stacking sequence, that principally determines the differences in electronic structure and physical properties between the two polytypes. Our high resolution data on 2H-NbS_2 revealed kinks in the spectral function, but the strength of the coupling was found to be much larger for the the sections of bands with Nb $4d_{x^2-y^2,xy}$ character than for the Nb $4d_{3z^2-r^2}$. Our measurements provide an experimental framework for interpreting the two-gap superconductivity and latent CDW in 2H-NbS_2, while also giving insight into the absence of these in the 3R-$Nb_{(1+x)}S_2$.

Recapping the results on 3R-$Nb_{(1+x)}S_2$, we showed that the prevalence of donor-type interstitials leads to a shifted chemical potential, smaller Fermi surfaces and a reduced DOS, moving the doped system away from any structural instabilities [256]. It is this difference, rather than the difference in stacking arrangement, that principally distinguishes the electronic and physical properties of the two phases.

If a stoichiometric 3R-NbS_2 existed, our DFT calculations suggest it would have a similar Fermi surface to the 2H phase, and therefore could similarly have interesting properties including potential non-centrosymmetric superconductivity. Unfortunately, stoichiometric 3R-NbS_2 is entirely hypothetical, and the only thermodynamic bulk phases are 3R-$Nb_{(1+x)}S_2$ and 2H-NbS_2. However, the monolayer limit provides a third structural form ("1H") of NbS_2, and has been predicted [219] and observed [238] to enter a CDW phase, although this may be substrate dependent

[237], and offers an interesting playground to tune the structural and superconducting instabilities [257].

Conclusions and Outlook

To summarize, we have demonstrated the tuning of the electronic structure of $HfTe_2$ by potassium K dosing, through an experimental realisation of a dimensionality crossover of the electronic band structure from a 3D bulk character of the pristine to a 2D character of the dosed surface. The measured electronic structure after high amount of dosing is very similar to a monolayer $HfTe_2$, unambiguously evidencing the intercalation of the alkali metal atoms within the van der Waals gaps. We also showed that the valence band of $HfTe_2$ along the out-of-plane k_z momentum supports the existence of a set of topological features such as a bulk Dirac point (BDP) and topological surface states (TSS), similar to other materials in the same space group.

One of the advantages of dosing this semimetallic system is that, by bringing the uppermost hole band below E_F, the band overlap can be directly measured. From Fig. 3.14(c), we estimate this to be $\sim$ 0.2 eV. We caution that this is a value for the surface-dosed system, and thus the bulk value may vary slightly, but we estimate it to be in the range 0.2-0.3 eV. A small band overlap is an interesting playground for novel electronic states. For instance, one could imagine substituting Se onto the Te site in order to continuously tune the band gap/overlap through zero, and it would be interesting to see if any electronic instabilities occur, such as in the well-known isovalent compound $TiSe_2$ [189, 86].

In addition to the published paper on $HfTe_2$, we have done several linear and circular dichroism measurements on $HfTe_2$ as well, disentangling the selection rules in this material and providing evidence that the observed CD signal is a pure consequence of the final states and geometrical effects, since the orbital angular momentum is quenched due to the inversion symmetry of the system. For this project, one-step photoemission calculations are expected to be combined with our measured data for a future publication.

Besides, we have investigated the electronic structure of the 2H and 3R polytypes of NbS_2 and evidenced that the main difference between them in term of the physical and electronic properties is intimately linked to the stoichiometry, rather than the stacking structure. While 2H-NbS_2 is stoichiometric, the 3R phase can only be stabilised with additional Nb interstitials, resulting in an off-stoichiometry of the form 3R-$Nb_{1+x}S_2$. These Nb interstitial act as electron donors, resulting in a shifted electronic band structure into higher binding energies compared to 2H-NbS_2, and putting away the 3R phase from any instabilities. The band splitting, present in the two phases have been measured, and its origin in each one of them has been revised in details.

Finally, our high resolution data revealed strong kinks in the spectral function of 2H-NbS_2, evidencing the electron-phonon coupling in this system. We demonstrated that this coupling varies strongly with the orbital character of the sheets forming the

Fermi surface and perfectly correlates the superconducting gap values. Our findings thus present an experimental explanation to the *multi-gap* nature of the superconductivity in 2H-NbS_2, in a similar way to the well-known materials MgB_2 and the isostructural and isovalent $NbSe_2$.

During our last beamtime on 2H-NbS_2, we have attempted to measure the superconducting gap in the straight section of the K barrel, where the gap exhibits its largest value in this material (0.97 meV). However, technical issues arising from the difficulty to stabilize the temperature below 2 or 3K during the whole experiment and the significantly flaky nature of the crystals make the resolution of such superconducting features very challenging. A possible solution we have been thinking of to overcome the flaky crystal facets would be to consider nano-ARPES, which could potentially be very helpful to resolve the superconducting gap in this case, however, micro-focused laser ARPES would be more reasonable approach for measuring gaps.

Although absent in the bulk compound due to anharmonic effects, charge density wave (CDW) has been lately reported in monolayer NbS_2 [238]. These studies have been performed on epitaxially grown single layers of NbS_2 on graphene/6H-SiC, where atomically resolved STM images revealed a 3×3 CDW, similar to the superstructure commonly observed in bulk 2H-TMDs, except 2H-NbS_2 itself [238]. Therefore, an ARPES investigation to confirm these findings is urgently required, however, the choice of the substrate is very crucial, since in this case the weak coupling between the graphene substrate and the sulfide film helps to preserve the intrinsic properties of the film, while in an epitaxially grown NbS_2 single-layer on Au(111) no CDW was observed [237]. It is most likely that the interactions with the substrate killed the CDW in the latter case, since recent first principle calculations have predicted the CDW in monolayer in NbS_2 to be very fragile, and strain as weak as 5% is sufficient to destroy it [219]. Although technically challenging to measure, it is now within the capability of nano-ARPES to measure gaps and backfolding as signatures of CDWs from monolayer samples, and I look forward to following progress on this.

Either for the bulk or monolayer NbS_2, the evolution of these novel electronic states as a function of strain and dosing would be very interesting to examine, as well as 3R-TMDs in general, which are still unexplored compared to other phases of this materials family.

Bibliography

[1] Sohail Ahmed and Jiabao Yi. "Two-dimensional transition metal dichalcogenides and their charge carrier mobilities in field-effect transistors". In: *Nano-micro letters* 9.4 (2017), p. 50.

[2] Aleksander A Tedstone, David J Lewis, and Paul O'Brien. "Synthesis, properties, and applications of transition metal-doped layered transition metal dichalcogenides". In: *Chemistry of Materials* 28.7 (2016), pp. 1965–1974.

[3] Henan Li et al. "Emerging energy applications of two-dimensional layered transition metal dichalcogenides". In: *Nano Energy* 18 (2015), pp. 293–305.

[4] CK Sumesh and Sebastian C Peter. "Two-dimensional semiconductor transition metal based chalcogenide based heterostructures for water splitting applications". In: *Dalton Transactions* 48.34 (2019), pp. 12772–12802.

[5] Xixia Zhang et al. "Transition Metal Dichalcogenides for the Application of Pollution Reduction: A Review". In: *Nanomaterials* 10.6 (2020), p. 1012.

[6] Supriyo Datta and Biswajit Das. "Electronic analog of the electro-optic modulator". In: *Applied Physics Letters* 56.7 (1990), pp. 665–667.

[7] Meysam Akhtar et al. "Recent advances in synthesis, properties, and applications of phosphorene". In: *npj 2D Materials and Applications* 1.1 (2017), pp. 1–13.

[8] Patrick K Schelling, Li Shi, and Kenneth E Goodson. "Managing heat for electronics". In: *Materials Today* 8.6 (2005), pp. 30–35.

[9] H Kamerlingh Onnes. "Further experiments with liquid helium". In: *Proceedings of the KNAW*. Vol. 13. 1911, pp. 1910–1911.

[10] A Schilling et al. "Superconductivity above 130 K in the Hg–Ba–Ca–Cu–O system". In: *Nature* 363.6424 (1993), pp. 56–58.

[11] Harald Ibach and Hans Lüth. "An Introduction to Principles of Materials Science". In: *Solid State and Physics, Springer, Berlin* (1995), p. 244.

[12] Steven H Simon. *The Oxford solid state basics*. OUP Oxford, 2013.

[13] MS Bahramy et al. "Ubiquitous formation of bulk Dirac cones and topological surface states from a single orbital manifold in transition-metal dichalcogenides". In: *Nature Materials* 17.1 (2018), p. 21. URL: https://www.nature.com/articles/nmat5031.

[14] Oliver Jon Clark. "Spin-and angle-resolved photoemission study of topological band inversions within a single orbital manifold". PhD thesis. University of St Andrews, 2019.

[15] P Hohenberg and W Kohn. "Physical review 136". In: *B864* (1964).

[16] John P Perdew. "Density functional theory and the band gap problem". In: *International Journal of Quantum Chemistry* 28.S19 (1985), pp. 497–523.

[17] David Koller, Fabien Tran, and Peter Blaha. "Improving the modified Becke-Johnson exchange potential". In: *Phys. Rev. B* 85 (15 Apr. 2012), p. 155109. DOI: 10.1103/PhysRevB.85.155109. URL: https://link.aps.org/doi/10.1103/PhysRevB.85.155109.

[18] Jochen Heyd, Gustavo E Scuseria, and Matthias Ernzerhof. "Hybrid functionals based on a screened Coulomb potential". In: *The Journal of chemical physics* 118.18 (2003), pp. 8207–8215.

[19] M Marsman et al. "Hybrid functionals applied to extended systems". In: *Journal of Physics: Condensed Matter* 20.6 (Jan. 2008), p. 064201. DOI: 10.1088/0953-8984/20/6/064201. URL: https://doi.org/10.1088.

[20] Peter Blaha et al. "WIEN2k: An APW+ lo program for calculating the properties of solids". In: *The Journal of Chemical Physics* 152.7 (2020), p. 074101.

[21] Hans Lüth. *Solid surfaces, interfaces and thin films*. Vol. 4. Springer, 2001.

[22] Stephan Hüfner. *Photoelectron spectroscopy: principles and applications*. Springer Science & Business Media, 2013. URL: https://www.springer.com/gp/book/9783540418023.

[23] Leslie L Foldy and Siegfried A Wouthuysen. "On the Dirac theory of spin 1/2 particles and its non-relativistic limit". In: *Physical Review* 78.1 (1950), p. 29.

[24] Albert Messiah and Leonard Isaac Schiff. *Quantum mechanics*. Vol. 643. McGraw-Hill College, 1968.

[25] Yu A Bychkov and E I Rashba. "Oscillatory effects and the magnetic susceptibility of carriers in inversion layers". In: 17.33 (Nov. 1984), pp. 6039–6045. DOI: 10.1088/0022-3719/17/33/015. URL: https://doi.org/10.1088%2F0022-3719%2F17%2F33%2F015.

[26] Gene Dresselhaus. "Spin-orbit coupling effects in zinc blende structures". In: *Physical Review* 100.2 (1955), p. 580.

[27] EU Condon and GH Shortley. "The Theory of Atomic Spectra, Cambridge University Press (1951)." In: ().

[28] Hadj M. Benia et al. "Reactive Chemical Doping of the Bi_2Se_3 Topological Insulator". In: *Phys. Rev. Lett.* 107 (17 Oct. 2011), p. 177602. DOI: 10.1103/PhysRevLett.107.177602. URL: https://link.aps.org/doi/10.1103/PhysRevLett.107.177602.

[29] MS Bahramy et al. "Emergence of non-centrosymmetric topological insulating phase in BiTeI under pressure". In: *Nature communications* 3.1 (2012), pp. 1–7.

[30] Jonathon Mark Riley et al. "Negative electronic compressibility and tunable spin splitting in WSe_2". In: *Nature Nanotechnology* 10.12 (2015), p. 1043. URL: https://www.nature.com/articles/nnano.2015.217.

[31] Mingu Kang et al. "Universal mechanism of band-gap engineering in transition-metal dichalcogenides". In: *Nano letters* 17.3 (2017), pp. 1610–1615. URL: https://pubs.acs.org/doi/abs/10.1021/acs.nanolett.6b04775.

[32] Matteo Michiardi et al. "Strongly anisotropic spin-orbit splitting in a two-dimensional electron gas". In: *Phys. Rev. B* 91 (3 Jan. 2015), p. 035445. DOI: 10.1103/PhysRevB.91.035445. URL: https://link.aps.org/doi/10.1103/PhysRevB.91.035445.

[33] O. J. Clark et al. "Dual quantum confinement and anisotropic spin splitting in the multivalley semimetal $PtSe_2$". In: *Phys. Rev. B* 99 (4 Jan. 2019), p. 045438. DOI: 10.1103/PhysRevB.99.045438. URL: https://link.aps.org/doi/10.1103/PhysRevB.99.045438.

[34] S. LaShell, B. A. McDougall, and E. Jensen. "Spin Splitting of an Au(111) Surface State Band Observed with Angle Resolved Photoelectron Spectroscopy". In: *Phys. Rev. Lett.* 77 (16 Oct. 1996), pp. 3419–3422. DOI: 10.1103/PhysRevLett.77.3419. URL: https://link.aps.org/doi/10.1103/PhysRevLett.77.3419.

[35] G. Nicolay et al. "Spin-orbit splitting of the L-gap surface state on Au(111) and Ag(111)". In: *Phys. Rev. B* 65 (3 Dec. 2001), p. 033407. DOI: 10.1103/PhysRevB.65.033407. URL: https://link.aps.org/doi/10.1103/PhysRevB.65.033407.

[36] M. Hoesch et al. "Spin structure of the Shockley surface state on Au(111)". In: *Phys. Rev. B* 69 (24 June 2004), p. 241401. DOI: 10.1103/PhysRevB.69.241401. URL: https://link.aps.org/doi/10.1103/PhysRevB.69.241401.

[37] A. Tamai et al. "Spin-orbit splitting of the Shockley surface state on Cu(111)". In: *Phys. Rev. B* 87 (7 Feb. 2013), p. 075113. DOI: 10.1103/PhysRevB.87.075113. URL: https://link.aps.org/doi/10.1103/PhysRevB.87.075113.

[38] Beomyoung Kim et al. "Spin and orbital angular momentum structure of Cu(111) and Au(111) surface states". In: *Phys. Rev. B* 85 (19 May 2012), p. 195402. DOI: 10.1103/PhysRevB.85.195402. URL: https://link.aps.org/doi/10.1103/PhysRevB.85.195402.

[39] Hanyoung Ryu et al. "Photon energy dependent circular dichroism in angle-resolved photoemission from Au(111) surface states". In: *Phys. Rev. B* 95 (11 Mar. 2017), p. 115144. DOI: 10.1103/PhysRevB.95.115144. URL: https://link.aps.org/doi/10.1103/PhysRevB.95.115144.

[40] Hongtao Yuan et al. "Zeeman-type spin splitting controlled by an electric field". In: *Nature Physics* 9.9 (2013), pp. 563–569.

[41] Xiuwen Zhang et al. "Hidden spin polarization in inversion-symmetric bulk crystals". In: *Nature Physics* 10.5 (2014), pp. 387–393.

[42] Jonathon Mark Riley et al. "Direct observation of spin-polarized bulk bands in an inversion-symmetric semiconductor". In: *Nature Physics* 10.11 (2014), pp. 835–839.

[43] R Suzuki et al. "Valley-dependent spin polarization in bulk MoS_2 with broken inversion symmetry". In: *Nature nanotechnology* 9.8 (2014), p. 611.

[44] Lewis Bawden et al. "Spin-valley locking in the normal state of a transition-metal dichalcogenide superconductor". In: *Nature communications* 7 (2016), p. 11711.

[45] E. Razzoli et al. "Selective Probing of Hidden Spin-Polarized States in Inversion-Symmetric Bulk MoS_2". In: *Phys. Rev. Lett.* 118 (8 Feb. 2017), p. 086402. DOI: 10.1103/PhysRevLett.118.086402. URL: https://link.aps.org/doi/10.1103/PhysRevLett.118.086402.

[46] K Ishizaka et al. "Giant Rashba-type spin splitting in bulk BiTeI". In: *Nature materials* 10.7 (2011), pp. 521–526.

[47] A. Crepaldi et al. "Giant Ambipolar Rashba Effect in the Semiconductor BiTeI". In: *Phys. Rev. Lett.* 109 (9 Aug. 2012), p. 096803. DOI: 10.1103/PhysRevLett.109.096803. URL: https://link.aps.org/doi/10.1103/PhysRevLett.109.096803.

[48] Lewis Bawden et al. "Hierarchical spin-orbital polarization of a giant Rashba system". In: *Science Advances* 1.8 (2015). DOI: 10.1126/sciadv.1500495. eprint: https://advances.sciencemag.org/content/1/8/e1500495.full.pdf. URL: https://advances.sciencemag.org/content/1/8/e1500495.

[49] K. S. Novoselov et al. "Electric Field Effect in Atomically Thin Carbon Films". In: *Science* 306.5696 (2004), pp. 666–669. ISSN: 0036-8075. DOI: 10.1126/science.1102896. eprint: https://science.sciencemag.org/content/306/5696/666.full.pdf. URL: https://science.sciencemag.org/content/306/5696/666.

[50] Hassan Raza. *Graphene nanoelectronics: Metrology, synthesis, properties and applications*. Springer Science & Business Media, 2012.

[51] Kostya S Novoselov et al. "Two-dimensional gas of massless Dirac fermions in graphene". In: *nature* 438.7065 (2005), pp. 197–200.

[52] MI Katsnelson, KS Novoselov, and AK Geim. "Chiral tunnelling and the Klein paradox in graphene". In: *Nature physics* 2.9 (2006), pp. 620–625.

[53] Konstantin S Novoselov and AK Geim. "The rise of graphene". In: *Nat. Mater* 6.3 (2007), pp. 183–191.

[54] A. H. Castro Neto et al. "The electronic properties of graphene". In: *Rev. Mod. Phys.* 81 (1 Jan. 2009), pp. 109–162. DOI: 10.1103/RevModPhys.81.109. URL: https://link.aps.org/doi/10.1103/RevModPhys.81.109.

[55] Jian-Hao Chen et al. "Intrinsic and extrinsic performance limits of graphene devices on SiO_2". In: *Nature nanotechnology* 3.4 (2008), p. 206.

[56] V. P. Gusynin and S. G. Sharapov. "Unconventional Integer Quantum Hall Effect in Graphene". In: *Phys. Rev. Lett.* 95 (14 Sept. 2005), p. 146801. DOI: 10.1103/PhysRevLett.95.146801. URL: https://link.aps.org/doi/10.1103/PhysRevLett.95.146801.

[57] Xiangfan Xu et al. "Length-dependent thermal conductivity in suspended single-layer graphene". In: *Nature communications* 5.1 (2014), pp. 1–6.

[58] Yuanbo Zhang et al. "Experimental observation of the quantum Hall effect and Berry's phase in graphene". In: *nature* 438.7065 (2005), pp. 201–204.

[59] Kostya S Novoselov et al. "Unconventional quantum Hall effect and Berry's phase of 2π in bilayer graphene". In: *Nature physics* 2.3 (2006), pp. 177–180.

[60] Edward McCann and Vladimir I. Fal'ko. "Landau-Level Degeneracy and Quantum Hall Effect in a Graphite Bilayer". In: *Phys. Rev. Lett.* 96 (8 Mar. 2006), p. 086805. DOI: 10.1103/PhysRevLett.96.086805. URL: https://link.aps.org/doi/10.1103/PhysRevLett.96.086805.

[61] Jl A Wilson and AD Yoffe. "The transition metal dichalcogenides discussion and interpretation of the observed optical, electrical and structural properties". In: *Advances in Physics* 18.73 (1969), pp. 193–335.

[62] AD Yoffe. "Electronic properties of some chain and layer compounds". In: *Chemical Society Reviews* 5 (1976), pp. 51–78.

[63] RMA Lieth and JCJM Terhell. "Transition metal dichalcogenides". In: *Preparation and crystal growth of materials with layered structures*. Springer, 1977, pp. 141–223.

[64] Francis Alain Lévy. *Crystallography and crystal chemistry of materials with layered structures*. Vol. 2. Springer Science & Business Media, 2012.

[65] Fritz Hulliger. *Structural chemistry of layer-type phases*. Vol. 5. Springer Science & Business Media, 2012.

[66] FR Gamble and TH Geballe. "Inclusion Compounds". In: *Treatise on Solid State Chemistry*. Springer, 1976, pp. 89–166.

[67] M Stanley Whittingham. "Chemistry of intercalation compounds: metal guests in chalcogenide hosts". In: *Progress in Solid State Chemistry* 12.1 (1978), pp. 41–99.

[68] Wayne G Fisher and MJ Sienko. "Stoichiometry, structure, and physical properties of niobium disulfide". In: *Inorganic Chemistry* 19.1 (1980), pp. 39–43.

[69] A. S. Ngankeu. "Study of the Electronic Properties of Three- and Two-Dimensional Transition Metal Dichalcogenides". In: 2017.

[70] L. F. Mattheiss. "Band Structures of Transition-Metal-Dichalcogenide Layer Compounds". In: *Phys. Rev. B* 8 (8 Oct. 1973), pp. 3719–3740. DOI: 10.1103/PhysRevB.8.3719. URL: https://link.aps.org/doi/10.1103/PhysRevB.8.3719.

[71] Manish Chhowalla et al. "The chemistry of two-dimensional layered transition metal dichalcogenide nanosheets". In: *Nature chemistry* 5.4 (2013), p. 263.

[72] Toru Kanazawa et al. "Few-layer HfS_2 transistors". In: *Scientific reports* 6 (2016), p. 22277. URL: https://www.nature.com/articles/srep22277.

[73] Qiyi Zhao et al. "Elastic, electronic, and dielectric properties of bulk and monolayer ZrS_2, $ZrSe_2$, HfS_2, $HfSe_2$ from van der Waals density-functional theory". In: *physica status solidi (b)* 254.9 (2017), p. 1700033. URL: https://doi.org/10.1002/pssb.201700033.

[74] Ch J Raub et al. "The occurrence of superconductivity in sulfides, selenides, tellurides of Pt-group metals". In: *Journal of Physics and Chemistry of Solids* 26.12 (1965), pp. 2051–2057.

[75] David T Hodul and Angelica M Stacy. "The effects of non-stoichiometry and electron concentration on the properties of $Li_xHfTe_2 - y$". In: *Journal of Physics and Chemistry of Solids* 46.12 (1985), pp. 1447–1453. URL: https://www.sciencedirect.com/science/article/abs/pii/S0022231309003329.

[76] AM Woolley and G Wexler. "Band structures and Fermi surfaces for 1T-TaS_2, 1T-$TaSe_2$ and 1T-VSe_2". In: *Journal of Physics C: Solid State Physics* 10.14 (1977), p. 2601.

[77] NV Smith, SD Kevan, and FJ DiSalvo. "Band structures of the layer compounds 1T-TaS_2 and 2H-$TaSe_2$ in the presence of commensurate charge-density waves". In: *Journal of Physics C: Solid State Physics* 18.16 (1985), p. 3175.

[78] DJ Eaglesham, RL Withers, and DM Bird. "Charge-density-wave transitions in 1T-VSe_2". In: *Journal of Physics C: Solid State Physics* 19.3 (1986), p. 359.

[79] B. Giambattista et al. "Scanning tunneling microscopy of atoms and charge-density waves in 1T-TaS_2, 1T-$TaSe_2$, and 1T-VSe_2". In: *Phys. Rev. B* 41 (14 May 1990), pp. 10082–10103. DOI: 10.1103/PhysRevB.41.10082. URL: https://link.aps.org/doi/10.1103/PhysRevB.41.10082.

[80] Th. Straub et al. "Charge-Density-Wave Mechanism in $2H - NbSe_2$: Photoemission Results". In: *Phys. Rev. Lett.* 82 (22 May 1999), pp. 4504–4507. DOI: 10.1103/PhysRevLett.82.4504. URL: https://link.aps.org/doi/10.1103/PhysRevLett.82.4504.

[81] Agnieszka Kuc and Thomas Heine. "The electronic structure calculations of two-dimensional transition-metal dichalcogenides in the presence of external electric and magnetic fields". In: *Chemical Society Reviews* 44.9 (2015), pp. 2603–2614.

[82] Lewis Bawden. "A spin-and angle-resolved photoemission study of coupled spin-orbital textures driven by global and local inversion symmetry breaking". PhD thesis. University of St Andrews, 2017.

[83] Jl A Wilson and AD Yoffe. "The transition metal dichalcogenides discussion and interpretation of the observed optical, electrical and structural properties". In: *Advances in Physics* 18.73 (1969), pp. 193–335.

[84] Michio Naito and Shoji Tanaka. "Electrical Transport Properties in 2H-NbS_2,-$NbSe_2$,-TaS_2 and -$TaSe_2$". In: *Journal of the Physical Society of Japan* 51.1 (1982), pp. 219–227.

[85] T. Eknapakul et al. "Direct observation of strain-induced orbital valence band splitting in $HfSe_2$ by sodium intercalation". In: *Phys. Rev. B* 97 (20 May 2018), p. 201104. DOI: 10.1103/PhysRevB.97.201104. URL: https://link.aps.org/doi/10.1103/PhysRevB.97.201104.

[86] Matthew D. Watson et al. "Orbital- and k_z-Selective Hybridization of Se $4p$ and Ti $3d$ States in the Charge Density Wave Phase of $TiSe_2$". In: *Phys. Rev. Lett.* 122 (7 Feb. 2019), p. 076404. DOI: 10.1103/PhysRevLett.122.076404. URL: https://link.aps.org/doi/10.1103/PhysRevLett.122.076404.

[87] Di Xiao et al. "Coupled Spin and Valley Physics in Monolayers of MoS_2 and Other Group-VI Dichalcogenides". In: *Phys. Rev. Lett.* 108 (19 May 2012), p. 196802. DOI: 10.1103/PhysRevLett.108.196802. URL: https://link.aps.org/doi/10.1103/PhysRevLett.108.196802.

[88] Xiaodong Xu and Wang Yao. "Di Xiao, and Tony F Heinz. Spin and pseudospins in layered transition metal dichalcogenides". In: *Nature Physics* 10.5 (2014), pp. 343–350.

[89] Kin Fai Mak et al. "Atomically Thin MoS_2: A New Direct-Gap Semiconductor". In: *Phys. Rev. Lett.* 105 (13 Sept. 2010), p. 136805. DOI: 10.1103/PhysRevLett.105.136805. URL: https://link.aps.org/doi/10.1103/PhysRevLett.105.136805.

[90] Hualing Zeng et al. "Valley polarization in MoS_2 monolayers by optical pumping". In: *Nature nanotechnology* 7.8 (2012), pp. 490–493.

[91] Kin Fai Mak et al. "Control of valley polarization in monolayer MoS_2 by optical helicity". In: *Nature nanotechnology* 7.8 (2012), pp. 494–498.

[92] Ting Cao et al. "Valley-selective circular dichroism of monolayer molybdenum disulphide". In: *Nature communications* 3.1 (2012), pp. 1–5.

[93] Kazuyuki Sakamoto et al. "Valley spin polarization by using the extraordinary Rashba effect on silicon". In: *Nature communications* 4.1 (2013), pp. 1–6.

[94] R. Coehoorn et al. "Electronic structure of $MoSe_2$, MoS_2, and WSe_2. I. Band-structure calculations and photoelectron spectroscopy". In: *Phys. Rev. B* 35 (12 Apr. 1987), pp. 6195–6202. DOI: 10.1103/PhysRevB.35.6195. URL: https://link.aps.org/doi/10.1103/PhysRevB.35.6195.

[95] R. Coehoorn, C. Haas, and R. A. de Groot. "Electronic structure of $MoSe_2$, MoS_2, and WSe_2. II. The nature of the optical band gaps". In: *Phys. Rev. B* 35 (12 Apr. 1987), pp. 6203–6206. DOI: 10.1103/PhysRevB.35.6203. URL: https://link.aps.org/doi/10.1103/PhysRevB.35.6203.

[96] Tawinan Cheiwchanchamnangij and Walter R. L. Lambrecht. "Quasiparticle band structure calculation of monolayer, bilayer, and bulk MoS_2". In: *Phys. Rev. B* 85 (20 May 2012), p. 205302. DOI: 10.1103/PhysRevB.85.205302. URL: https://link.aps.org/doi/10.1103/PhysRevB.85.205302.

[97] Eugene S Kadantsev and Pawel Hawrylak. "Electronic structure of a single MoS_2 monolayer". In: *Solid State Communications* 152.10 (2012), pp. 909–913.

[98] Qing Hua Wang et al. "Electronics and optoelectronics of two-dimensional transition metal dichalcogenides". In: *Nature nanotechnology* 7.11 (2012), p. 699.

[99] Won Seok Yun et al. "Thickness and strain effects on electronic structures of transition metal dichalcogenides: 2H-MX_2 semiconductors (M = Mo, W; X = S, Se, Te)". In: *Phys. Rev. B* 85 (3 Jan. 2012), p. 033305. DOI: 10.1103/PhysRevB.85.033305. URL: https://link.aps.org/doi/10.1103/PhysRevB.85.033305.

[100] Wencan Jin et al. "Direct Measurement of the Thickness-Dependent Electronic Band Structure of MoS_2 Using Angle-Resolved Photoemission Spectroscopy". In: *Phys. Rev. Lett.* 111 (10 Sept. 2013), p. 106801. DOI: 10.1103/PhysRevLett.111.106801. URL: https://link.aps.org/doi/10.1103/PhysRevLett.111.106801.

[101] Weijie Zhao et al. "Evolution of electronic structure in atomically thin sheets of WS_2 and WSe_2". In: *ACS nano* 7.1 (2013), pp. 791–797.

[102] Yi Zhang et al. "Direct observation of the transition from indirect to direct bandgap in atomically thin epitaxial $MoSe_2$". In: *Nature nanotechnology* 9.2 (2014), p. 111.

[103] Hualing Zeng et al. "Optical signature of symmetry variations and spin-valley coupling in atomically thin tungsten dichalcogenides". In: *Scientific reports* 3 (2013), p. 1608.

[104] R. Bertoni et al. "Generation and Evolution of Spin-, Valley-, and Layer-Polarized Excited Carriers in Inversion-Symmetric WSe_2". In: *Phys. Rev. Lett.* 117 (27 Dec. 2016), p. 277201. DOI: 10.1103/PhysRevLett.117.277201. URL: https://link.aps.org/doi/10.1103/PhysRevLett.117.277201.

[105] R Suzuki et al. "Valley-dependent spin polarization in bulk MoS_2 with broken inversion symmetry". In: *Nature nanotechnology* 9.8 (2014), p. 611.

[106] Haijun Zhang et al. "Topological insulators in Bi_2Se_3, Bi_2Te_3 and Sb_2Te_3 with a single Dirac cone on the surface". In: *Nature physics* 5.6 (2009), pp. 438–442.

[107] O. J. Clark et al. "Fermiology and Superconductivity of Topological Surface States in $PdTe_2$". In: *Phys. Rev. Lett.* 120 (15 Apr. 2018), p. 156401. DOI: 10.1103/PhysRevLett.120.156401. URL: https://link.aps.org/doi/10.1103/PhysRevLett.120.156401.

[108] Oliver Jon Clark et al. "A general route to form topologically-protected surface and bulk Dirac fermions along high-symmetry lines". In: *Electronic Structure* 1.1 (2019), p. 014002.

[109] Barun Ghosh et al. "Observation of bulk states and spin-polarized topological surface states in transition metal dichalcogenide Dirac semimetal candidate $NiTe_2$". In: *Phys. Rev. B* 100 (19 Nov. 2019), p. 195134. DOI: 10.1103/PhysRevB.100.195134. URL: https://link.aps.org/doi/10.1103/PhysRevB.100.195134.

[110] M. Leroux et al. "Anharmonic suppression of charge density waves in 2H-NbS_2". In: *Phys. Rev. B* 86 (15 Oct. 2012), p. 155125. DOI: 10.1103/PhysRevB.86.155125. URL: https://link.aps.org/doi/10.1103/PhysRevB.86.155125.

[111] Chenhaoping Wen et al. "Impurity-pinned incommensurate charge density wave and local phonon excitations in $2H-NbS_2$". In: *Phys. Rev. B* 101 (24 June 2020), p. 241404. DOI: 10.1103/PhysRevB.101.241404. URL: https://link.aps.org/doi/10.1103/PhysRevB.101.241404.

[112] Balazs Sipos et al. "From Mott state to superconductivity in 1T-TaS_2". In: *Nature materials* 7.12 (2008), pp. 960–965.

[113] J. A. Wilson, F. J. Di Salvo, and S. Mahajan. "Charge-Density Waves in Metallic, Layered, Transition-Metal Dichalcogenides". In: *Phys. Rev. Lett.* 32 (16 Apr. 1974), pp. 882–885. DOI: 10.1103/PhysRevLett.32.882. URL: https://link.aps.org/doi/10.1103/PhysRevLett.32.882.

[114] Maxime Leroux et al. "Traces of charge density waves in NbS_2". In: *Phys. Rev. B* 97 (19 May 2018), p. 195140. DOI: 10.1103/PhysRevB.97.195140. URL: https://link.aps.org/doi/10.1103/PhysRevB.97.195140.

[115] Matteo Calandra, I. I. Mazin, and Francesco Mauri. "Effect of dimensionality on the charge-density wave in few-layer 2H-$NbSe_2$". In: *Phys. Rev. B* 80 (24 Dec. 2009), p. 241108. DOI: 10.1103/PhysRevB.80.241108. URL: https://link.aps.org/doi/10.1103/PhysRevB.80.241108.

[116] Xiaoxiang Xi et al. "Strongly enhanced charge-density-wave order in monolayer $NbSe_2$". In: *Nature nanotechnology* 10.9 (2015), p. 765.

[117] Emilia Morosan et al. "Superconductivity in Cu x $TiSe_2$". In: *Nature Physics* 2.8 (2006), pp. 544–550.

[118] T. Valla et al. "Quasiparticle Spectra, Charge-Density Waves, Superconductivity, and Electron-Phonon Coupling in 2H$-NbSe_2$". In: *Phys. Rev. Lett.* 92 (8 Feb. 2004), p. 086401. DOI: 10.1103/PhysRevLett.92.086401. URL: https://link.aps.org/doi/10.1103/PhysRevLett.92.086401.

[119] J. D. Fletcher et al. "Penetration Depth Study of Superconducting Gap Structure of 2$H-NbSe_2$". In: *Phys. Rev. Lett.* 98 (5 Feb. 2007), p. 057003. DOI: 10.1103/PhysRevLett.98.057003. URL: https://link.aps.org/doi/10.1103/PhysRevLett.98.057003.

[120] S. V. Borisenko et al. "Pseudogap and Charge Density Waves in Two Dimensions". In: *Phys. Rev. Lett.* 100 (19 May 2008), p. 196402. DOI: 10.1103/PhysRevLett.100.196402. URL: https://link.aps.org/doi/10.1103/PhysRevLett.100.196402.

[121] D. J. Rahn et al. "Gaps and kinks in the electronic structure of the superconductor 2*H*-$NbSe_2$ from angle-resolved photoemission at 1 K". In: *Phys. Rev. B* 85 (22 June 2012), p. 224532. DOI: 10.1103/PhysRevB.85.224532. URL: https://link.aps.org/doi/10.1103/PhysRevB.85.224532.

[122] I. Guillamón et al. "Superconducting Density of States and Vortex Cores of 2H-NbS_2". In: *Phys. Rev. Lett.* 101 (16 Oct. 2008), p. 166407. DOI: 10.1103/PhysRevLett.101.166407. URL: https://link.aps.org/doi/10.1103/PhysRevLett.101.166407.

[123] J. Ka čmar čık et al. "Specific heat measurements of a superconducting NbS_2 single crystal in an external magnetic field: Energy gap structure". In: *Phys. Rev. B* 82 (1 July 2010), p. 014518. DOI: 10.1103/PhysRevB.82.014518. URL: https://link.aps.org/doi/10.1103/PhysRevB.82.014518.

[124] P. Diener et al. "In-plane magnetic penetration depth in NbS_2". In: *Phys. Rev. B* 84 (5 Aug. 2011), p. 054531. DOI: 10.1103/PhysRevB.84.054531. URL: https://link.aps.org/doi/10.1103/PhysRevB.84.054531.

[125] V. G. Tissen et al. "Pressure dependence of superconducting critical temperature and upper critical field of 2*H*-NbS_2". In: *Phys. Rev. B* 87 (13 Apr. 2013), p. 134502. DOI: 10.1103/PhysRevB.87.134502. URL: https://link.aps.org/doi/10.1103/PhysRevB.87.134502.

[126] Christoph Heil et al. "Origin of Superconductivity and Latent Charge Density Wave in NbS_2". In: *Phys. Rev. Lett.* 119 (8 Aug. 2017), p. 087003. DOI: 10.1103/PhysRevLett.119.087003. URL: https://link.aps.org/doi/10.1103/PhysRevLett.119.087003.

[127] George Gruner. *Density waves in solids*. CRC press, 2018.

[128] M. D. Johannes, I. I. Mazin, and C. A. Howells. "Fermi-surface nesting and the origin of the charge-density wave in $NbSe_2$". In: *Phys. Rev. B* 73 (20 May 2006), p. 205102. DOI: 10.1103/PhysRevB.73.205102. URL: https://link.aps.org/doi/10.1103/PhysRevB.73.205102.

[129] M. D. Johannes and I. I. Mazin. "Fermi surface nesting and the origin of charge density waves in metals". In: *Phys. Rev. B* 77 (16 Apr. 2008), p. 165135. DOI: 10.1103/PhysRevB.77.165135. URL: https://link.aps.org/doi/10.1103/PhysRevB.77.165135.

[130] F. Weber et al. "Extended Phonon Collapse and the Origin of the Charge-Density Wave in $2H-NbSe_2$". In: *Phys. Rev. Lett.* 107 (10 Sept. 2011), p. 107403. DOI: 10.1103/PhysRevLett.107.107403. URL: https://link.aps.org/doi/10.1103/PhysRevLett.107.107403.

[131] Maxime Leroux et al. "Strong anharmonicity induces quantum melting of charge density wave in $2H-NbSe_2$ under pressure". In: *Phys. Rev. B* 92 (14 Oct. 2015), p. 140303. DOI: 10.1103/PhysRevB.92.140303. URL: https://link.aps.org/doi/10.1103/PhysRevB.92.140303.

[132] FJ Himpsel. "Angle-resolved measurements of the photoemission of electrons in the study of solids". In: *Advances in Physics* 32.1 (1983), pp. 1–51.

[133] Stephen Douglas Kevan. *Angle-resolved photoemission: theory and current applications*. Elsevier, 1992.

[134] S Hüfner et al. "Photoemission spectroscopy in metals:: band structure-Fermi surface spectral function". In: *Journal of electron spectroscopy and related phenomena* 100.1-3 (1999), pp. 191–213.

[135] Andrea Damascelli, Zahid Hussain, and Zhi-Xun Shen. "Angle-resolved photoemission studies of the cuprate superconductors". In: *Rev. Mod. Phys.* 75 (2 Apr. 2003), pp. 473–541. DOI: 10.1103/RevModPhys.75.473. URL: https://link.aps.org/doi/10.1103/RevModPhys.75.473.

[136] Andrea Damascelli. "Probing the Electronic Structure of Complex Systems by ARPES". In: *Physica Scripta* T109 (2004), p. 61. DOI: 10.1238/physica.topical.109a00061. URL: https://doi.org/10.1238%2Fphysica.topical.109a00061.

[137] Heinrich Hertz. "Ueber einen Einfluss des ultravioletten Lichtes auf die electrische Entladung". In: *Annalen der Physik* 267.8 (1887), pp. 983–1000.

[138] Albert Einstein. "ber einen die Erzeugung und Verwandlung des Lichtes betreffenden heuristischen Gesichtspunkt". In: *Annalen der Physik* 322.6 (1905), pp. 132–148.

[139] Peter J. Feibelman and D. E. Eastman. "Photoemission spectroscopy Correspondence between quantum theory and experimental phenomenology". In: *Phys. Rev. B* 10 (12 Dec. 1974), pp. 4932–4947. DOI: 10.1103/PhysRevB.10.4932. URL: https://link.aps.org/doi/10.1103/PhysRevB.10.4932.

[140] V. N. Strocov et al. "Three-dimensional band structure of layered $TiTe_2$: Photoemission final-state effects". In: *Phys. Rev. B* 74 (19 Nov. 2006), p. 195125. DOI: 10.1103/PhysRevB.74.195125. URL: https://link.aps.org/doi/10.1103/PhysRevB.74.195125.

[141] M Pl Seah and WA Dench. "Quantitative electron spectroscopy of surfaces: A standard data base for electron inelastic mean free paths in solids". In: *Surface and interface analysis* 1.1 (1979), pp. 2–11.

[142] N. V. Smith, P. Thiry, and Y. Petroff. "Photoemission linewidths and quasiparticle lifetimes". In: *Phys. Rev. B* 47 (23 June 1993), pp. 15476–15481. DOI: 10.1103/PhysRevB.47.15476. URL: https://link.aps.org/doi/10.1103/PhysRevB.47.15476.

[143] VN Strocov. "Intrinsic accuracy in 3-dimensional photoemission band mapping". In: *Journal of Electron Spectroscopy and related phenomena* 130.1-3 (2003), pp. 65–78. URL: https://www.sciencedirect.com/science/article/pii/S0368204803000549.

[144] H Wadati et al. "Angle-resolved photoemission spectroscopy of perovskite-type transition-metal oxides and their analyses using tight-binding band structure". In: *Phase Transitions* 79.8 (2006), pp. 617–635.

[145] Zakariae El Youbi et al. "Bulk and surface electronic states in the dosed semimetallic $HfTe_2$". In: *Phys. Rev. B* 101 (23 June 2020), p. 235431. DOI: 10.1103/PhysRevB.101.235431. URL: https://link.aps.org/doi/10.1103/PhysRevB.101.235431.

[146] Muhammad Y Bashouti et al. "A non-oxidative approach towards hybrid silicon nanowire-based solar cell heterojunctions". In: (2014).

[147] Sunjic Doniach and M Sunjic. "Many-electron singularity in X-ray photoemission and X-ray line spectra from metals". In: *Journal of Physics C: Solid State Physics* 3.2 (1970), p. 285.

[148] Dave A Shirley. "High-resolution X-ray photoemission spectrum of the valence bands of gold". In: *Physical Review B* 5.12 (1972), p. 4709.

[149] Siegfried Hofmann. *Auger-and X-ray photoelectron spectroscopy in materials science: a user-oriented guide*. Vol. 49. Springer Science & Business Media, 2012.

[150] Paul S Bagus, Eugene S Ilton, and Connie J Nelin. "The interpretation of XPS spectra: Insights into materials properties". In: *Surface Science Reports* 68.2 (2013), pp. 273–304.

[151] M Hoesch et al. "A facility for the analysis of the electronic structures of solids and their surfaces by synchrotron radiation photoelectron spectroscopy". In: *Review of Scientific Instruments* 88.1 (2017), p. 013106. URL: https://doi.org/10.1063/1.4973562.

[152] Settimio Mobilio, Federico Boscherini, and Carlo Meneghini. *Synchrotron Radiation*. Springer, 2016.

[153] G. Levy et al. "Deconstruction of resolution effects in angle-resolved photoemission". In: *Phys. Rev. B* 90 (4 July 2014), p. 045150. DOI: 10.1103/PhysRevB.90.045150. URL: https://link.aps.org/doi/10.1103/PhysRevB.90.045150.

[154] Saumya Mukherjee et al. "Fermi-crossing Type-II Dirac fermions and topological surface states in $NiTe_2$". In: *Scientific reports* 10.1 (2020), pp. 1–9.

[155] S. Mangelsen et al. "Large nonsaturating magnetoresistance and pressure-induced phase transition in the layered semimetal $HfTe_2$". In: *Phys. Rev. B* 96 (20 Nov. 2017), p. 205148. DOI: 10.1103/PhysRevB.96.205148. URL: https://link.aps.org/doi/10.1103/PhysRevB.96.205148.

[156] Yun Kim, Jin-Lin Huang, and Charles M Lieber. "Characterization of nanometer scale wear and oxidation of transition metal dichalcogenide lubricants by atomic force microscopy". In: *Applied physics letters* 59.26 (1991), pp. 3404–3406.

[157] R. Claessen et al. "Complete band-structure determination of the quasi-two-dimensional Fermi-liquid reference compound $TiTe_2$". In: *Phys. Rev. B* 54 (4 July 1996), pp. 2453–2465. DOI: 10.1103/PhysRevB.54.2453. URL: https://link.aps.org/doi/10.1103/PhysRevB.54.2453.

[158] K. Rossnagel et al. "Three-dimensional Fermi surface determination by angle-resolved photoelectron spectroscopy". In: *Phys. Rev. B* 63 (12 Mar. 2001), p. 125104. DOI: 10.1103/PhysRevB.63.125104. URL: https://link.aps.org/doi/10.1103/PhysRevB.63.125104.

[159] Ali Hussain Reshak and S. Auluck. "Electronic and optical properties of the 1*T* phases of TiS_2, $TiSe_2$, and $TiTe_2$". In: *Phys. Rev. B* 68 (24 Dec. 2003), p. 245113. DOI: 10.1103/PhysRevB.68.245113. URL: https://link.aps.org/doi/10.1103/PhysRevB.68.245113.

[160] LEIF Brattas and ARNE KJEKSHUS. "On the Properties of the Zirconium & Hafnium Dichalcogenides". In: *Acta Cehmica Scandinavica* 27 (1973), pp. 1290–1298.

[161] S Takahashi et al. "Transport and elastic anomalies in $ZrTe_3$". In: *Solid state communications* 49.11 (1984), pp. 1031–1034.

[162] Qiang Li et al. "Chiral magnetic effect in $ZrTe_5$". In: *Nature Physics* 12.6 (2016), pp. 550–554.

[163] G. Manzoni et al. "Evidence for a Strong Topological Insulator Phase in $ZrTe_5$". In: *Phys. Rev. Lett.* 117 (23 Nov. 2016), p. 237601. DOI: 10.1103/PhysRevLett.117.237601. URL: https://link.aps.org/doi/10.1103/PhysRevLett.117.237601.

[164] Guolin Zheng et al. "Transport evidence for the three-dimensional Dirac semimetal phase in $ZrTe_5$". In: *Phys. Rev. B* 93 (11 Mar. 2016), p. 115414. DOI: 10.1103/PhysRevB.93.115414. URL: https://link.aps.org/doi/10.1103/PhysRevB.93.115414.

[165] H. Xiong et al. "Three-dimensional nature of the band structure of $ZrTe_5$ measured by high-momentum-resolution photoemission spectroscopy". In: *Phys. Rev. B* 95 (19 May 2017), p. 195119. DOI: 10.1103/PhysRevB.95.195119. URL: https://link.aps.org/doi/10.1103/PhysRevB.95.195119.

[166] Yan Zhang et al. "Electronic evidence of temperature-induced Lifshitz transition and topological nature in $ZrTe_5$". In: *Nature communications* 8.1 (2017), pp. 1–9.

[167] Polychronis Tsipas et al. "Massless dirac fermions in $ZrTe_2$ semimetal grown on InAs (111) by van der Waals epitaxy". In: *ACS nano* 12.2 (2018), pp. 1696–1703.

[168] L. Perfetti et al. "High-resolution angle-resolved photoemission investigation of the quasiparticle scattering processes in a model Fermi liquid: $1T - TiTe_2$". In: *Phys. Rev. B* 64 (11 Aug. 2001), p. 115102. DOI: 10.1103/PhysRevB.64.115102. URL: https://link.aps.org/doi/10.1103/PhysRevB.64.115102.

[169] G. Nicolay et al. "Importance of many-body effects to the spectral function of $1T$-$TiTe_2$". In: *Phys. Rev. B* 73 (4 Jan. 2006), p. 045116. DOI: 10.1103/PhysRevB.73.045116. URL: https://link.aps.org/doi/10.1103/PhysRevB.73.045116.

[170] Qingyun Zhang, Yingchun Cheng, and Udo Schwingenschlögl. "Series of topological phase transitions in $TiTe_2$ under strain". In: *Phys. Rev. B* 88 (15 Oct. 2013), p. 155317. DOI: 10.1103/PhysRevB.88.155317. URL: https://link.aps.org/doi/10.1103/PhysRevB.88.155317.

[171] Zhiyong Zhu, Yingchun Cheng, and Udo Schwingenschlögl. "Topological Phase Diagrams of Bulk and Monolayer $TiS_{2-x}Te_x$". In: *Phys. Rev. Lett.* 110 (7 Feb. 2013), p. 077202. DOI: 10.1103/PhysRevLett.110.077202. URL: https://link.aps.org/doi/10.1103/PhysRevLett.110.077202.

[172] RC Xiao et al. "Manipulating superconductivity of 1 T-$TiTe_2$ by high pressure". In: *Journal of Materials Chemistry C* 5.17 (2017), pp. 4167–4173.

[173] Peng Chen et al. "Emergence of charge density waves and a pseudogap in single-layer $TiTe_2$". In: *Nature communications* 8.1 (2017), pp. 1–6.

[174] V. Rajaji et al. "Structural, vibrational, and electrical properties of $1T-TiTe_2$ under hydrostatic pressure: Experiments and theory". In: *Phys. Rev. B* 97 (8 Feb. 2018), p. 085107. DOI: 10.1103/PhysRevB.97.085107. URL: https://link.aps.org/doi/10.1103/PhysRevB.97.085107.

[175] U. Dutta et al. "Pressure-induced superconductivity in semimetallic $1T - TiTe_2$ and its persistence upon decompression". In: *Phys. Rev. B* 97 (6 Feb. 2018), p. 060503. DOI: 10.1103/PhysRevB.97.060503. URL: https://link.aps.org/doi/10.1103/PhysRevB.97.060503.

[176] Xiao-Fang Tang et al. "Three-dimensional Fermi surface and electron-phonon coupling in semimetallic 1T- $TiTe_2$ studied by angle-resolved photoemission spectroscopy". In: *Phys. Rev. B* 99 (12 Mar. 2019), p. 125112. DOI: 10.1103/PhysRevB.99.125112. URL: https://link.aps.org/doi/10.1103/PhysRevB.99.125112.

[177] JG Smeggil and S Bartram. "The preparation and x ray characterization of $HfTe_2 - x$, x= 0.061". In: *Journal of Solid State Chemistry* 5.3 (1972), pp. 391–394. URL: https://www.sciencedirect.com/science/article/pii/0022459672900837.

[178] David Hodul and MJ Sienko. "Solid state studies of $HfSe_2 - xTe_x$ and $HfTe_2 - x$". In: *Physica B+ C* 99.1-4 (1980), pp. 215–218. URL: https://www.sciencedirect.com/science/article/pii/0378436380902351.

[179] P C Klipstein et al. "Electronic properties of HfTe2". In: *Journal of Physics C: Solid State Physics* 19.25 (Sept. 1986), pp. 4953–4963. DOI: 10.1088/0022-3719/19/25/012. URL: https://doi.org/10.1088%2F0022-3719%2F19%2F25%2F012.

[180] Y Aoki et al. "Hf-Ditelluride: Phase transition under pressure". In: *Synthetic Metals* 71.1-3 (1995), pp. 1883–1884. URL: https://www.sciencedirect.com/science/article/abs/pii/037967799403090S.

[181] Yasuyuki Aoki et al. "Thermopower of $HfTe_2$ and $ZrTe_2$". In: *Journal of the Physical Society of Japan* 65.8 (1996), pp. 2590–2593. URL: https://journals.jps.jp/doi/abs/10.1143/JPSJ.65.2590.

[182] Ali Hussain Reshak and S Auluck. "Ab initio calculations of the electronic and optical properties of 1T-HfX_2 compounds". In: *Physica B: Condensed Matter* 363.1-4 (2005), pp. 25–31. URL: https://www.sciencedirect.com/science/article/pii/S0921452605005843.

[183] Sebastian Mangelsen and Wolfgang Bensch. "$HfTe_2$: Enhancing Magnetoresistance Properties by Improvement of the Crystal Growth Method". In: *Inorganic Chemistry* (2019). URL: https://pubs.acs.org/doi/10.1021/acs.inorgchem.9b02734.

[184] S Aminalragia-Giamini et al. "Molecular beam epitaxy of thin $HfTe_2$ semimetal films". In: *2D Materials* 4.1 (Oct. 2016), p. 015001. DOI: 10.1088/2053-1583/4/1/015001. URL: https://doi.org/10.1088%2F2053-1583%2F4%2F1%2F015001.

[185] Cai Cheng et al. "Hidden spin polarization in the 1T-phase layered transition-metal dichalcogenides MX_2 (M= Zr, Hf; X= S, Se, Te)". In: *Science Bulletin* 63.2 (2018), pp. 85–91.

[186] Y. Nakata et al. "Dimensionality reduction and band quantization induced by potassium intercalation in $1T-HfTe_2$". In: *Phys. Rev. Materials* 3 (7 July 2019), p. 071001. DOI: 10.1103/PhysRevMaterials.3.071001. URL: https://link.aps.org/doi/10.1103/PhysRevMaterials.3.071001.

[187] Wei Yao et al. "Direct observation of spin-layer locking by local Rashba effect in monolayer semiconducting $PtSe_2$ film". In: *Nature communications* 8.1 (2017), pp. 1–6.

[188] Peter Blaha et al. "wien2k". In: *An augmented plane wave+ local orbitals program for calculating crystal properties* (2001). URL: https://www.bc.edu/content/dam/bc1/schools/mcas/physics/pdf/wien2k/Overview-WIEN2k2C_forces_etc_Blaha.pdf.

[189] K. Rossnagel, L. Kipp, and M. Skibowski. "Charge-density-wave phase transition in $1T - TiSe_2$: Excitonic insulator versus band-type Jahn-Teller mechanism". In: *Phys. Rev. B* 65 (23 May 2002), p. 235101. DOI: 10.1103/PhysRevB.65.235101. URL: https://link.aps.org/doi/10.1103/PhysRevB.65.235101.

[190] SB Dugdale. "Life on the edge: a beginner's guide to the Fermi surface". In: *Physica Scripta* 91.5 (2016), p. 053009.

[191] Amalia I Coldea. "Quantum oscillations probe the normal electronic states of novel superconductors". In: *Philosophical Transactions of the Royal Society A: Mathematical, Physical and Engineering Sciences* 368.1924 (2010), pp. 3503–3517.

[192] T. Mitsuhashi et al. "Influence of $k_\perp$ broadening on ARPES spectra of the (110) and (001) surfaces of $\mathbf{SrVO_3}$ films". In: *Phys. Rev. B* 94 (12 Sept. 2016), p. 125148. DOI: 10.1103/PhysRevB.94.125148. URL: https://link.aps.org/doi/10.1103/PhysRevB.94.125148.

[193] Ting Cao et al. "Valley-selective circular dichroism of monolayer molybdenum disulphide". In: *Nature communications* 3.1 (2012), pp. 1–5.

[194] JM Lu et al. "Evidence for two-dimensional Ising superconductivity in gated MoS_2". In: *Science* 350.6266 (2015), pp. 1353–1357.

[195] Yu Saito et al. "Superconductivity protected by spin–valley locking in ion-gated MoS_2". In: *Nature Physics* 12.2 (2016), pp. 144–149.

[196] Hongtao Yuan et al. "Evolution of the valley position in bulk transition-metal chalcogenides and their monolayer limit". In: *Nano letters* 16.8 (2016), pp. 4738–4745.

[197] Yi Zhang et al. "Electronic structure, surface doping, and optical response in epitaxial WSe_2 thin films". In: *Nano letters* 16.4 (2016), pp. 2485–2491.

[198] Yuki Nakata et al. "Anisotropic band splitting in monolayer $NbSe_2$: implications for superconductivity and charge density wave". In: *npj 2D Materials and Applications* 2.1 (2018), pp. 1–6.

[199] Per Joensen, RF Frindt, and S Roy Morrison. "Single-layer MoS_2". In: *Materials research bulletin* 21.4 (1986), pp. 457–461.

[200] Atsushi Koma. "Van der Waals epitaxy for highly lattice-mismatched systems". In: *Journal of crystal growth* 201 (1999), pp. 236–241.

[201] Peter W Sutter, Jan-Ingo Flege, and Eli A Sutter. "Epitaxial graphene on ruthenium". In: *Nature materials* 7.5 (2008), pp. 406–411.

[202] Daeho Kim et al. "Toward the growth of an aligned single-layer MoS_2 film". In: *Langmuir* 27.18 (2011), pp. 11650–11653.

[203] K Rossnagel. "Suppression and emergence of charge-density waves at the surfaces of layered 1T-$TiSe_2$ and 1T-TaS_2 by in situ Rb deposition". In: *New Journal of Physics* 12.12 (2010), p. 125018. URL: https://iopscience.iop.org/article/10.1088/1367-2630/12/12/125018.

[204] Jimin Kim et al. "Observation of tunable band gap and anisotropic Dirac semimetal state in black phosphorus". In: *Science* 349.6249 (2015), pp. 723–726. URL: https://science.sciencemag.org/content/349/6249/723.full.

[205] Seung Su Baik et al. "Emergence of two-dimensional massless dirac fermions, chiral pseudospins, and berry's phase in potassium doped few-layer black phosphorus". In: *Nano letters* 15.12 (2015), pp. 7788–7793. URL: https://pubs.acs.org/doi/10.1021/acs.nanolett.5b04106.

[206] Jimin Kim et al. "Two-Dimensional Dirac Fermions Protected by Space-Time Inversion Symmetry in Black Phosphorus". In: *Phys. Rev. Lett.* 119 (22 Nov. 2017), p. 226801. DOI: 10.1103/PhysRevLett.119.226801. URL: https://link.aps.org/doi/10.1103/PhysRevLett.119.226801.

[207] Sung Won Jung et al. "Black phosphorus as a bipolar pseudospin semiconductor". In: *Nature Materials* (2020), pp. 1–5. URL: https://www.nature.com/articles/s41563-019-0590-2.

[208] T Eknapakul et al. "Electronic structure of a quasi-freestanding MoS2 monolayer". In: *Nano letters* 14.3 (2014), pp. 1312–1316. URL: https://pubs.acs.org/doi/abs/10.1021/nl4042824.

[209] Soohyun Cho et al. "Electronic-dimensionality reduction of bulk MoS_2 by hydrogen treatment". In: *Physical Chemistry Chemical Physics* 20.35 (2018), pp. 23007–23012. URL: https://pubs.rsc.org/en/content/articlelanding/2018/cp/c8cp02365d#!divAbstract.

[210] T. Eknapakul et al. "Nearly-free-electron system of monolayer Na on the surface of single-crystal $HfSe_2$". In: *Phys. Rev. B* 94 (20 Nov. 2016), p. 201121. DOI: 10.1103/PhysRevB.94.201121. URL: https://link.aps.org/doi/10.1103/PhysRevB.94.201121.

[211] Nasser Alidoust et al. "Observation of monolayer valence band spin-orbit effect and induced quantum well states in MoX_2". In: *Nature Communications* 5 (2014), p. 4673. URL: https://www.nature.com/articles/ncomms5673.

[212] Ulrike A Schröder et al. "Core level shifts of intercalated graphene". In: *2D Materials* 4.1 (Nov. 2016), p. 015013. DOI: 10.1088/2053-1583/4/1/015013. URL: https://doi.org/10.1088%2F2053-1583%2F4%2F1%2F015013.

[213] N. Ehlen et al. "Direct observation of a surface resonance state and surface band inversion control in black phosphorus". In: *Phys. Rev. B* 97 (4 Jan. 2018), p. 045143. DOI: 10.1103/PhysRevB.97.045143. URL: https://link.aps.org/doi/10.1103/PhysRevB.97.045143.

[214] T Jaouen et al. "Unveiling the Semimetallic Nature of 1*T*-TiSe_2 by Doping its Charge Density Wave". In: *arXiv preprint arXiv:1911.06053* (2019). URL: https://arxiv.org/abs/1911.06053.

[215] CHP Wen et al. "Anomalous correlation effects and unique phase diagram of electron-doped FeSe revealed by photoemission spectroscopy". In: *Nature Communications* 7.1 (2016), pp. 1–7. URL: https://www.nature.com/articles/ncomms10840.

[216] Barun Ghosh et al. "Observation of bulk states and spin-polarized topological surface states in transition metal dichalcogenide Dirac semimetal candidate $NiTe_2$". In: *Phys. Rev. B* 100 (19 Nov. 2019), p. 195134. DOI: 10.1103/PhysRevB.100.195134. URL: https://link.aps.org/doi/10.1103/PhysRevB.100.195134.

[217] Saumya Mukherjee et al. "Fermi-crossing Type-II Dirac fermions and topological surface states in $NiTe_2$". In: *arXiv preprint arXiv:1912.08535* (2019). URL: https://arxiv.org/abs/1912.08535.

[218] Dongjing Lin et al. "Patterns and driving forces of dimensionality-dependent charge density waves in 2H-type transition metal dichalcogenides". In: *Nature communications* 11.1 (2020), pp. 1–9.

[219] Raffaello Bianco et al. "Quantum enhancement of charge density wave in NbS_2 in the two-dimensional limit". In: *Nano letters* 19.5 (2019), pp. 3098–3103.

[220] Ph Hofmann et al. "Electron–phonon coupling at surfaces and interfaces". In: *New Journal of Physics* 11.12 (2009), p. 125005.

[221] Jun Nagamatsu et al. "Superconductivity at 39 K in magnesium diboride". In: *nature* 410.6824 (2001), pp. 63–64.

[222] XX Xi. "Two-band superconductor magnesium diboride". In: *Reports on Progress in Physics* 71.11 (2008), p. 116501.

[223] F Bouquet et al. "Specific heat of $Mg^{11}B_2$: evidence for a second energy gap". In: *Physical review letters* 87.4 (2001), p. 047001.

[224] HD Yang et al. "Order parameter of MgB_2: a fully gapped superconductor". In: *Physical review letters* 87.16 (2001), p. 167003.

[225] P. Szabó et al. "Evidence for Two Superconducting Energy Gaps in MgB_2 by Point-Contact Spectroscopy". In: *Phys. Rev. Lett.* 87 (13 Sept. 2001), p. 137005. DOI: 10.1103/PhysRevLett.87.137005. URL: https://link.aps.org/doi/10.1103/PhysRevLett.87.137005.

[226] X. K. Chen et al. "Evidence for Two Superconducting Gaps in MgB_2". In: *Phys. Rev. Lett.* 87 (15 Sept. 2001), p. 157002. DOI: 10.1103/PhysRevLett.87.157002. URL: https://link.aps.org/doi/10.1103/PhysRevLett.87.157002.

[227] S. Tsuda et al. "Evidence for a Multiple Superconducting Gap in MgB_2 from High-Resolution Photoemission Spectroscopy". In: *Phys. Rev. Lett.* 87 (17 Oct. 2001), p. 177006. DOI: 10.1103/PhysRevLett.87.177006. URL: https://link.aps.org/doi/10.1103/PhysRevLett.87.177006.

[228] S Souma et al. "The origin of multiple superconducting gaps in MgB_2". In: *Nature* 423.6935 (2003), pp. 65–67.

[229] Ke Chen et al. "Momentum-dependent multiple gaps in magnesium diboride probed by electron tunnelling spectroscopy". In: *Nature communications* 3.1 (2012), pp. 1–5.

[230] Hyoung Joon Choi et al. "The origin of the anomalous superconducting properties of MgB_2". In: *Nature* 418.6899 (2002), pp. 758–760.

[231] Hyoung Joon Choi et al. "First-principles calculation of the superconducting transition in MgB_2 within the anisotropic Eliashberg formalism". In: *Physical Review B* 66.2 (2002), p. 020513.

[232] Hyoung Joon Choi, Marvin L Cohen, and Steven G Louie. "Anisotropic Eliashberg theory and the two-band model for the superconducting properties of MgB_2". In: *Physical Review B* 73.10 (2006), p. 104520.

[233] Asier Eiguren and Claudia Ambrosch-Draxl. "Wannier interpolation scheme for phonon-induced potentials: Application to bulk MgB_2, W, and the (1×1) H-covered W (110) surface". In: *Physical Review B* 78.4 (2008), p. 045124.

[234] Elena Roxana Margine and Feliciano Giustino. "Anisotropic migdal-eliashberg theory using wannier functions". In: *Physical Review B* 87.2 (2013), p. 024505.

[235] Bartholomew Mears Ludbrook. "Electron-phonon mediated superconductivity probed by ARPES: from MgB_2 to lithium-decorated graphene". PhD thesis. University of British Columbia, 2014.

[236] Arnab Majumdar et al. "Interplay of charge density wave and multiband superconductivity in layered quasi-two-dimensional materials: The case of 2H−NbS_2 and 2H−$NbSe_2$". In: *Phys. Rev. Materials* 4 (8 Aug. 2020), p. 084005. DOI: 10.1103/PhysRevMaterials.4.084005. URL: https://link.aps.org/doi/10.1103/PhysRevMaterials.4.084005.

[237] Raluca-Maria Stan et al. "Epitaxial single-layer NbS_2 on Au(111): Synthesis, structure, and electronic properties". In: *Phys. Rev. Materials* 3 (4 Apr. 2019), p. 044003. DOI: 10.1103/PhysRevMaterials.3.044003. URL: https://link.aps.org/doi/10.1103/PhysRevMaterials.3.044003.

[238] Haicheng Lin et al. "Growth of atomically thick transition metal sulfide film-son graphene/6H-SiC (0001) by molecular beam epitaxy". In: *Nano Research* 11.9 (2018), pp. 4722–4727.

[239] N Sirica et al. "The nature of ferromagnetism in the chiral helimagnet $Cr_{1/3}NbS_2$". In: *Communications Physics* 3.1 (2020), pp. 1–8.

[240] Corsin Battaglia et al. "Non-uniform doping across the Fermi surface of NbS_2 intercalates". In: *The European Physical Journal B* 57.4 (2007), pp. 385–390.

[241] Dawei Shen et al. "Joint density of states and charge density wave in 2H-structured transition metal dichalcogenides". In: *Journal of Physics and Chemistry of Solids* 69.12 (2008), pp. 2975–2977.

[242] J Brandt et al. "Band structure of the misfit compound (PbS) NbS_2 compared to $NbSe_2$: experiment and theory". In: *Journal of Electron Spectroscopy and Related Phenomena* 114 (2001), pp. 555–561.

[243] Erik GCP van Loon et al. "Competing Coulomb and electron–phonon interactions in NbS_2". In: *npj Quantum Materials* 3.1 (2018), pp. 1–8.

[244] Wei Bai et al. "Monolayer Behavior of NbS_2 in Natural van der Waals Heterostructures". In: *The Journal of Physical Chemistry Letters* 9.22 (2018), pp. 6421–6425.

[245] Andor Kormányos et al. "Tunable Berry curvature and valley and spin Hall effect in bilayer MoS_2". In: *Phys. Rev. B* 98 (3 July 2018), p. 035408. DOI: 10.1103/PhysRevB.98.035408. URL: https://link.aps.org/doi/10.1103/PhysRevB.98.035408.

[246] Drew W. Latzke et al. "Electronic structure, spin-orbit coupling, and interlayer interaction in bulk MoS_2 and WS_2". In: *Phys. Rev. B* 91 (23 June 2015), p. 235202. DOI: 10.1103/PhysRevB.91.235202. URL: https://link.aps.org/doi/10.1103/PhysRevB.91.235202.

[247] S. V. Borisenko et al. "Two Energy Gaps and Fermi-Surface "Arcs" in $NbSe_2$". In: *Phys. Rev. Lett.* 102 (16 Apr. 2009), p. 166402. DOI: 10.1103/PhysRevLett.102.166402. URL: https://link.aps.org/doi/10.1103/PhysRevLett.102.166402.

[248] Lewis Bawden et al. "Spin–valley locking in the normal state of a transition-metal dichalcogenide superconductor". In: *Nature communications* 7 (2016), p. 11711.

[249] Christoph Heil, Martin Schlipf, and Feliciano Giustino. "Quasiparticle *GW* band structures and Fermi surfaces of bulk and monolayer NbS_2". In: *Phys. Rev. B* 98 (7 Aug. 2018), p. 075120. DOI: 10.1103/PhysRevB.98.075120. URL: https://link.aps.org/doi/10.1103/PhysRevB.98.075120.

[250] A Meerschaut and C Deudon. "Crystal structure studies of the 3R-$Nb_1.09S2S_2$ and the 2H-$NbSe_2$ compounds: correlation between nonstoichiometry and stacking type (= polytypism)". In: *Materials research bulletin* 36.9 (2001), pp. 1721–1727.

[251] T. Machida et al. "Orbital-dependent quasiparticle scattering interference in $3R - NbS_2$". In: *Phys. Rev. B* 96 (7 Aug. 2017), p. 075206. DOI: 10.1103/PhysRevB.96.075206. URL: https://link.aps.org/doi/10.1103/PhysRevB.96.075206.

[252] Sung-Kwan Mo et al. "Spin-resolved photoemission study of epitaxially grown $MoSe_2$ and WSe_2 thin films". In: *Journal of physics: Condensed matter* 28.45 (2016), p. 454001.

[253] K. Rossnagel et al. "Fermi surface of $2H - NbSe_2$ and its implications on the charge-density-wave mechanism". In: *Phys. Rev. B* 64 (23 Nov. 2001), p. 235119. DOI: 10.1103/PhysRevB.64.235119. URL: https://link.aps.org/doi/10.1103/PhysRevB.64.235119.

[254] Felix Flicker and Jasper Van Wezel. "Charge order from orbital-dependent coupling evidenced by $NbSe_2$". In: *Nature communications* 6.1 (2015), pp. 1–6.

[255] Felix Flicker and Jasper van Wezel. "Charge order in $\mathbf{NbSe_2}$". In: *Phys. Rev. B* 94 (23 Dec. 2016), p. 235135. DOI: 10.1103/PhysRevB.94.235135. URL: https://link.aps.org/doi/10.1103/PhysRevB.94.235135.

[256] Yoshimasa Nishio et al. "Role of Electron-Lattice Interaction in Layered Transition Metal Dichalcogenide 2H-NbS_2. I. Phonon Anomaly and Superconductivity". In: *Journal of the Physical Society of Japan* 63.1 (1994), pp. 156–167.

[257] Aravind Devarakonda et al. "Clean 2D superconductivity in a bulk van der Waals superlattice". In: *Science* 370.6513 (2020), pp. 231–236.